Travail de fin d'études et stage[BR]- Travail de fin d'études : Preliminary Design of a Transverse Composite Leaf Spring for Electric Vehicles[BR]- Stage d'insertion professionnelle

Auteur : Van Hulle, Samuel
Promoteur(s) : Duysinx, Pierre
Faculté : Faculté des Sciences appliquées
Diplôme : Master en ingénieur civil mécanicien, à finalité spécialisée en technologies durables en automobile
Année académique : 2022-2023
URI/URL : http://hdl.handle.net/2268.2/18334

Preliminary Design of a Transverse Composite Leaf Spring for Electric Vehicles

Master thesis conducted to obtain the Master's degree of Science in Mechanical Engineering, specialised in Sustainable Automotive Technologies

VAN HULLE Samuel - 20181098

Supervisor:	DUYSINX Pierre
Second supervisor:	TROMME Emmanuel
Date final version:	21st August 2023

University of Liège
Faculty of Applied Sciences
Mechanical Engineering
Academic Year 2022-2023

Abstract

With growing demand in battery electric vehicles, car manufacturers are facing new challenges in mass reduction and space optimisation of the suspension designs. A possible solution to this problem is to integrate several suspension members into a single, more compact transverse composite leaf spring. The aim of this Master's thesis is to develop a reliable and general analytical method allowing the computation of a preliminary design for transverse composite leaf springs.

The analytical design methodology starts with the definition of the starting independent suspension in which the leaf will be integrated and the choice of laminate material for the manufacturing of the leaf spring. The possible designs of the leaf based on the integrated suspension members are then established. The leaf is modeled using classical beam theory and classical laminate plate theory together. A method to compute the suspension forces graphically is then derived and paired with a two-dimensional kinematic model of the suspension to fully determine the configuration of the suspension along the wheel stroke.

This analytical method is then applied to the 2004 Audi A6, which has short long arm suspensions on its rear axle. This results in two different geometries of the leaf springs: one leaf of 11mm thickness, 100mm width and length of 1340mm, the second one with the same geometry but a thickness of 17.3mm. This last leaf design gives an equivalent roll stiffness of 936Nm/deg on the rear axle, as it integrates the anti-roll bar properties. Kinematic performance curves of the transverse leaf spring suspension are assessed and give similar/close results compared to the original coil spring suspension design. For each leaf design, stresses are computed and the Tsaï-Wu failure criteria is verified. For all designs, the criteria is met.

Finite element analysis is performed on the obtained leaf designs. Using NASTRAN SOL 402, assumptions on the large deformation of the leaf springs are verified. This leads to the conclusion that the model used for the first leaf design has to be improved when the leaf experiences very large deformations. On the other hand, the model for the second leaf design can be simplified by considering that the large deformation of the leaf is given by an equivalent rotating rigid arms. Modal analysis of the leaves using NASTRAN SOL 103 shows that the natural frequencies of the leaves are all greater than the frequency due to the road surface irregularities (12Hz).

Acknowledgements

I would like to thank my supervisor Professor Pierre Duysinx for his trust and for giving me the opportunity to work on this very interesting subject. Thank you also to my second supervisor Professor Emmamnuel Tromme for his precious time, advices and for sharing his wide knowledge over suspensions with me. Special thanks to Professor Michaël Bruyneel for sharing his knowledge over composite laminates properties, manufacturing processes and numerical modeling.

On a more general note, I would like to thank the jury members and anyone who dedicated a bit of their precious time to read and evaluate my work.

My last thanks are for my parents. Thanks to my mother who helped by proofreading this thesis and for her support throughout my studies. Thanks to my father, to whom I would like to dedicate my work as he always was my biggest motivation throughout my engineering studies.

Contents

List of Figures

List of Tables

Acronyms

ARB Anti-Roll Bar

BEV Battery Electric Vehicle

CFRP Carbon Fiber Reinforced Polymer

CLPT Classical Laminated Plate Theory

CM Center of Mass

CPC Contact Patch Center

DOF Degree Of Freedom

FE Finite Element

FRP Fiber Reinforced Plastic

GFRP Glass Fiber Reinforced Polymer

HP-RTM High Pressure Resin Transfer Molding

HVS High Voltage Storage

MBD Multi-Body Dynamics

RTM Resin Transfer Molding

SLA Short Long Arm

SMC Short Moulding Compound

Introduction

As an introduction, the general framework of the thesis is described. The more general context underlying the motivation is first presented and followed by a short definition of both objectives and structure of the study. This introduction is completed with an overview of the history and current technologies around leaf springs.

Context

Suspensions in cars have always historically provided great room for improvement from increasing functionalities for upper class vehicles to cost-optimized designs for more compact cars. With the growing demand in electric vehicles, new challenges appear during the design phase of the suspensions.

Energy consumption is becoming a key factor when designing a car. Therefore, more focus is put on lightweight design which, for suspensions members, is mainly characterised through the reduction of the unsprung mass. The reduction of the unsprung mass allows a reduction of the mass of the vehicle while improving overall performances of the suspension in handling and steering [1]. Most of the mass saving operations on suspension members consist in shape and material optimisation. The latter implies the use of more and more complex materials, such as composites laminates.

A new point of interest in suspension design is the integration of the battery for battery electric vehicles (BEVs). Currently, the most expensive part of a BEV is its high voltage storage (HVS) [2]. To reduce the cost of such batteries, a simple boxy geometry is required. Due to vehicle components, such as suspension arms and anti-roll bars, available space is restricted and simple design of the batteries cannot be achieved without impacting the electric range of the vehicle.

A solution to meet both requirements in mass reduction and in space optimisation is to design some suspension members based on functional integration of other members. In this context, car manufacturers such as Volvo or Chevrolet have developed independent axles based on a transverse leaf spring, which allows the integration of the coil spring, anti-roll bar and lower suspension arms into a single composite element. Structural integration in a transverse leaf spring allows to design more compact suspensions while taking advantage of the properties of composites [3] such as their strength-to-weight ratio, fatigue resistance, internal damping and fine tuning of the mechanical properties using laminates.

Objectives

The main objective of this thesis is to establish an analytical method allowing the computation of a preliminary design for a transverse composite leaf spring with specific structural integration requirements integrated in a pre-existing independent suspension on the rear axle. The method should remain as general as possible, so that it can be easily adapted to other independent suspension types and geometries. It is also required that the method predicts the behavior of the suspension after the integration of the leaf spring and assesses associated properties of the leaf following the integration of one or more suspension elements.

Structure of the study

This thesis is structured into five chapters:

- Chapter 1 is dedicated to the definition of the independent suspension model that is used as a basis for the development of the analytical design method. First, the type of suspension is chosen to best meet the requirement of generality of the method. A case study suspension is then selected accordingly. In a second time, the suspension and car characteristics are gathered and an equivalent multi-body finite element model of the suspension is created. Lastly, the multi-body model of the car is used to compute the motion and the evolution of the suspension forces, establishing a benchmark for preliminary designs that are computed afterwards.

- Chapter 2 focuses on the material study of the composite leaf spring. The laminate material for the leaf is first chosen using material selection amongst common materials used in the manufacturing of composite leaf springs. Material properties of the chosen material are then defined. Finally, adequate manufacturing processes for composite leaf springs are described.

- Chapter 3 is aimed at the establishment of the analytical method for the preliminary designs of the transverse leaf springs. A first section is dedicated to the definition of the different structural integration cases that are possible for the leaf spring, which are named as integration degrees. A second section is dedicated to the establishment of a leaf spring model based on *Classical Laminate Plate Theory* (CLPT) and on beam theory which are particularised according to the different integration degrees. The last section is dedicated to the suspension modeling, which is separated in two parts. The first part covers the computation of suspension forces whilst the second part covers the creation of an equivalent two-dimensional kinematic model that describes the motion of the suspension members along the vertical displacement of the wheel.

- Chapter 4 is dedicated to the computation of a preliminary leaf spring design based on the case study suspension. For each integration degree, the geometry of the leaf is first computed and assumptions regarding beam theory are verified. Modal analysis is then performed if an analytical solution exists for the corresponding beam model. As a second step, kinematic analysis of the suspension is carried out and compared with results from the suspension case study. Dynamic loading is then assessed based on a set of standard values. Afterwards, a comparison of the results between each integration degree is made. This chapter ends with the enumeration of several possible improvements on the different leaf designs based on the observation made with the analytical results.

- Chapter 5 is first aimed at the validation of the analytical results and assumptions. To do so, finite element models of the preliminary leaf designs are created. With these models, static analysis is performed on the leaf with different loads to assess validity of previously made assumptions. A rapid modal analysis is also performed on the leafs to assess whether or not it is suited to be fitted into an actual suspension.

Overview of leaf spring technology

Leaf springs are usually mounted longitudinally on heavy loaded vehicles such as vans and pick-ups. They are particularly suited for the rear suspension of those vehicles as they are compliant in the vertical direction and stiff in lateral and longitudinal directions [4]. The most familiar form of longitudinal leaf spring mountings is called the Hotchkiss arrangement. It is composed of a pair of semi-elliptic leaf springs which is attached to the rigid axle through U-clips. Connection to the body is made of a bushing on the one end and a shackle on the other end, allowing for the deformation of the leaf (Fig. 1).

In terms of materials, two families are commonly observed: steel and composite leafs. Steel leaf springs are most of the time composed of a pile of staged leafs with the same or different thickness called multiple-leaf springs. Those layers are required for the spring to obtain the required compliance and strength for the suspension. They are really cheap and easy to produce but this particular geometry leads to inter-leaf friction. This friction between leafs leads to a non-linear behavior of the spring deflection [5], which impacts the natural frequencies of the spring and therefore the driving comfort [6].

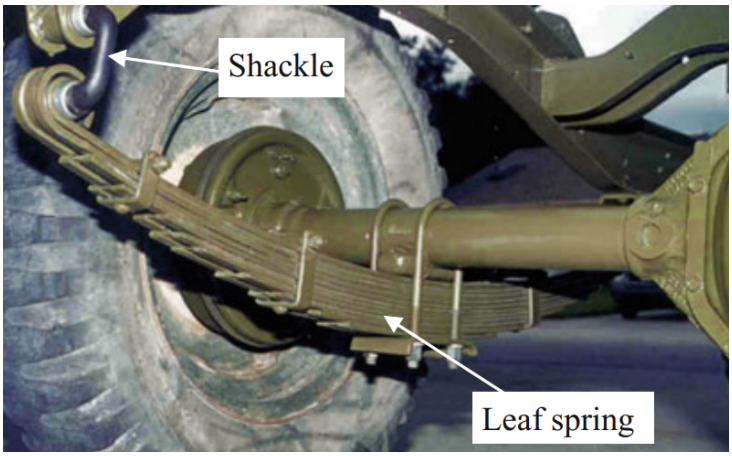

Figure 1: General Hotchkiss suspension system [4].

With the use of composite materials, this problem can be avoided since a mono-leaf spring design (Fig. 2) can be achieved due to their superior strain energy storage per weight (up to 5 times compared to steel [7]) and lamination, leading to a more compact and lighter leaf spring. Composites are also rather well suited for leaf springs as they provide superior fatigue strength, corrosion resistance and higher natural frequencies, leading to a smoother ride. The most commonly used composite materials are Carbon Fiber Reinforced Plastics (CFRP) and Glass Fiber Reinforced plastics (GFRP). CFRP is considered as a high end material, as the material and manufacturing costs are high but provide the lowest mass. GFRP is a cheaper alternative, as the material density is higher and the material properties are lower, increasing the mass [8].

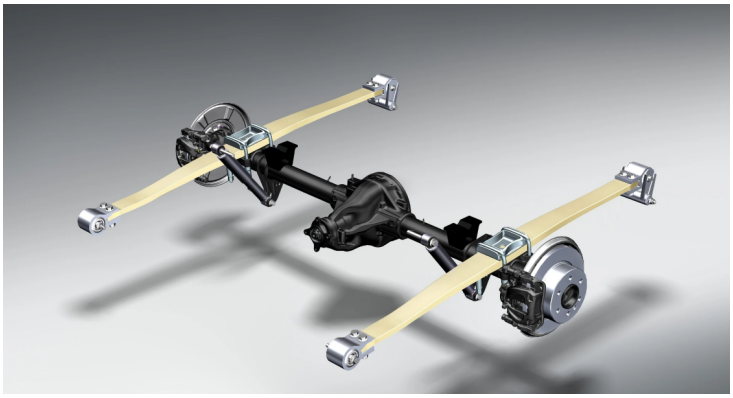

Figure 2: Rear axle of the Mercedes Sprinter with composite single-leaf springs [9].

Even though transverse leaf springs are not common for current suspensions, their use is not limited to recent times. In fact, the first mass produced car in history, the Ford T, was equipped with a front multi-leaf steel spring, as pictured in Fig. 3. This axle, often called the 'Suicide Axle', was particularly known for its poor handling due to their horizontal shackles that allowed lateral rocking. The design of this suspension was however motivated by the state of the roads at that time. Roads were mostly dirt

tracks, which made it difficult for cars to maintain the four wheels in contact with the ground. This lateral wheel travel allowed to keep contact with the ground [10]. This is why the Ford Motor Company kept using this front axle from 1908 to 1948, as after this period, tarmac roads became more common. Improvements in production machinery also allowed to produce better quality coil springs. For the record, the transverse leaf spring suspension is even older than the Ford T, as this suspension type can be found on coaches dated about 1650 [11].

Figure 3: Front suspension of the Ford T[12].

Even though coil springs became the norm for independent suspensions, some car manufacturers still tried to use transverse steel leaf springs. A well-known example is the Chevrolet Corvette, which started using transverse leaf springs with the Corvette C2 (1963). The C2 implemented a steel leaf spring in a rear independent suspension (Fig. 4) that allowed to have an anti-roll effect due to the leaf and its pivot mountings, which was designed by Zora Arkus-Duntov based on the CERV I (Chevrolet Experimental Racing Vehicle) from 1959 [13]. Other car manufacturers such as Fiat with the 128 and Triumph with the Spitfire used transverse steel leaf springs for their rear independent suspension.

Figure 4: Rear suspension of the Chevrolet Corvette C2 [14].

The most significant change in transverse leaf suspensions came with the Chevrolet Corvette C3 (1967). Initially, the C3 was equipped with the same rear suspension than the C2 but, in 1980, Chevrolet replaced the multi-leaf steel spring with a single mono-leaf FRP (Fiber Reinforced Plastic) spring. This allowed further weight saving on the rear axle, as the FRP allowed to save 19kg compared to the steel multi-leaf spring. Moreover, the mass of the FRP leaf only represents 33% of the mass for the equivalent coil spring suspension (also, the anti-roll bar could be either removed or a lighter one could be placed) [15]. Since they are the first manufacturer to utilise FRF mono-leaf springs, this type of independent suspension is often referred as the 'Corvette leaf spring'. Since then, almost all transverse leafs are made of composite materials.

Nowadays, with manufacturers needing to further reduce the mass of their vehicles (to limit the consumption) and also searching for compact suspensions (to allow space for the battery in electric vehicles), some car manufacturers are developing suspensions based on a transverse composite leaf spring. This appears to be a good solution, as the leaf allows to save weight with respect to coil spring designs and also further reduce the mass by functional integration of several other suspension members on the leaf. Apart from the independent suspension type on which the leaf is integrated (*e.g.* double wishbone, McPherson, ...), 4 different types of transverse leaf spring suspensions can be defined based on their degree of functional integration.

The first type of transverse leaf suspensions is when the leaf is used only to replace coil springs. A known example is the second generation of the Volvo XC90 (2015-) which uses an integral link rear axle with a GFRP transverse leaf spring (Fig. 5). In this case, the leaf spring allows a mass reduction of approximately 4.5kg, improvement of the NVH (Noise, Vibration and Harshness) and also adds some space to the trunk compared to the initial design with coil springs [16]. The leaf extremities are connected to the lower arm with vertical sliders and rubber bushings to further reduce vibrations. Connection to the body is made with 2 clamps at the top of the leaf and two others at the bottom of the leaf, with top and bottom clamps slightly unaligned. Following a patent from Hyundai [17], the asymmetric link improves driving comfort. The leaf spring is made of GFRP plies with unidirectional lay-up along the longitudinal direction of the leaf (transverse direction for the suspension) as the leaf only experiences vertical loads.

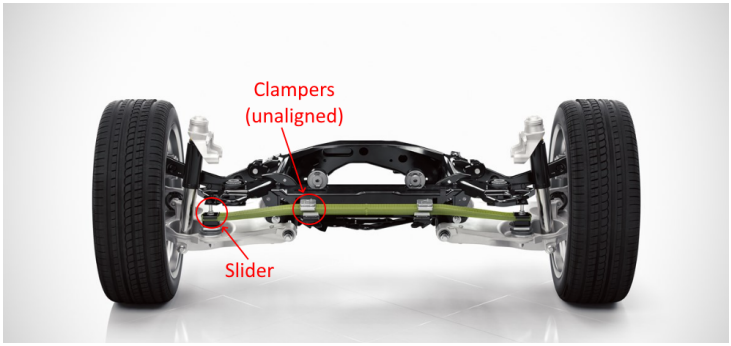

Figure 5: Rear suspension of the Volvo XC90 [18].

A second type of suspension is when the leaf is used to replace coil springs and also to have anti-roll properties, in order to replace totally the anti-roll bar or use a less stiff one. This allows to save some more weight and space. As explained earlier, a known example for this type of suspension is the Chevrolet Corvette. Starting from the C5, both front and rear suspensions of the Corvette consist in an independent suspension with unequal-length double wishbones and a transverse GFRP mono-leaf spring attached to the lower arm, pictured in Fig. 6. The leaf is attached to the car body through two widely spaced pivot mounts which give the leaf its anti-roll property. This property is explained by Michael Lamm [13]: "*The leaf actually would forms a S shape when the car rolls if the material was soft enough, the fact that it does not actually serves as counteracting this effect, hence minimizing roll*". Lamm also adds that the anti-roll effect can be tuned with the position of the pivot mounts and also by changing the thickness and width of the center part of the leaf. This allows the Corvette to have a lower ride height, reduce the stiffness of their anti-roll bars and save weight compared to the same suspension with coil springs. For some versions of the Corvette C7, the rear anti-roll bar could even be entirely removed.

(a) Rear suspension **(b)** Front suspension

Figure 6: Front and rear suspensions of the Chevrolet Corvette C5[19].

A third type of suspension is when the leaf is used to replace both coil springs and

control arms. This type of suspension is not common (even in patents), as one of the only example is a prototype from BMW presented at the 11th International Munich Chassis Symposium in 2020 [20]. This prototype presents a particular design, as it is technically not a transverse leaf design. For space reason, the leaf is separated into two parts (Fig. 7). The leaf is clamped to the body and is designed to only be compliant in the vertical direction, as the leaf must ensure the functions of the control arm. This suspension designed for the BMW i3 allows to save weight on both axles and also save space for a larger one-box design for the HVS instead of the conventional two-box design, as the single-leaf design is more compact than the series 5-link suspension (Fig. 8). However, as told by Dr. Emmanuel Tromme, this design was not conclusive in further testings as durability problems appeared. Therefore, they had to go back to the use a whole transverse leaf instead of their separate leaf design.

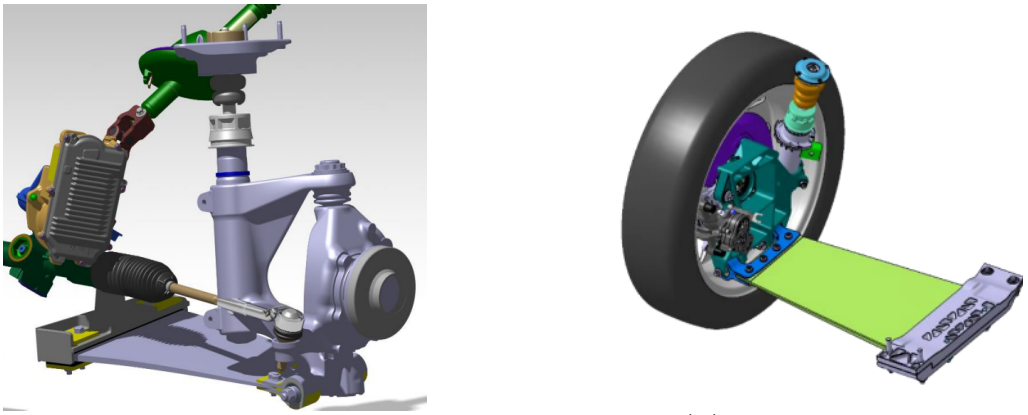

(a) Front suspension

(b) Rear suspension

Figure 7: Front and rear suspension prototypes for the BMW i3 [2].

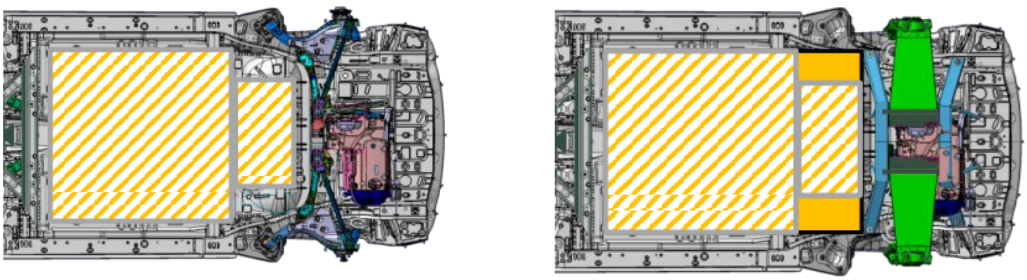

(a) Series rear axle

(b) Prototype rear axle

Figure 8: Available space for high voltage storage in an electrified compact car [2].

The last suspension type is when the leaf integrates the coil springs, anti-roll bar and control arms. This type of suspension is not really present on the market but can be seen in many patents and prototypes. One example is the GFRP transversal leaf spring for BEVs (Battery Electric Vehicles) from the automotive supplier Mubea (Fig. 9). This

suspension, presented at the 2021 International Motor Show in Munich, integrates anti-roll properties by using two pivot mounts at the center of the leaf. Since the leaf integrates the control arm, it must be stiff to lateral and longitudinal loads and compliant to the vertical load. To allow this vertical compliance, the leaf is made of unidirectional GFRP plies in the longitudinal direction. According to Mubea, this design is aimed at replacing multi-link axles allowing a weight reduction of approximately 20kg and freeing up some space for the batteries.

Figure 9: Mubea's GFRP transversal blade spring for BEV-axles [21].

Chapter 1

Initial suspension model

A suspension model is required to compute preliminary designs of the transverse leaf springs and to establish a benchmark when assessing their performance. This chapter first motivates the choice of suspension type that will be used in the development of the analytical design method. The suspension case study is then defined and a thorough kinematic analysis is performed to establish a benchmark for future computations.

1.1 Choice of the initial suspension design

The choice of the suspension is motivated with the objective of deriving a straightforward and reliable analytical model for the integration of the transverse leaf spring. With further aim of having a more general solution that can be adapted to other types of independent suspensions, the double wishbone suspension has been retained. This suspension type is commonly studied analytically in 2D using a front and side view plane (Fig. 1.1), which makes is simple to understand and compute forces acting of the suspension.

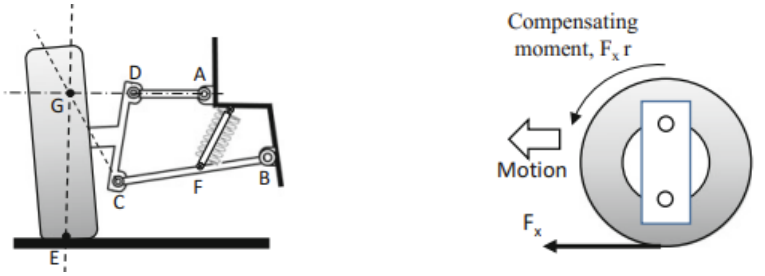

(a) Side view plane **(b)** Front view plane

Figure 1.1: 2D planes for the computation of forces in double wishbone suspensions [4].

Furthermore, the solution for the double wishbone suspension is usually applied to approximate multi-link suspensions and the solution for the MacPherson suspension can be retrieved by considering an infinitely long upper arm, as advised by David C. Barton and John D. Fieldhouse [4]. To further simplify the analytical solution, the suspension

is considered on the rear axle. This avoids having to take into account any turning mechanism in the computations.

The initial double wishbone suspension design is the one present on the pre 2005 Audi A6 (Fig. 1.2) rear axle, which is more specifically a Short Long Arm (SLA) suspension design. This specific suspension has been previously studied at the university of Liège in Professor Olivier Brüls Ph.D. dissertation on *Integrated Simulation and Reduced-Order Modeling of Controlled Flexible Multibody Systems* [22] [23].

Figure 1.2: Audi A6 (2004) [24].

In this context, a multi-body model based on the Finite Elements Method (FEM) was created on SAMCEF-MECANO based on real measurements performed on the car. Current study is based on this multi-body model, which was reconstructed through a data file provided by Dr. Emmanuel Tromme.

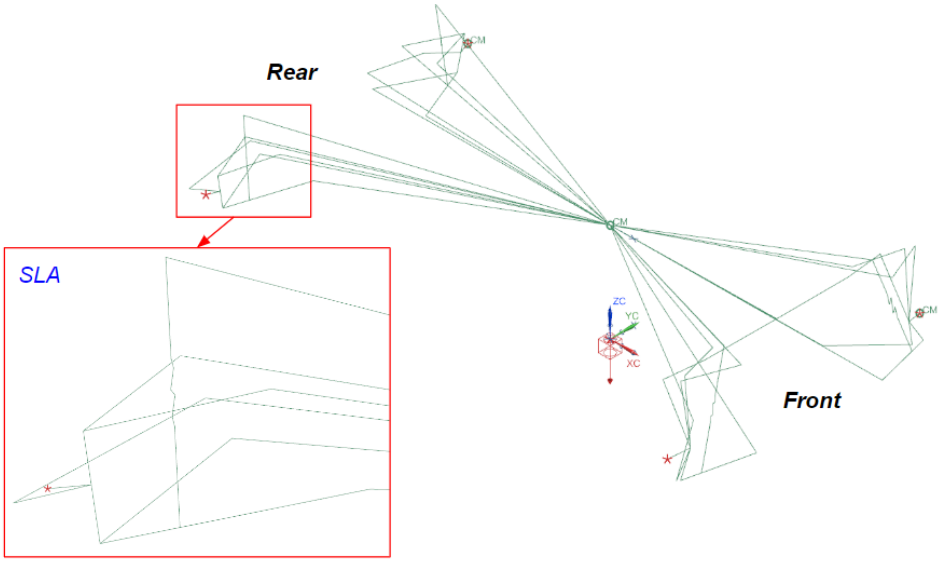

Figure 1.3: View of the provided multi-body model in Siemens NX22.

This model, which is not working in the current state of Siemens NX, is the starting point for the creation of a smaller 3D model representing only the rear axle of the car.

1.2 Suspension characteristics

Using the multi-body model of the A6 (Fig. 1.3), the position of the center of mass (Fig. 1.4) and a 3D schematic of the suspension geometry (Fig. 1.5) are defined. Numerical values associated to both Fig. 1.4 and Fig. 1.5 are gathered in Table 1.2. Other useful information for the suspension modeling can be found in Table 1.1. Please note that the vehicle axis are defined based on the ISO 8855:2011 [25].

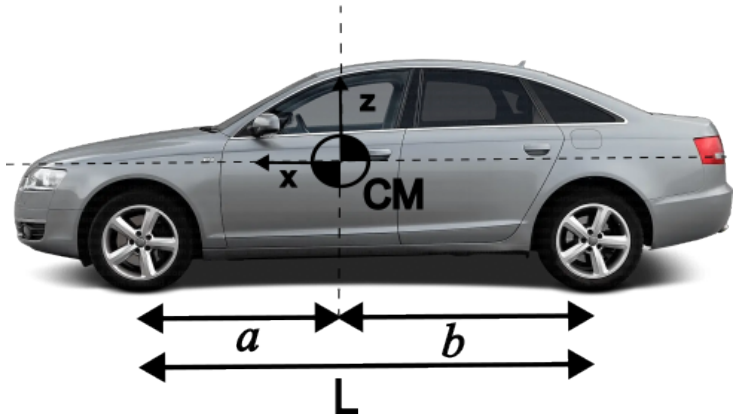

Figure 1.4: Position of the center of mass with respect to the side view plane of the car.

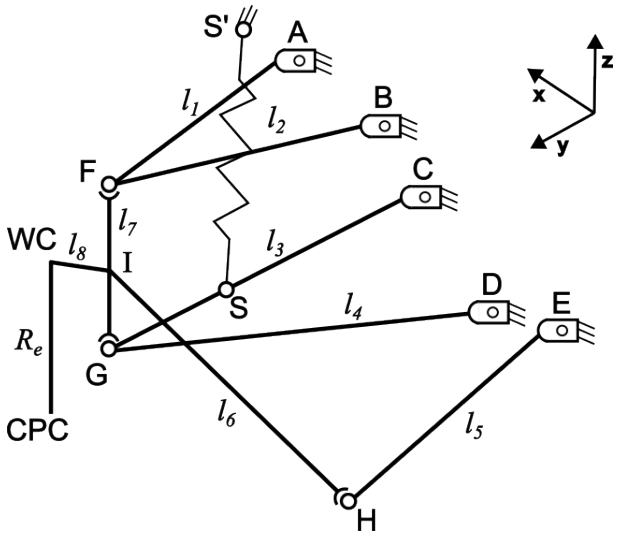

Figure 1.5: Simplified 3D multi-body model schematic of the rear left SLA suspension.

Parameter	Symbol	Value
Mass of the car	M	1146 kg
Mass of the wheel	M_W	15 kg
Linear stiffness of the spring	k	48 N/mm
Damping coefficient of the damper	c	2 N· s/mm

Table 1.1: General characteristics of the car and its suspension.

Parameter	Symbol(s)	Value [mm]
Position center of mass CM	(x_{CM}, y_{CM}, z_{CM})	(0, 0, 585)
Wheelbase	L	2714
Front distance to CM	a	1090
Rear distance to CM	b	1624
Length short arms	l_1, l_2	287
Length long arm 1	l_3	405
Length long arm 2	l_4	389
Length tie rod 1	l_5	356
Length tie rod 2	l_6	227
Length knuckle	l_7	192
Length wheel link	l_8	67
Effective rolling radius	R_e	318
Position hinge A	(x_A, y_A, z_A)	(-1495, 466, 434)
Position hinge B	(x_B, y_B, z_B)	(-1702, 466, 421)
Position hinge C	(x_C, y_C, z_C)	(-1429, 334, 265)
Position hinge D	(x_D, y_D, z_D)	(-1746, 334, 245)
Position hinge E	(x_E, y_E, z_E)	(-1789, 348, 297)
Position fixed end of spring S'	$(x_{S'}, y_{S'}, z_{S'})$	(-1608, 571, 631)
Initial position spherical joint F	(x_F, y_F, z_F)	(-1597, 733, 405)
Initial position spherical joint G	(x_G, y_G, z_G)	(-1605, 695, 217)
Initial position spherical joint H	(x_H, y_H, z_H)	(-1805, 695, 217)
Initial position point I	(x_H, y_H, z_H)	(-1601, 715, 315)
Initial position wheel center WC	(x_{WC}, y_{WC}, z_{WC})	(-1624, 778, 318)
Initial position CPC	$(x_{CPC}, y_{CPC}, z_{CPC})$	(-1624, 798, 0)
Initial position free end of spring S	(x_S, y_S, z_S)	(-1553, 589, 231)

Table 1.2: Geometry for the car and the suspension schematics.

It is worth to note that for the initial multi-body model, the car is considered in standard conditions. The only force acting on the car is its own weight with the car on a flat surface, meaning that the spring is already compressed. This position is considered

throughout the study as the reference position of the wheel (0mm stroke). In this configuration of the suspension, the initial value of the camber angle is $\gamma = -2.5°$ while the initial value for the toe angle is not known since the wheel is not represented in the initial model. The initial toe angle value is therefore considered 0°.

1.3 Kinematic analysis

Based on the geometry and parameters of the suspension, a NASTRAN-MECANO multi-body model is created to establish an initial benchmark for the design. The multi-body model is composed of the rear-left SLA suspension fixed to a fictional car body by the means of rigid links connected to the center of mass which is set fixed. Also, since NASTRAN does not allow the pre-compression of springs, a negative vertical force F_{init} corresponding to the reaction force due to the mass of the vehicle is added at the contact patch center (CPC). Using the position of the center of mass (Fig. 1.4) and performing the equilibrium, the reaction force on the rear axle writes

$$R_{rear} = Mg\frac{a}{L} = 1446 \cdot 9.81\frac{1090}{2714} = 5718\text{N}, \tag{1.1}$$

with g the gravitational constant. Force acting in one of the rear wheel contact patch is therefore $F_{init} = 5718/2 = 2859$N. The complete multi-body model is pictured in Fig. 1.6.

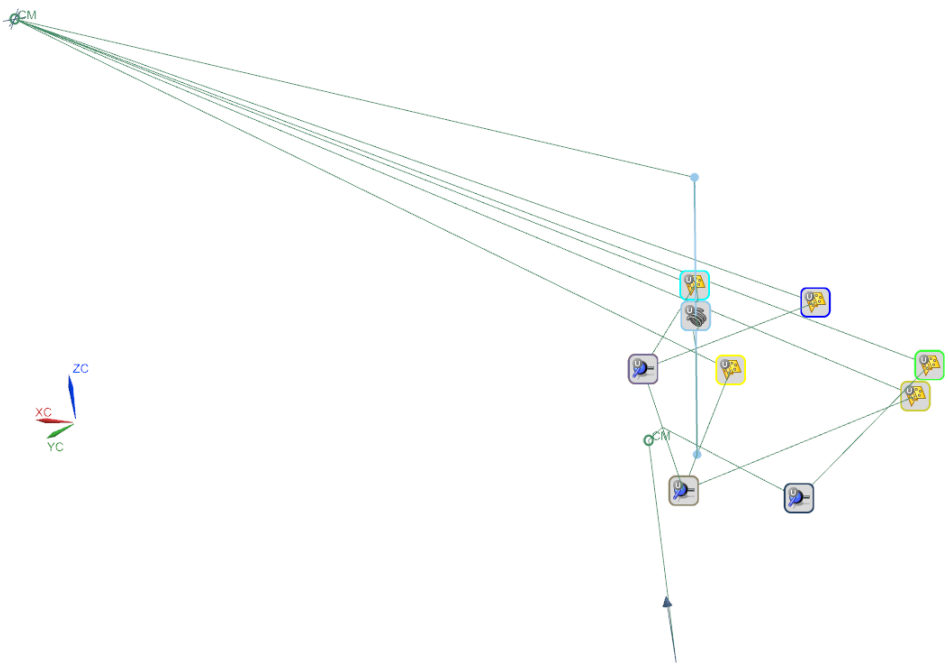

Figure 1.6: MECANO model of the initial suspension design.

To compute vertical force in the wheel contact patch and kinematic performance curves of the suspension, vertical displacement of the wheel is enforced through a constraint on

the contact patch center. Vertical displacement of the wheel is separated into positive displacement (jounce) and negative displacement (rebound) starting from the standard position of the suspension for which the vertical displacement of the wheel is 0mm. Maximum rebound position is defined as the vertical position of the wheel as the car lifts off the ground completely. In this configuration, only the mass of the wheel (m = 15kg) acts on the suspension, resulting in a -103mm vertical displacement. Maximum jounce position is usually limited by bump stops, which are nor defined nor available for this car. According to Genta [11], good practice when designing suspension for a passenger car is to consider a 70mm wheel displacement. Using this value for the undefined jounce, the total vertical stroke of the wheel is [-103; 70]mm. The simulation is performed using the NASTRAN SOL402 multi-step nonlinear kinematics solver. The case is solved as a nonlinear dynamics problem by using a generalized-α time integration scheme with spectral radius ρ_∞ = 0.8, leaving moderate numerical damping into the solution [26]. Jounce and rebound phases are separately performed in a 100s time in order to have a solution that is as close as possible to a static loading of the suspension. The time step is 0.1s which leads to sufficient precision of the solution and convergence of the solution. Using the solution of the simulation, the static loading in the contact patch along the displacement of the wheel (Fig. 1.7) is obtained and the kinematic performance curves (Fig. 1.8) are derived.

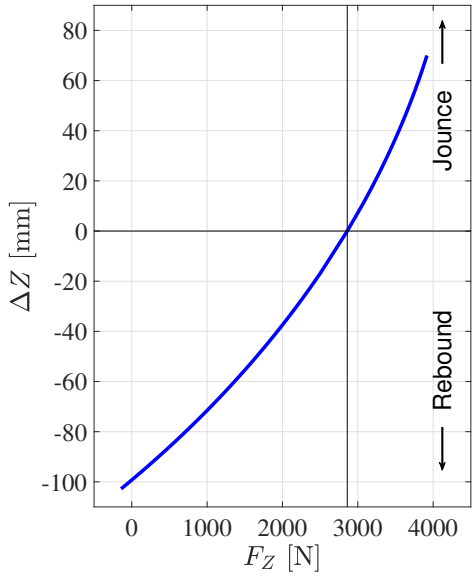

Figure 1.7: Vertical static loading in the contact patch center during jounce and rebound. Computed using the MECANO model.

As it can be seen in Fig. 1.7, the vertical force associated with the maximum jounce position yields F_Z = 3918N while the position corresponding to the unloaded (F_Z = 0N) position yields $\Delta Z = -99$mm.

The evolution of the vertical force in the contact is a convex function. This means that with an increasing force, the vertical displacement of the wheel increases more rapidly.

This may seem wrong at first sight but this behavior can simply be explained by two factors. First, when the wheel moves upwards, the free end of the spring attached to the lower arm experiences a lateral displacement along the y-axis. As the other end of the spring is fixed to the car body, the angle formed by the spring and the z-axis increases hence, the axial force induced by the spring is reduced. The other reason is that the spring is modeled as a linear element. In a real behavior, the spring would see its stiffness increase past a certain compression rate, which would lead to an increase in the axial force. Also, in practice, the positive vertical motion of the wheel is limited by a bump stop, which is a rubber element preventing contact between the suspension members and the body of the car.

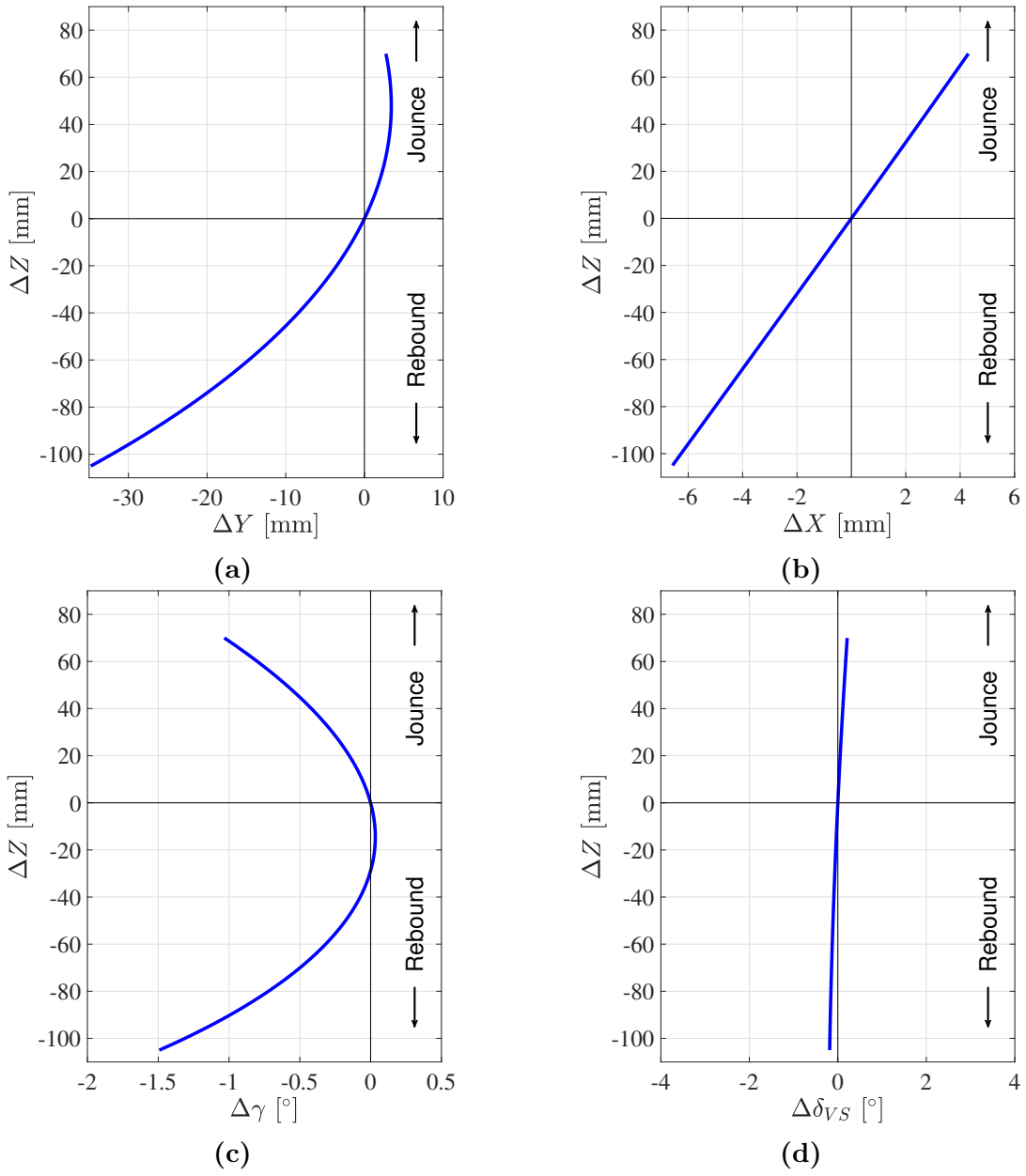

Figure 1.8: Half track (a), wheelbase (b), camber angle (c) and toe angle (d) variation during jounce and rebound. Computed using the MECANO model.

Half-track (Fig. 1.8a), camber angle (Fig. 1.8c) and toe angle (Fig. 1.8d) variation all have the expected behavior compared to other SLA suspension [27]. SLA suspensions are known for their negative camber gain compared to other variants of the double wishbone suspension (*e.g.* equal length arms). Also, a negative camber gain of $-1.5°$ is of the same order of magnitude as most passenger cars. For the wheelbase variation (Fig. 1.8b), the increasing wheelbase in jounce and decreasing wheelbase in rebound can be discussed. For double wishbone suspensions, upper and lower wishbones are both theoretically parallel to the x-axis, which means that there should not be any wheelbase change due to the vertical motion of the wheel. However, in the case of the Audi A6, the SLA suspension on the rear axle are actually by an angle of approximately $-3.6°$ in the xz-plane, which induces the wheelbase variation. This can be further verified by computing the minimum and maximum values of the camber gain:

$$\Delta X(\Delta Z = 70) = 4.3 \approx 70 \sin(3.6°) \tag{1.2}$$

$$\Delta X(\Delta Z = -103) = 6.5 \approx -103 \sin(3.6°) \tag{1.3}$$

Chapter 2

Material study

This chapter is dedicated to the definition of the composite material that will be considered for the design of the leaf spring. Material selection is performed to determine the choice of laminate material and its associated material properties are gathered. Manufacturing processes are then discussed.

2.1 Material selection

Based on literature, there are mainly 2 families of composite materials that are used to manufacture transverse leaf springs: glass fiber reinforced polymers (GFRP) and carbon fiber reinforced polymers (CFRP). Materials from both families usually consist in a fiber reinforcement held by the means of a resin matrix, which is called a ply. Plies are then stacked together with specific angles to form a laminate. The most commonly encountered type of laminate ply is the E-Glass/Epoxy. It is a GFRP with E-type glass fibers, which stands for low electrical conductivity type of glass fibers, held together by the means of epoxy resin. Other types of plies are listed in Table 2.1.

GFRP		**CFRP**	
Material	Reference(s)	Material	Reference(s)
E-Glass/Epoxy	[7], [28]	HT-Carbon/epoxy	[7], [8]
E-Glass/Vinyl Ester	[28]		
S2-Glass/Epoxy	[7]		

Table 2.1: Common plies for composite transverse leaf springs.

The candidate material is required to have a high specific strain energy, as it ensures that the leaf spring will have a lower mass. The specific strain energy can be written

$$S = \frac{1}{2}\frac{\sigma_t^2}{\rho E}, \tag{2.1}$$

where σ_t is the allowable stress, ρ is the material density and E is the Young's modulus of elasticity. For the suspension application, it is required to have a high specific strain energy in static loading but more importantly a high specific strain energy in dynamic loading, as most loads applied on a suspensions are dynamic. Fig. 2.1 highlights specific strain energies of candidate spring materials from Table 2.1 in both static and dynamic loading. The strain energies are expressed as a relative percentage of the reference value obtained for the S2-Glass/Epoxy and the hatched region corresponds to the dynamic loading strain energy.

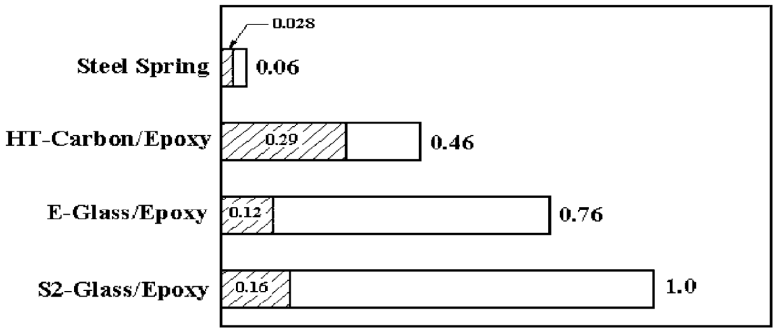

Figure 2.1: Specific strain energies of the spring candidate materials [29].

As shown in Fig. 2.1, HT-Carbon/Epoxy is the most suited materials as its specific strain energy in dynamic loading is the highest. However, its low impact strength [7] may cause a suspension failure in case of contact. HT-Carbon is also subjected to galvanic corrosion [29], which can also lead to suspension failure over time. The cost is also more important compared to glass fibers, as shown in Fig. 2.2.

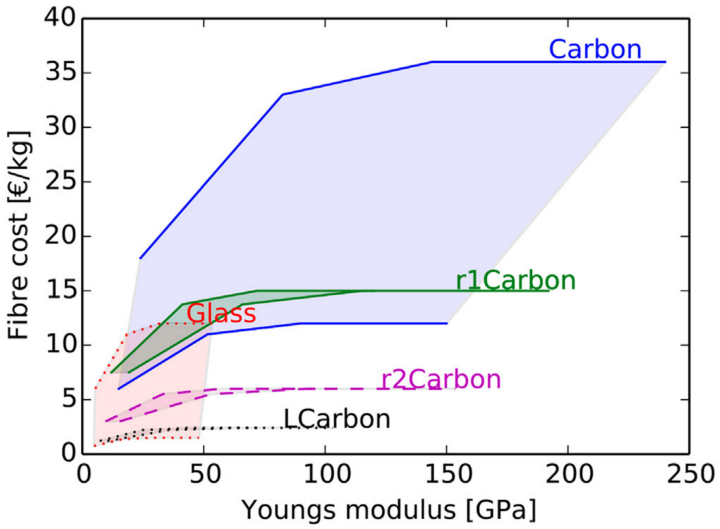

Figure 2.2: Cost of fibers with increasing reinforcement performance [30].

The selection is therefore narrowed up to E- and S2-Glass/Epoxy which have higher impact strength and galvanic corrosion resistance for a lower cost. S2-Glass/Epoxy has a better specific strain energy compared to E-Glass/Epoxy due to its higher Young's modulus of elasticity but also costs more. In a perspective of a mass produced leaf spring for the automotive industry, the slight increase in specific strain energy in dynamic loading brought by the S2-Glass fiber is not justified compared to the increase of the costs. S2-Glass fibers would however be much more suited for high end applications of the leaf spring, such as sport cars.

2.2 Material properties

For the design of the leaf, mechanical properties of the lamina in the material axes are required, namely: Young's modulus in the fiber (longitudinal) direction E_{11}, Young's modulus in the transverse direction E_{22}, shear modulus G_{12}, major Poisson's ratio ν_{12}, minor Poisson's ratio ν_{21}, longitudinal tensile and compressive strengths σ_1^T and σ_1^C, transverse tensile and compressive strengths σ_2^T and σ_2^C, shear strength τ_{12} and density ρ. For E-Glass/Epoxy plies, part of these mechanical properties are reported in Table 2.2.

Property	E_{11}	E_{22}	G_{12}	ν_{12}	σ_1^T	σ_1^C	σ_2^T	σ_2^C	τ_{12}	ρ
Units	[GPa]	[GPa]	[GPa]	[-]	[MPa]	[MPa]	[MPa]	[MPa]	[MPa]	$[kg/m^3]$
E-Glass/epoxy	39	8	3.7	0.28	1082	620	39	128	89	2000

Table 2.2: Mechanical properties of the E-Glass/Epoxy laminate plies [31].

Another mechanical property, the minor Poisson's ratio ν_{21}, is determined using the reciprocity relation.

$$\frac{\nu_{12}}{E_{11}} = \frac{\nu_{21}}{E_{22}} \Rightarrow \nu_{21} = \nu_{12}\frac{E_{22}}{E_{11}} = 0.0574. \tag{2.2}$$

2.3 Manufacturing processes

Manufacturers such as BMW and Mubea [32] resort to (low pressure) Resin Transfer Molding (RTM) and High Pressure Resin Transfer Molding (HP-RTM) when manufacturing their GFRP and CFRP components. These processes are particularly well suited for automation and mass production as their cycle time are relatively short. HP-RTM is the fastest of the two process, with cycle times of less than 10min compared to 30min for the RTM process. HP-RTM also allows to create complex geometries, such as sideframes for the BMW i3 [32]. This process however requires a more consequent investment in the machinery and in the computation of the pressure, which can become complex depending on the manufactured geometry. Process cycles for both processes are pictured in Fig. 2.3.

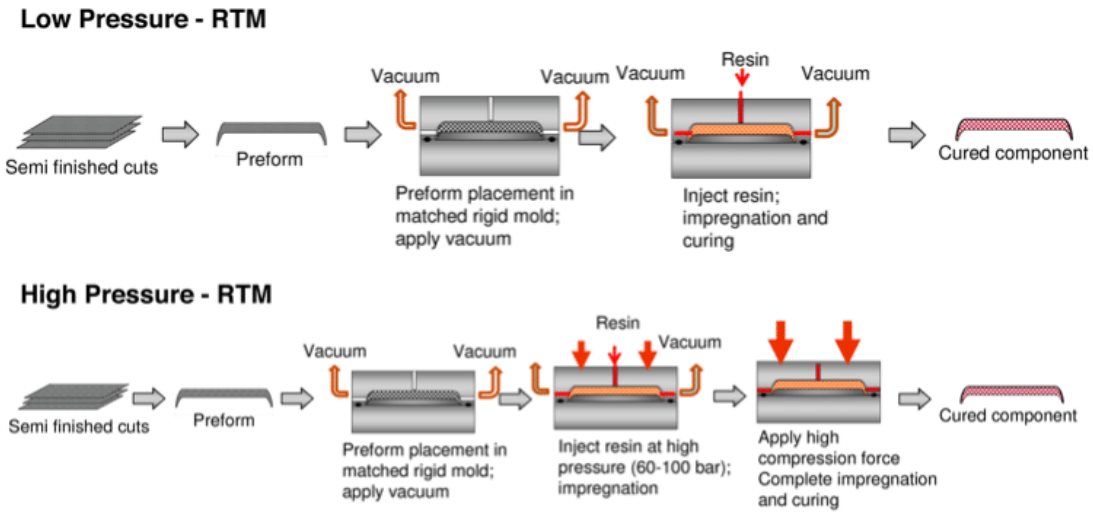

Figure 2.3: Low pressure resin transfer molding (RTM) and high-pressure resin transfer molding (HP-RTM) process cycles [33].

Another possible process for the manufacturing of composite leaf springs is the use of Short Moulding Compound (SMC), as advised by Pr. Michaël Bruyneel in a discussion. Interests in SMC are growing in the automotive industry, as it is one of the cheapest process for the production of composite structures and particularly well-suited for mass production [34]. SMC are ready-to-mould GFRP or CFRP materials usually delivered in the form of rolls. These are manufactured by dispersion of chopped carbon or glass fibers in a bath of thermoset resin (*e.g.* epoxy), as pictured in Fig. 2.4. Due to this process, the compound is relatively homogeneous, which could be detrimental in the manufacturing of leaf springs as it is preferred to have anisotropy in the material. However, processes exist in which the fibers are forced towards an unidirectional direction. SMC are usually put into shape using compression moulding [34].

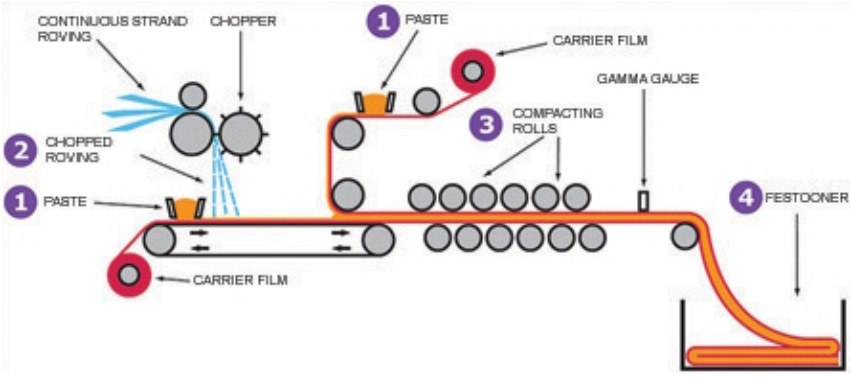

Figure 2.4: Manufacturing process of short moulding compounds [35].

Chapter 3

Analytical study

Before stating the analytical methodology for the computation of the preliminary design of the leaf, different possible suspension designs are derived based on the type of suspension members the leaf integrates. The leaf spring is then modeled accordingly to its design requirements combining beam and laminate theories, allowing to express its deformation when subjected to loading cases. After that, a methodology for the computation of the suspension forces is defined and a kinematic model of the suspension is created. Beforehand, some specific preliminary assumptions are made on the design:

- The transverse leaf spring is a single component that links the right and left sides of the suspension;
- The leaf is placed at the lower arms, as positioning the leaf on the upper arms would lead to a reduction of the trunk space;
- To avoid altering the design of the car, the position of the leaf supports are those of the lower arm.

These assumptions, which are common to most transverse leaf spring suspension designs, lead to the general schematic of the transverse leaf suspension pictured in Fig. 3.1.

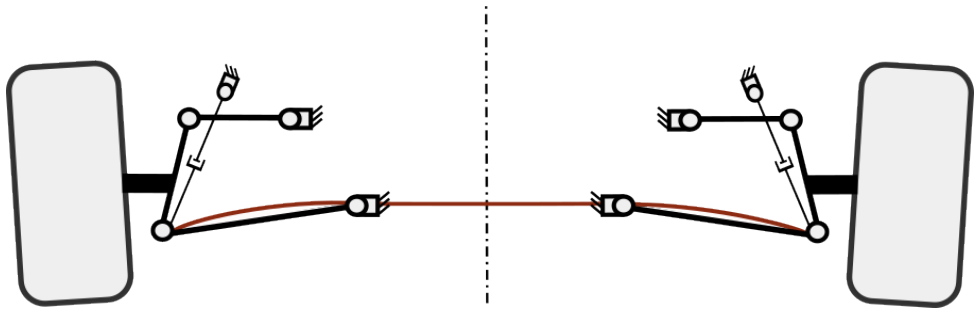

Figure 3.1: Front view plane schematic of a double wishbone suspension with the coil spring replaced by a leaf spring (orange).

3.1 Modified suspension design

Following the state of the art on transverse leaf springs, 4 different design possibilities of the suspension are derived based on the number of suspension elements the leaf integrates, *i.e.* the "integration degree" of the leaf spring. These degrees are depicted in Table 3.1.

Integration degree	Integrated suspension members			Example
	Coil spring	Anti-roll bar	Lower arm	
1	✓	×	×	Chevrolet Corvette C3 [14]
2a	✓	✓	×	Chevrolet Corvette C5 [19]
2b	✓	×	✓	BMW (concept i3) [2]
3	✓	✓	✓	Mubea [21]

Table 3.1: Possible integration degrees of the leaf spring in the suspension design.

In terms of suspension design, each integration level requires one or two modifications of the initial suspension diagram pictured in Fig. 3.1. Integrating the coil spring is simply done by linking its ends to movable parts (here the lower spherical joint) of the left and right suspension of the axle and fixing them to the car body by the mean of clamps. Even though the main goal is to sustain vertical loading, those clamps often allow a small lateral (y-axis) and longitudinal (x-axis) motion in the form of bushings as, in practice, suspension arms are not infinitely rigid. When the lower arm is removed, the clamp must sustain loading in all directions. To integrate the anti-roll bar (ARB) properties in the leaf, the clamps are replaced by hinges allowing rotation of the leaf around the x-axis. As a matter of simplicity, bushing will not be modeled in this section. Nonetheless, it will be considered that for cases where the lower arm is not removed, the leaf does not experience any longitudinal (x-axis) forces due to these bushings. For those cases also, no external transversal (y-axis) forces will be considered except the ones rising from the tension/compression caused by the geometry of the suspension. The different integration degrees are pictured in Fig. 3.2.

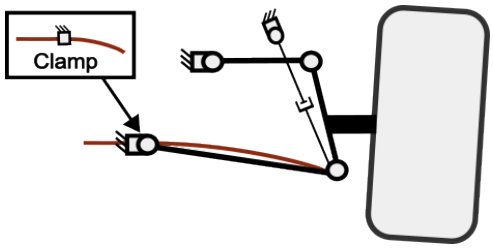

(a) Coil spring

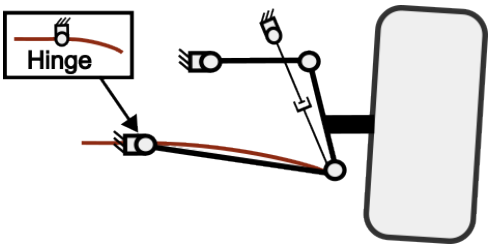

(b) Coil spring + ARB

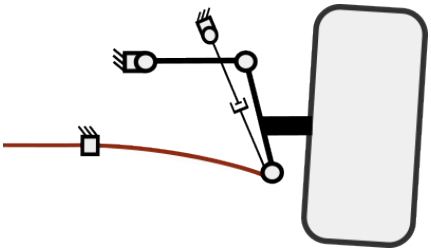

(c) Coil spring + lower arm

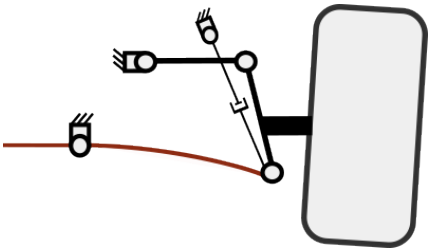

(d) Coil spring + ARB + lower arm

Figure 3.2: Schematics of the integration degrees 1 (a), 2a (b), 2b (c) and 3 (d).

3.2 Leaf spring modeling

To predict the behavior of the leaf spring under loading cases, an accurate analytical model of the leaf is sought. This model is obtained by a combination of laminate and beam theory particularised to the integration degrees of the leaf expressed in Section 3.1.

3.2.1 Deformed composite structure

To compute deformation and stresses of a composite laminate, effective properties of the laminate are computed by determining the properties of the individual laminae. The associated analytical process is known as the *Classical Laminated Plate Theory* (CLPT) [31] [36], which is a combination of the classical laminate plate and thin structure theories. The latest, also known as the Kirchhoff–Love theory of plates, is based on the following Kirchhoff assumptions [36]:

- Assumptions related to thin plates:
  - Plate initially flat and of constant thickness;
  - Thickness / width ≤ 0.2;
  - Transverse displacement / thickness ≤ 0.2.
- Assumptions related to the behaviour under loading:
  - A segment initially normal to the mid-plane remains straight and normal to the mid-plane in the deformed state;

– The normal stresses perpendicular to the mid-plane are negligible;

– Displacements of the points belonging to the mid-plane of the plate are perpendicular to this plane (bending).

A general laminate can be subjected to both in-plane and out-of-plane loading. Following CLPT, resulting strains $\boldsymbol{\epsilon}$ and curvature $\boldsymbol{\kappa}$ are continuous through the laminate whilst stresses $\boldsymbol{\sigma}$ are continuous only within the plies, as the ply moduli are discontinuous due to various orientations of the plies. This variation of strain and stresses is shown in Fig. 3.3.

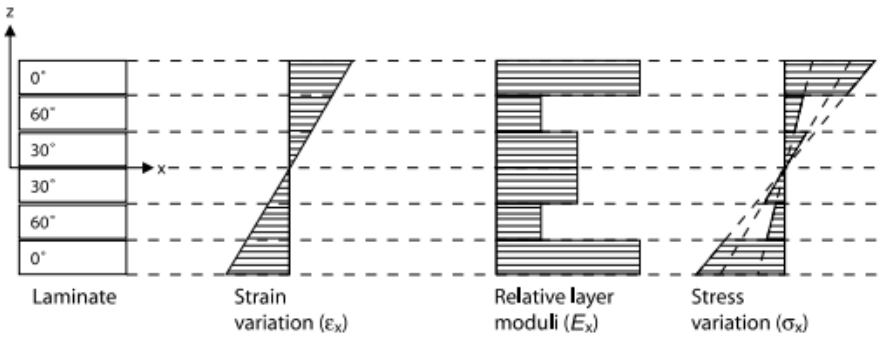

Figure 3.3: Strain and stress variation in a laminate subjected to bending [31].

Due to this discontinuity of the stresses, applied loads are defined in terms of their stress resultants. As pictured in Fig. 3.4, this leads to three in-plane (N_x, N_y, N_{xy}) and three out-of-plane (M_x, M_y, M_{xy}) resultants in the structural axes (x, y, z). Please note that the structural and material axes that are written in this report follow the convention established in [31] which is a different convention from [36].

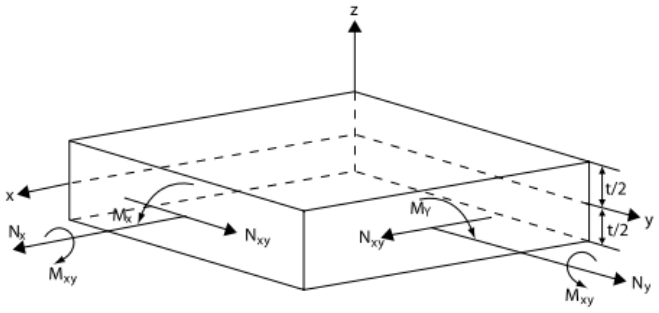

Figure 3.4: Material axes and associated in-plane and out-of-plane loads for the ply [31].

For composites, these resultants are found by integrating the ply stresses through the thickness of the laminate:

$$\boldsymbol{N} = \begin{Bmatrix} N_x \\ N_y \\ N_{xy} \end{Bmatrix} = \int_{-h/2}^{h/2} \begin{Bmatrix} \sigma_x \\ \sigma_y \\ \sigma_{xy} \end{Bmatrix} dz \qquad (3.1) \qquad \boldsymbol{M} = \begin{Bmatrix} M_x \\ M_y \\ M_{xy} \end{Bmatrix} = \int_{-h/2}^{h/2} z \begin{Bmatrix} \sigma_x \\ \sigma_y \\ \sigma_{xy} \end{Bmatrix} dz \qquad (3.2)$$

From Eq. (3.1) and Eq. (3.2), it comes

$$\begin{Bmatrix} \sigma_x \\ \sigma_y \\ \sigma_{xy} \end{Bmatrix} = \begin{pmatrix} \overline{Q_{11}} & \overline{Q_{21}} & \overline{Q_{16}} \\ \overline{Q_{12}} & \overline{Q_{22}} & \overline{Q_{26}} \\ \overline{Q_{16}} & \overline{Q_{26}} & \overline{Q_{66}} \end{pmatrix} (\boldsymbol{\epsilon}^0 + z\boldsymbol{\kappa}) = \mathbf{Q}_{x,y,z}\boldsymbol{\epsilon} \tag{3.3}$$

where $\mathbf{Q}_{x,y,z}$ is the reduced stiffness matrix in the structural axes and $\boldsymbol{\epsilon}^0$ are the membrane strains due to in-plane deformation. The reduced stiffness matrix $\mathbf{Q}_{x,y,z}$ is obtained by rotation of the reduced stiffness matrix in the material axes $\mathbf{Q}_{1,2,3}$ which writes

$$\mathbf{Q}_{1,2,3} = \begin{pmatrix} Q_{11} & Q_{12} & 0 \\ Q_{21} & Q_{22} & 0 \\ 0 & 0 & Q_{66} \end{pmatrix} = \begin{pmatrix} m\ E_{11} & m\ \nu_{21}\ E_{11} & 0 \\ m\ \nu_{12}\ E_{22} & m\ E_{22} & 0 \\ 0 & 0 & G_{12} \end{pmatrix} \tag{3.4}$$

with $m == \frac{1}{1-\nu_{xy}\nu_{yx}}$. The transformation from the material to the structural axes writes

$$\begin{Bmatrix} \overline{Q_{11}} \\ \overline{Q_{22}} \\ \overline{Q_{12}} \\ \overline{Q_{66}} \\ \overline{Q_{16}} \\ \overline{Q_{26}} \end{Bmatrix} = \begin{pmatrix} c^4 & s^4 & 2c^2s^2 & 4c^2s^2 \\ s^4 & c^4 & 2c^2s^2 & 4c^2s^2 \\ c^2s^2 & c^2s^2 & c^4+s^4 & -4c^2s^2 \\ c^2s^2 & c^2s^2 & -2c^2s^2 & (c^2-s^2)^2 \\ c^3s & -cs^3 & cs^3-c^3s & 2(cs^3-c^3s) \\ cs^3 & c^3s & c^3s-cs^3 & 2(c^3s-cs^3) \end{pmatrix} \begin{Bmatrix} Q_{11} \\ Q_{22} \\ Q_{12} \\ Q_{66} \end{Bmatrix} \tag{3.5}$$

where $c = \cos(\theta)$ and $s = \sin(\theta)$. θ is the orientation of the ply. For the laminate, the general form of the laminate stress-strain relation is finally given by Eq. (3.6).

$$\left[\begin{array}{c} N_x \\ N_y \\ N_{xy} \\ \hline M_x \\ M_y \\ M_{xy} \end{array}\right] = \left[\begin{array}{ccc|ccc} A_{11} & A_{21} & A_{16} & B_{11} & B_{21} & B_{16} \\ A_{12} & A_{22} & A_{26} & B_{12} & B_{22} & B_{26} \\ A_{16} & A_{26} & A_{66} & B_{16} & B_{26} & B_{66} \\ \hline B_{11} & B_{21} & B_{16} & D_{11} & D_{21} & D_{16} \\ B_{12} & B_{22} & B_{26} & D_{12} & D_{22} & D_{26} \\ B_{16} & B_{26} & B_{66} & D_{16} & D_{26} & D_{66} \end{array}\right] \left[\begin{array}{c} \epsilon_x^0 \\ \epsilon_y^0 \\ \gamma_{xy}^0 \\ \hline \kappa_x \\ \kappa_y \\ \kappa_{xy} \end{array}\right] \tag{3.6}$$

Particularised to a laminate with constant h_0 thick plies, matrices $\mathbf{A}$, $\mathbf{B}$ and $\mathbf{D}$ are given by Eq. (3.7)

$$A_{ij} = h_0 \sum_{t=1-n/2}^{n/2} Q_{ij}^t (t - (t-1)) \tag{3.7a}$$

$$B_{ij} = \frac{h_0^2}{2} \sum_{t=1-n/2}^{n/2} Q_{ij}^t (t^2 - (t-1)^2) \tag{3.7b}$$

$$D_{ij} = \frac{h_0^3}{3} \sum_{t=1-n/2}^{n/2} Q_{ij}^t (t^3 - (t-1)^3) \tag{3.7c}$$

where n is the number of plies in the laminate and t the position of the ply with respect to the middle plane.

Matrix **B** is commonly referred as the stretching-bending coupling matrix. If at least one $B_{ij} \neq 0$, the laminate will warp due to a purely in-plane load (Fig. 3.5a) or stretch due to a pure bending moment. To avoid such effects, the laminate is required to be symmetric along the mid-plane of the stacking sequence. Such stacking sequence is denoted with a 'S' subscript (*e.g.* $[0/90]_S$).

Non-zero A_{16} and A_{26} terms of the **A** matrix are responsible for the coupling between extensional stresses (ϵ_x^0 and ϵ_y^0) and shear strains (γ_{xy}^0). This coupling can lead to the laminate deformation pictured in Fig. 3.5b. To avoid these coupling terms, the laminate is required to consist only of 0° and 90° oriented plies or that all angle plies are balanced. A laminate is said balanced if for each ply at θ with thickness h, another ply oriented at $-\theta$ with thickness h exists (*e.g.* $[0/+\text{-}30/90]_T$, where the subscript 'T' denotes the total laminate).

Non-zero D_{16} and D_{26} terms of the **D** matrix are responsible for the coupling between bending and torsion of the laminate, as pictured in Fig. 3.5c. This can be avoided in the same way as avoiding tension-shear coupling.

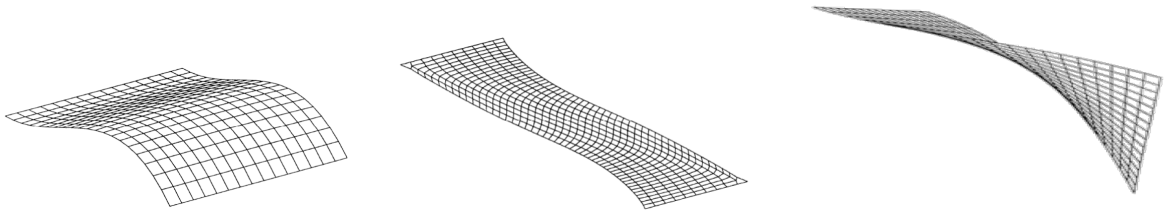

(a) Stretching-bending **(b)** Tension-shear **(c)** Bending-torsion

Figure 3.5: Stretching-bending (a), tension-shear (b) and bending-torsion (c) coupling effects on the laminate [36].

For a laminate that is both balanced and symmetric, all coupling terms vanish and

Eq. (3.6) becomes Eq. (3.8) and Eq. (3.9)

$$\begin{bmatrix} N_x \\ N_y \\ N_{xy} \end{bmatrix} = \begin{bmatrix} A_{11} & A_{21} & 0 \\ A_{12} & A_{22} & 0 \\ 0 & 0 & A_{66} \end{bmatrix} \begin{bmatrix} \epsilon_x^0 \\ \epsilon_y^0 \\ \gamma_{xy}^0 \end{bmatrix} \tag{3.8}$$

$$\begin{bmatrix} M_x \\ M_y \\ M_{xy} \end{bmatrix} = \begin{bmatrix} D_{11} & D_{21} & 0 \\ D_{12} & D_{22} & 0 \\ 0 & 0 & D_{66} \end{bmatrix} \begin{bmatrix} \kappa_x \\ \kappa_y \\ \kappa_{xy} \end{bmatrix} \tag{3.9}$$

From there, effective engineering properties are computed in Eq. (3.10)

$$E_x = \frac{1}{h}\left[A_{11} - \frac{A_{12}^2}{A_{22}}\right] \tag{3.10a}$$

$$E_y = \frac{1}{h}\left[A_{22} - \frac{A_{12}^2}{A_{11}}\right] \tag{3.10b}$$

$$\nu_{xy} = \frac{A_{12}}{A_{22}} \tag{3.10c}$$

$$G_{xy} = \frac{A_{66}}{h} \tag{3.10d}$$

where h is the total laminate thickness.

For the design of the leaf, the stacking sequences is chosen balanced and symmetric to avoid these coupling terms which may be detrimental for the performance of the leaf spring.

3.2.2 Beam theory

Beam theory assumptions are first discussed to define the most accurate analytical model for the leaf. Beam theory is then particularised according to the different transverse leaf spring design possibilities expressed in Section 3.1.

3.2.2.1 Curved beam theory

Deflection of curved beams is mostly computed based on energy methods, *e.g.* Castigliano's second theorem. Such computations can lead to highly non-linear equations, as the beam deflection involves large deformation in the of a leaf spring [37]. However, for a curved beam with a large radius, straight beam theory can be used under one condition on the thickness of the beam. The condition writes [31, p. 275]: *'If for a curved beam, the radius of curvature is large enough (10 times the thickness), the stress distribution along the depth is very nearly linear and the complementary energy of flexure is given with sufficient accuracy by the straight beam theory. If, in addition, the angular span is*

great enough such that deformations due to axial stress from the normal force N and the shear stresses due to transverse shear V can be neglected, deflections and rotations can be deduced from straight beam theory.'

Considering the leaf initially has a constant curvature R (due to the manufacturing), the radius of curvature can be evaluated using the geometry of the suspension under the no-loading assumption (F_z = 0N). R is computed based both for a cantilever beam (integration degrees 1 and 2b) and an overhanging beam (integration degrees 2a and 3).

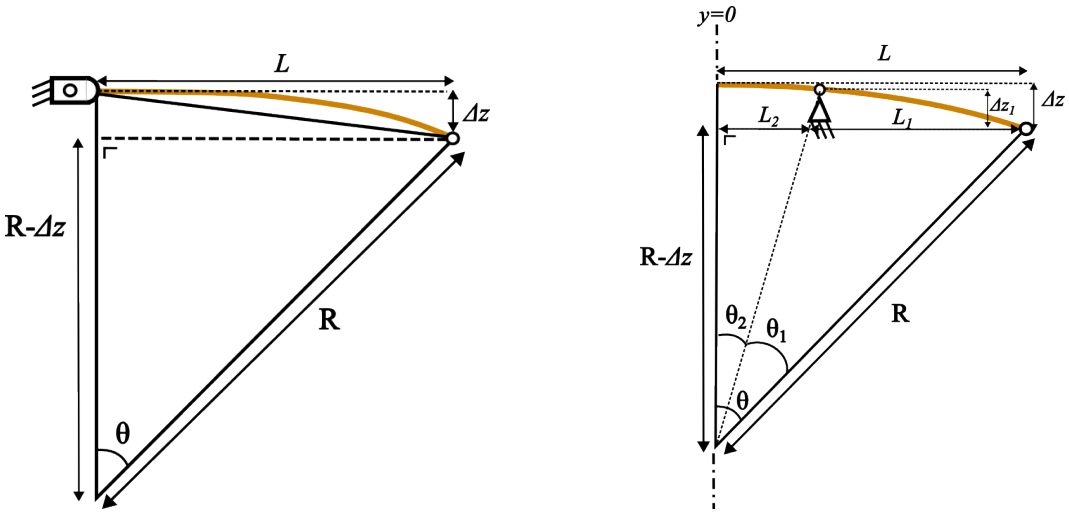

(a) Cantilever beam **(b)** Overhanging beam

Figure 3.6: Computation of the constant curvature radius in the case of the cantilever (a) and the overhanging beam (b).

In both cases, the radius of curvature R writes

$$R = L^2 \frac{1}{2\Delta z} + \frac{\Delta z}{2} \tag{3.11}$$

where L is the distance from the eye of the leaf to the straight part of the leaf and Δz is the vertical offset of the eye with respect to straight part of the leaf. The angular span θ yields in both cases

$$\theta = \sin^{-1}(\frac{L}{R}). \tag{3.12}$$

For the cantilever beam, Eq. (3.11) can be solved straight from the geometry of the suspension in Fig. 3.6a, which is computed with the method presented in Section 3.3.2. This gives a radius of curvature R = 468mm and an angular span of θ = 46° (in the case the lower arm). Therefore, requirements for the straight beam theory are met, since in practice the thickness of a leaf spring lies between 10mm and 20mm ($< \frac{1}{10}R$).

For the overhanging beam, more calculation is required since the distance $\Delta z - \Delta z_1$ is unknown. Based on the geometry in Fig. 3.6b, one can find the radius of curvature

R = 1300mm. This leads to an angular span of 31°. Like the cantilever beam, requirements are met for the overhanging beam.

3.2.2.2 Euler-Bernoulli beam theory

As deduced in previous section, the leaf can be represented by using a straight beam under transverse deformation. Classical beam theory, also known as Euler-Bernoulli beam theory, provides a solution for the deformation of a beam. The Euler-Bernoulli equation expresses the relationship between the load and the deflection, which writes in the xz-axes

$$\frac{d^2}{dx^2}\left(EI\frac{d^2w}{dx^2}\right) = q, \tag{3.13}$$

where E is the Young's modulus, I is the second moment of area of the beam's cross section, w the deflection in the vertical (z-axis) direction and q is a distributed load. Note that for the leaf spring application, the x-axis of the beam is replaced by the y-axis of the car, hence Eq. (3.13) writes

$$\frac{d^2}{dy^2}\left(EI\frac{d^2w}{dy^2}\right) = q, . \tag{3.14}$$

This equation can be particularised with the boundary conditions and loads applied on the beam. Books such as *'Roark's principle of Roark's Formulas for Stress and Strain'* [31] provide tables with particularised solutions to the Euler-Bernoulli equations for common beam problems encountered in practice, with, as most known example, the cantilever beam. These tables are used to model the leaf depending on the integration degree established earlier in Table 3.1.

In the case the leaf is clamped to the body, *i.e.* no anti-roll bar integration, the leaf spring can be represented by a cantilever beam carrying a point load on its free end. This deflection (in small deformation) is illustrated in Fig. 3.7.

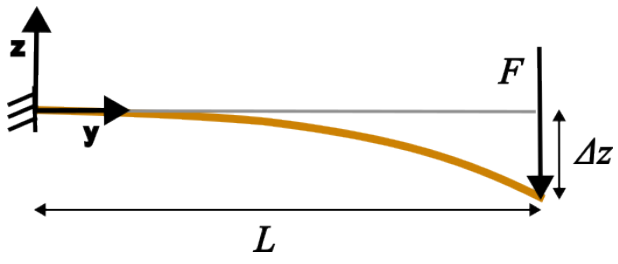

Figure 3.7: Deflection of a cantilever beam subjected to a point load at its free end in small deformation assumption.

In this case, the deformation writes for any point of the lead

$$\Delta z(y) = \frac{Fy^2}{6EI}(3L - y). \tag{3.15}$$

The maximum deflection at the free end is therefore given by

$$\Delta z_{max} = \frac{FL^3}{3EI}. \tag{3.16}$$

In the case the leaf is fixed through hinges to the body, *i.e.* anti-roll bar integration, the leaf spring can be represented by a overhanging beam carrying a point load on its free end(s). This deflection (in small deformation) is illustrated in Fig. 3.8.

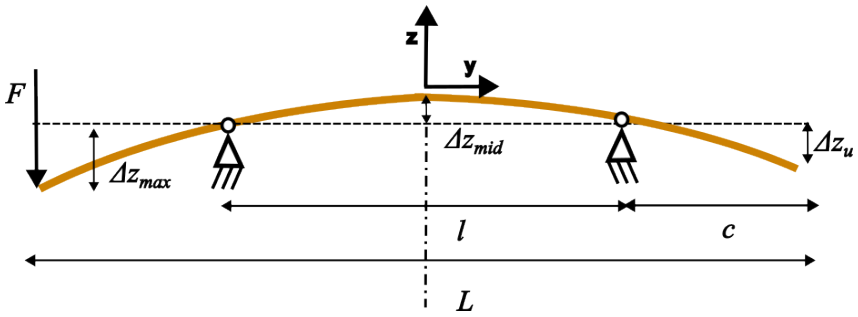

Figure 3.8: Deflection of a overhanging beam subjected to a point load at its free end in the small deformation assumption.

In this case, the deformation writes for any point of the leaf

$$\begin{cases} \Delta z(y) = \dfrac{F(y+\frac{l}{2})}{6EI}\left[3c(y+\frac{l}{2}) - (y+\frac{l}{2})^2 + 2cl\right] & \text{, for } y \in \left[-\dfrac{L}{2}; -\dfrac{l}{2}\right] \\ \Delta z(y) = -\dfrac{Fc(y-\frac{l}{2})}{6EIl}(l - y + \frac{l}{2})(2l - y + \frac{l}{2}) & \text{, for } y \in \left[-\dfrac{l}{2}; \dfrac{l}{2}\right] \\ \Delta z(y) = \dfrac{Fcl(y-\frac{l}{2})}{6EI} & \text{, for } y \in \left[\dfrac{l}{2}; \dfrac{L}{2}\right] \end{cases} \tag{3.17}$$

The maximum deflection at the loaded free end is therefore given by

$$\Delta z_{max} = \frac{Fc^2}{3EI}(c+l), \tag{3.18}$$

and the deformation on the unloaded end is given by

$$\Delta z_u = \frac{Fc^2 l}{6EI}, \tag{3.19}$$

The deformation at the center of the leaf also writes

$$\Delta z_{mid} = -\frac{Fcl^2}{16EI}. \tag{3.20}$$

In practice, the suspension experiences forces at both wheels, leading to a static charge at both ends of the leaf. The load acting on the leaf is pictured in Fig. 3.9.

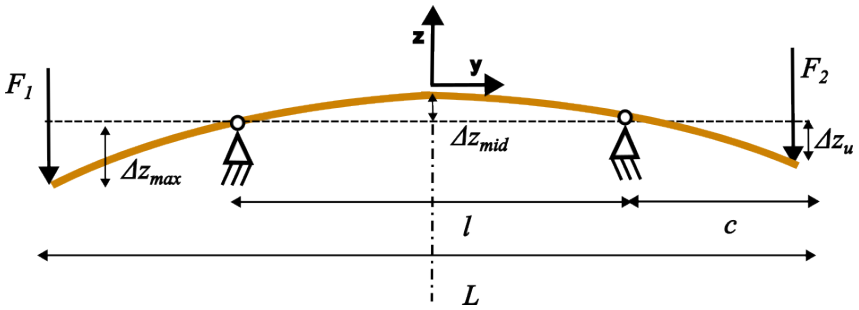

Figure 3.9: Deflection of a overhanging beam subjected to a point load on both free ends in the small deformation assumption.

The solution for this deflected beam is found using the principle of superposition with the contribution of each force. In the case $F_1 = F_2$, which is the load case for the computation of the static vertical force in the contact patch, maximum deformation occurring at the ends of the leaf writes

$$\Delta z_{max} = \frac{Fc^2}{6EI}(2c + 3l). \tag{3.21}$$

The deflection at the center of the beams writes

$$\Delta z_{mid} = -\frac{Fcl^2}{8EI}. \tag{3.22}$$

Two limitations however arise from the Euler-Bernoulli beam theory: transverse shear deformation is neglected and the deflection along y is neglected by the assumption of small displacements. While the first limitation is investigated in Section 3.2.2.3, the second is discussed hereafter. The assumption of small displacements is often valid for the computation of beam deflection, as for most of the cases, beams are structural elements that undergo really small displacement. However, in the case of a leaf spring, the deflection is well beyond the assumption of small displacements. If there were no lateral deflection Δy for a large deformation, this would mean that the beam elongates, which should not happen under the pure bending assumptions. In the case of large displacements, the deformation of the cantilever beam can be pictured as in Fig. 3.10.

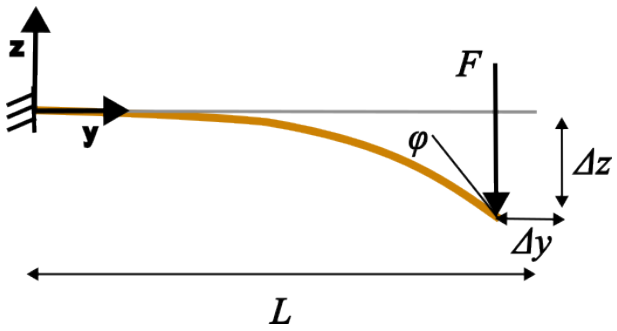

Figure 3.10: Deflection of a cantilever beam subjected to a point load at its free end in small deformation assumption.

A solution to determine the lateral deflection Δy of a cantilever beam in large deformations is proposed by Kashi Nath Saha and Sushanta Ghuku [37]. This relation, written in current yz-coordinates, yields

$$y(s) = \frac{L}{\sqrt{\alpha}}\left(\sqrt{\sin(\psi_{tip})} - \sqrt{\sin(\psi_{tip}) - \sin(\psi_{tip})}\right), \tag{3.23}$$

where s is the coordinate along the beam in the curvilinear coordinate system, L is the length of the leaf (constant due to pure bending assumption), $\alpha = \frac{FL^2}{2EI}$ is a normalised load parameter, ψ_{tip} is the deflection angle at the free end (whose value might differ from the small deformation case) and $\psi(s)$ is the deflection angle at the considered point. Computing the deflection at the free, it comes $\psi(s) = \psi_{tip}$ and Eq. (3.23) becomes

$$\Delta y = L - y_{tip} = L\left(1 - \sqrt{\frac{\sin(\psi_{tip})}{\alpha}}\right). \tag{3.24}$$

The authors provide a relationship linking α to ψ_{tip}, which is pictured in 3.11.

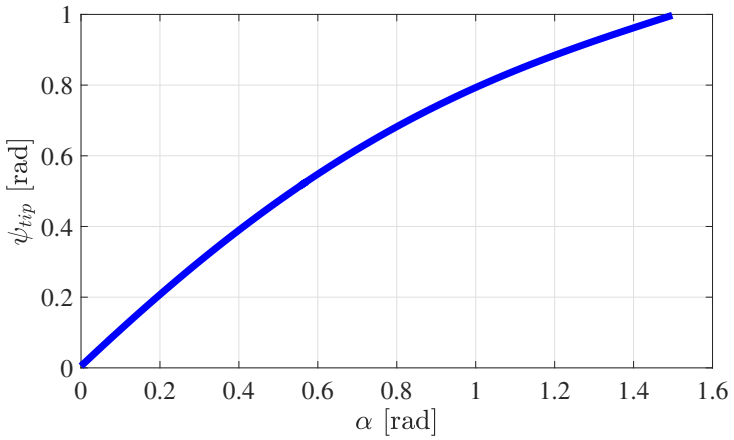

Figure 3.11: Relation between the normalised load parameter α and the angle of deflection ψ_{tip} for a cantilever beam in large deformation [37].

As it can be seen in the graph, the value of α is the same as ψ_{tip} for low values of α. In fact, for a low load parameter, the small deformation solution is retrieved as

$$\lim_{\alpha \to 0} \frac{sin(\alpha)}{\alpha} = 0 \Rightarrow y = 0. \tag{3.25}$$

For the particular case of the current suspension design, the maximum value of α in the suspension stroke can be computed with the complete configuration of the suspension in jounce/rebound (see Section 3.3.2). A first guess of α is then computed based on the vertical deflection in the minimum rebound position

$$\alpha = \frac{FL^2}{2EI} = \frac{K\Delta z L^2}{2EI} = \frac{3\Delta z}{2L} = \frac{3 * 141}{2 * 363} = 0.58. \tag{3.26}$$

As it can be observed in 3.11, the value of ψ is close to the one of α for $\alpha < 0.6$. Therefore, the assumption could be made that these two values are equal for the suspension geometry, hence

$$\psi = \alpha = \frac{3\Delta z}{2L}. \tag{3.27}$$

However, using this assumption leads to a difference of 10mm in the lateral displacement of point B for the minimum rebound position. On the scale of the suspension, this leads to a significant change in the suspension behavior, mainly on the camber angle which becomes too big. To avoid this, an analytical expression is used. [38] provides a 10^{th} order polynomial approximating the $\alpha - \phi$ relation, which is written in Eq. (3.28).

$$\begin{aligned}\phi(\alpha) = 0.5(2\alpha) - 0.0458333(2\alpha)^3 + 0.00893105(2\alpha)^5 \\ - 0.00223058(2\alpha)^7 + 9.0927 \cdot 10^6(2\alpha)^9.\end{aligned} \tag{3.28}$$

Finally, Eq. (3.24) writes

$$\Delta y = L\left(1 - \sqrt{\frac{\sin(\psi_{tip})}{\alpha}}\right) = L\left(1 - \sqrt{\frac{\sin(\frac{3\Delta z}{2L})}{\frac{3\Delta z}{2L}}}\right). \tag{3.29}$$

Please note that, even though straight beam theory is used, the deflection of an initially curved beam with constant curvature is well approximated by this method, as shown by Kashi Nath Saha and Sushanta Ghuku's results [37]. It is however expected that the lateral deflection Δy will be slightly larger for the initially curved beam. This behavior of the beam under large deformation is later verified using a finite element model.

In the case of the overhanging beam, no equivalent analytical expression for the large deformation of the leaf spring could be found in the literature, as it is less studied than the cantilever beam. This means that, in this case, it would be necessary to use Timoshenko's beam theory to derive the analytical expression of the lateral deflection in large deformations of the beam [38]. This would lead to rather heavy ordinary differential equations (ODEs) that require numerical tools to solve. This methodology is however too computationally demanding for a preliminary design. Therefore, the large deformation of the leaf spring with integration degree 3 will be assumed the same as for the case where the lower arm is not suppressed (*i.e.* integration degree 2a). The real behavior under large deformation of the overhanging beam is later verified using a finite element model.

3.2.2.3 Bending of composite beams

If the laminate plate meets the requirements of a beam, the standard beam theory (Euler-Bernoulli) can be used [31]. The necessary requirements are that the width and the height must be much smaller than the length of the beam. This is the case for

the leaf spring as its length is approximately 1.4m which will be much larger than its width ($\approx$ 100mm) and its thickness ($\approx$ 15mm). For pure bending of the composite beam, additional assumptions [31] are also required:

1. The beam is of rectangular cross section;
2. Plies lie in the x-z plane;
3. The shear coupling terms $()_{16}$ and $()_{26}$ are zero.

The equivalent modulus E^* writes

$$E^* = (D_{11} - \frac{B_{11}^2}{A_{11}})\frac{12}{h^3}, \tag{3.30}$$

and can be particularised for a symmetric stacking sequence

$$E^* = D_{11}\frac{12}{h^3}. \tag{3.31}$$

This equivalent modulus can then be used within the standard beam theory to approximate the solution in bending. However, Euler-Bernoulli beam theory ignores transverse shear deformation, which is negligible for materials such as steel but might not be for composites. In fact, transverse shear deformation should not be ignored for laminates, as the shear modulus of the laminate is significantly smaller ($G_{\text{steel}} \approx 70\text{GPa}$ and $G_{\text{GFRP}} \approx 5\text{GPa}$). To take into account shear deformation, it is required to use Timoshenko's static beam theory [39], which writes for an homogeneous beam of constant cross section

$$EI\frac{d^4w}{dx^4} = q(x) - \frac{EI}{\kappa' AG}\frac{d^2q}{dx^2} \tag{3.32}$$

with I the second moment of area, A the cross section area, $q(x)$ a distributed load, w the vertical displacement of the mid-surface and κ' is the Timoshenko shear coefficient, which is equal to 5/6 for beams with rectangular cross sections. However, a criteria exists in Timoshenko's beam theory that allows to ignore shear deformation [39] which yields

$$\frac{3EI}{\kappa' L^2 AG} << 1. \tag{3.33}$$

If Eq. (3.33) is valid, then Timoshenko's beam theory simply writes as Euler-Bernoulli beam theory. For the leaf design, the procedure will therefore be the following:

1. Compute the geometry of the cross section of the leaf using its requirements (mainly stiffness K) and Euler-Bernoulli beam theory;
2. Assess Timoshenko's criteria in shear Eq. (3.33) using the computed geometry for the beam;

(a) If the criteria is valid, Euler-Bernoulli can be used for the analysis.

(b) If the criteria is not valid, Timoshenko beam theory has to be used (if possible).

Stresses are computed on a ply-by-ply basis. In the case of pure bending, it comes for ply k

$$\begin{Bmatrix} \sigma_x \\ \sigma_y \\ \sigma_{xy} \end{Bmatrix}_k = \mathbf{Q}^k_{x,y,z} z\boldsymbol{\kappa} = \mathbf{Q}^k_{x,y,z} z\mathbf{D}^{-1}\mathbf{M}. \tag{3.34}$$

3.2.2.4 Axial tension/compression of composite beams

The solution for the beam under pure axial loading is similar to the one for pure bending. Besides standard beam theory assumptions, the following assumptions (from [31]) also apply:

1. Plies lie in the x-z plane;
2. The shear coupling terms $()_{16}$ and $()_{26}$ are zero;
3. The laminate is balanced and symmetric.

For a beam of rectangular cross section with width b, the axial stiffness $(EA)^*$ writes

$$(EA)^* = bA_{11}. \tag{3.35}$$

In this case, stresses in ply k are given by Eq. (3.36).

$$\begin{Bmatrix} \sigma_x \\ \sigma_y \\ \sigma_{xy} \end{Bmatrix} = \begin{pmatrix} \overline{Q_{11}} & \overline{Q_{21}} & \overline{Q_{16}} \\ \overline{Q_{12}} & \overline{Q_{22}} & \overline{Q_{26}} \\ \overline{Q_{16}} & \overline{Q_{26}} & \overline{Q_{66}} \end{pmatrix}_k = \mathbf{Q}^k_{x,y,z}\boldsymbol{\epsilon}^0 = \mathbf{Q}^k_{x,y,z}\mathbf{A}^{-1}\mathbf{N} \tag{3.36}$$

3.2.3 Failure criterion

For anisotropic composite materials, one can evaluate if fracture occurs using the Tsaï-Wu failure criterion [36]. In the material axes, fracture occurs if the criterion is satisfied

$$F_i\sigma_i + F_{ij}\sigma_i\sigma_j = 1 \quad (i,j = 1,...,6) \tag{3.37}$$

$$F_1\sigma_1 + F_2\sigma_2 + F_6\sigma_6 + F_{11}\sigma_1^2 + F_{22}\sigma_2^2 + F_{66}\sigma_6^2 + 2F_{12}\sigma_1\sigma_2 = 1 \tag{3.38}$$

The coefficients F_i are computed based on the material properties:

$$F_1 = \frac{1}{\sigma_1^T} - \frac{1}{\sigma_1^C} \qquad F_{11} = \frac{1}{\sigma_1^T \sigma_1^C}$$
$$F_2 = \frac{1}{\sigma_2^T} - \frac{1}{\sigma_2^C} \qquad F_{22} = \frac{1}{\sigma_2^T \sigma_2^C}$$
$$F_6 = 0 \qquad F_{66} = \frac{1}{\tau_{12}^2}$$

$$F_{12} = -0.5\sqrt{F_{11}F_{22}} \tag{3.39}$$

From there, a safety criterion R can be introduced in the failure criterion

$$R = \frac{\sigma_i(a)}{\sigma_i} \tag{3.40}$$

where $\sigma_i(a)$ is the proportional load case. The criterion finally writes

$$F_i\sigma_i R + F_{ij}\sigma_i\sigma_j R^2 = 1. \tag{3.41}$$

Based on the value of the safety factor R, the safety of the design can be evaluated:

- If $R = \infty$: no stresses and strains;
- If $R > 1$: safe design;
- If $R = 1$: critical design leading to failure;
- If $R < 1$: hypothetical failure of the design.

3.3 Suspension modeling

As pointed out by David C. Barton and John D. Fieldhouse in *Automotive Chassis Engineering* [4], analysing the forces in a suspension is a complex problem that requires the use of FEA for static analysis of the suspension members and MBD for three-dimensional dynamic loading (road irregularities, accelerating, braking, cornering, etc). However, it is possible to carry out simple design calculations based on graphical representation of the suspension for a given load.

In this section, methodologies for the calculation of the static suspension forces are first defined. They are then paired with a kinematic model of the suspension to fully describe the suspension loads associated to the vertical motion of the wheel.

3.3.1 Suspension forces

David C. Barton and John D. Fieldhouse [4] provide methods to compute forces in the suspension members and mounting points. These methods and associated assumptions are described and particularised to the case of the short long arm suspension in the following sections.

3.3.1.1 Longitudinal loading

Longitudinal loads F_X due to aerodynamic drag, shocks, inboard brakes (non-conventional) or drive torque give rise to a resulting force with the center of the wheel as its effective point of application. The force acting at the center of the wheel is simply F_X, as illustrated in Fig. 3.12.

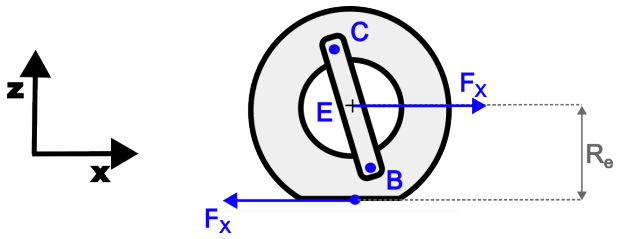

Figure 3.12: Free body diagram of the suspension in theside view plane for a longitudinal load acting in the contact patch.

For longitudinal loads due to outboard brakes (conventional) or drive torque in the case of live axles (*e.g.* beam axles), a resulting torque is reacted outboard a the hubs. This results in forces acting on the suspension arms as pictured in Fig. 3.13.

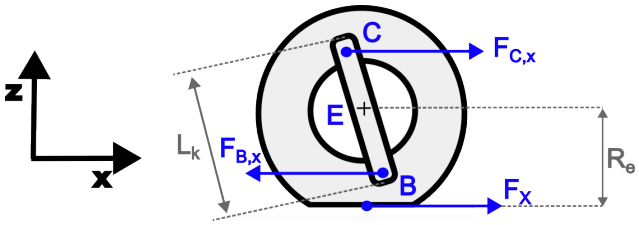

Figure 3.13: Free body diagram of the suspension in the side view plane in the case of outboard braking.

Using the equilibrium around the wheel center, forces acting on the arms yield

$$F_{C,x} = F_X \frac{BE}{CE} \frac{R_e}{L_k} \tag{3.42}$$

$$F_{B,x} = F_X \frac{CE}{BE} \frac{R_e}{L_k} \tag{3.43}$$

with $F_{C,x}$ the longitudinal force acting on the upper arm, $F_{B,x}$ the longitudinal force acting on the lower arm and L_k the length of the knuckle.

3.3.1.2 Vertical loading

To compute the forces in the suspension due to the static wheel load F_Z, the following assumptions are made:

1. Arms are considered as rigid links;
2. The loads due to the masses are ignored, as they are negligible compared to the loads due to F_Z;
3. Joints are considered pin joints to avoid friction effects, compliance in bushes and other effects that are difficult to model;
4. The problem can be treated in 2D in the front view plane.

These assumptions lead to the diagram of the double wishbone suspension as previously pictured in Fig. 3.1, with the leaf spring acting on the lower pin joint of the long arm. This is a statics problem, as all members are in equilibrium. The simplest approach to compute the suspension forces is to do it graphically.

It is first observed that the force acting on the upper arm F_{ua} can only be along axis, as the arm is pin-jointed on both ends. This allows to compute the intersection point G of the force F_Z and the upper link axis. By equilibrium, the direction of the force acting on the lower joint F_B is known as it must pass through the intersection point G. With that, the forces acting on the wheel and kingpin assembly can be computed using a force diagram illustrated in Fig. 3.14.

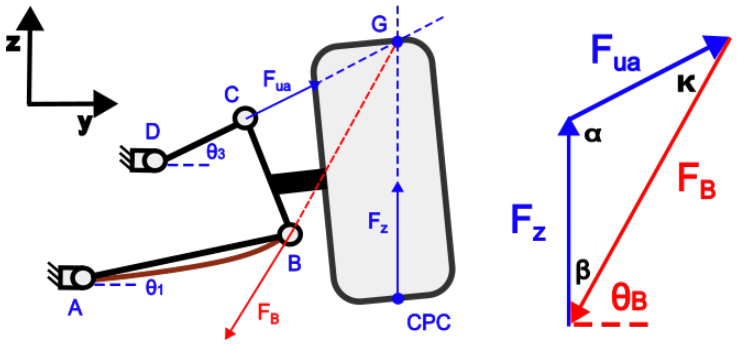

Figure 3.14: Free body diagram and force diagram of the wheel and kingpin assembly.

Analogous to the upper arm, the force acting on the lower arm must also be along its axis. By equilibrium, the force acting on the leaf spring F_S can be computed using the force diagram as illustrated in Fig. 3.15

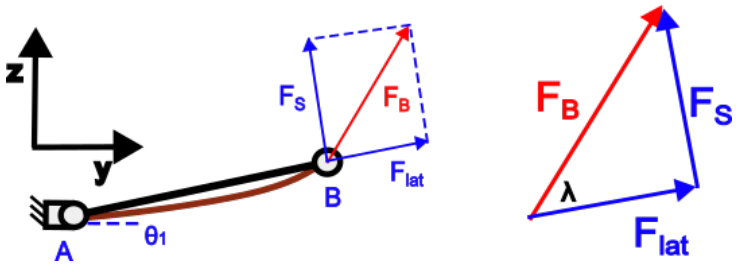

Figure 3.15: Free body diagram and force diagram of the lower arm and leaf spring assembly.

The vertical force $F_{S,vert}$ and lateral force $F_{S,vert}$ acting on the leaf can then be computed as illustrated in Fig. 3.16.

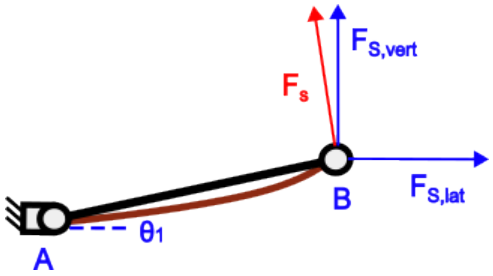

Figure 3.16: Free body diagram of the leaf.

For the computations, the leaf is assumed to be deforming under pure bending. Therefore, the lateral force $F_{S,vert}$ will be neglected. This assumption is further motivated by the fact that the angle θ_1 is really small (maximum 22° for this geometry) leading to a small $F_{S,vert}$. Another consideration is the effect of the lower arm on the deflected configuration of the leaf spring. As the arm is rigid, its rotation will cause the leaf to experience tension/compression hence, producing a supplementary lateral force on the arm. This force will also be neglected in the computation of the stresses.

Assuming the leaf spring rate in pure bending K and the current configuration of the suspension are known (this is the case when computing the force at the wheel during full jounce and rebound), F_Z can be computed by first computing F_S. Starting from the force diagram on the lower arm and on the leaf, F_B is computed

$$F_{S,vert} = F_S \sin(\frac{\pi}{2} + \theta_1) = F_B \sin(\lambda) \sin(\frac{\pi}{2} + \theta_1) \tag{3.44}$$

$$\iff F_B = \frac{F_S}{\sin(\lambda) \sin(\frac{\pi}{2} + \theta_1)} = \frac{K \Delta z_B}{\sin(\theta_B - \theta_1) \sin(\frac{\pi}{2} + \theta_1)}, \tag{3.45}$$

where Δz_B is the vertical displacement of pin joint B, θ_B is the angle of force B with respect to the y-axis and θ_1 is the angle of the lower link with respect to the y-axis. From there, the force diagram of the wheel and kingpin assembly gives the value of the static

wheel force. By the rule of sinuses one gets

$$\frac{F_Z}{\sin(\kappa)} = \frac{F_B}{\sin(\alpha)} \Longleftrightarrow F_Z = F_B \frac{\sin(\kappa)}{\sin(\alpha)}, \tag{3.46}$$

where α is the angle between F_{ua} and the z-axis and κ is the angle between F_{ua} and F_B. Using the geometry of the suspension and the properties of the triangle forces by the forces, it yields

$$\begin{cases} \alpha = \frac{\pi}{2} + \theta_3 \\ \beta = \frac{\pi}{2} - \theta_B \end{cases} \Rightarrow \kappa = \pi - \alpha - \beta = \theta_B - \theta_3 \tag{3.47}$$

where θ_3 is the angle of the upper arm. With configuration of the suspension, θ_B is computed. The position of point G is given by

$$\begin{cases} y_G = y_{CPC} \\ z_G = m_{ua} y_G + p_{ua} \end{cases} \tag{3.48}$$

where m_{ua} is the gradient and p_{ua} is the offset of the linear equation including the upper arm. The gradient writes

$$m_{ua} = \frac{z_C - z_D}{y_C - y_D}, \tag{3.49}$$

whilst the offset is found using the position of the upper hinge D

$$p_{ua} = z_D - m_{ua} y_D = z_D - \frac{z_C - z_D}{y_C - y_D} y_D. \tag{3.50}$$

The angle θ_B is then computed using the gradient m_B of the segment $\overline{BG}$

$$m_B = \frac{z_B - z_G}{y_B - y_G} \Rightarrow \theta_B = \tan^{-1}\left(\frac{z_B - z_G}{y_B - y_G}\right). \tag{3.51}$$

Expressed with the known quantities, the static force in the contact patch center F_Z finally writes

$$F_Z = \frac{K \Delta z_B}{\sin\left(\tan^{-1}\left(\frac{z_B - z_G}{y_B - y_G}\right) - \theta_1\right) \sin\left(\frac{\pi}{2} + \theta_1\right)} \frac{\sin\left(\tan^{-1}\left(\frac{z_B - z_G}{y_B - y_G}\right) - \theta_3\right)}{\sin\left(\frac{\pi}{2} + \theta_3\right)}. \tag{3.52}$$

In the case F_Z is imposed, Eq. (3.52) is still valid but the configuration corresponding to the equilibrium of the suspension has to be found iteratively, as the resulting suspension configuration is unknown.

When the lower arm is suppressed, the computation of the vertical load is similar except that the lower arm does not handle the later force F_{lat} anymore. The force applied on joint B F_B will therefore lead to a vertical force $F_{S,vert}$ and a lateral force $F_{S,lat}$ acting

directly on the leaf spring. The new force diagram is illustrated in Fig. 3.17.

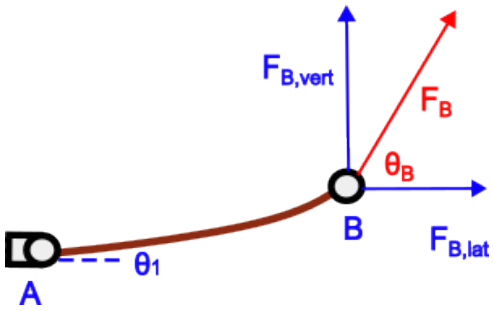

Figure 3.17: Free body diagram of the leaf in the case the lower arm is suppressed.

Now, the lateral force $F_{B,lat}$ applied on joint B has to be applied on the leaf. This means that the position of pin joint B is subjected to a change in position as the leaf is subjected to axial tension/compression. This is a problem in the computation as it would be necessary to use the principle of superposition to compute the displacement, which is strongly discouraged in the case of laminates [31]. For materials such as steel, empirical tables that provide a coefficient for the combine axial and transverse loads do exist but the same could not be found for composite beams. To avoid this potential problem, the leaf is considered rigid in its axial direction which leads to the same results as if the lower arm was still present. This assumption may rather well be best suited in this particular case as the leaf will most certainly be made of unidirectional plies in the y-axis of the suspension (x-axis in the ply coordinate system), leading to a very high Young modulus of 50GPa compared to a relatively small force of approximately 3500N maximum. Nonetheless, this assumption will be verified afterwards and the lateral force will be computed and considered for the stress analysis. Based on the forces in Fig. 3.17, force on the joint F_B now writes

$$F_B = \frac{F_{S,vert}}{\sin(\theta_B)} = \frac{K\Delta z_B}{\sin(\theta_B)} = \frac{K\Delta z_B}{\sin(\tan^{-1}(\frac{z_B - z_G}{y_B - y_G}))}, \tag{3.53}$$

and Eq. (3.52) becomes

$$F_Z = \frac{K\Delta z_B}{\sin(\tan^{-1}(\frac{z_B - z_G}{y_B - y_G}))} \frac{\sin(\tan^{-1}(\frac{z_B - z_G}{y_B - y_G}) - \theta_3)}{\sin(\frac{\pi}{2} + \theta_3)}. \tag{3.54}$$

3.3.1.3 Lateral loading

Adding a lateral load F_Y to the vertical load F_Z in the contact patch gives rise to a resultant wheel force F_R. The method to compute this force is the same as for the vertical load except that the position of the intersection point G is changed. The new associated free body diagram is illustrated in Fig. 3.18.

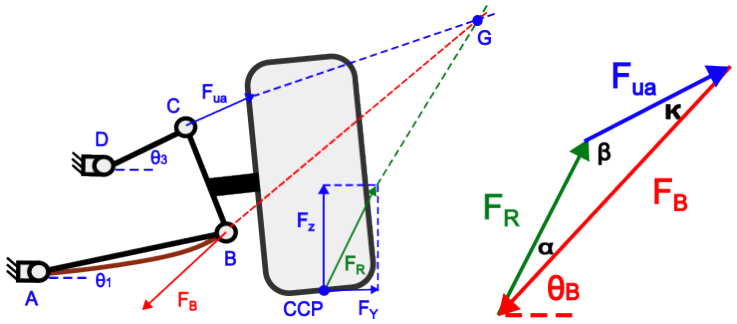

Figure 3.18: Free body diagram and force diagram of the wheel and kingpin assembly.

In this case, it is assumed that forces F_Z and F_Y are known and the configuration of the suspension is unknown. Analogously to the vertical load case, the rule of sinuses writes

$$\frac{F_R}{\sin(\kappa)} = \frac{F_B}{\sin(\beta)} \Longleftrightarrow F_Z = F_B \frac{\sin(\kappa)}{\sin(\beta)}, \tag{3.55}$$

Using the geometry of the suspension and the properties of the triangle forces by the forces, it yields

$$\begin{cases} \theta_R = \tan^{-1}(\frac{F_Z}{F_Y}) \\ \alpha = \theta_R - \theta_B \\ \beta = \pi - \theta_R + \theta_3 \end{cases} \Rightarrow \kappa = \pi - \alpha - \beta = \theta_B - \theta_3 \tag{3.56}$$

with θ_R the angle of the resulting force F_R. The position of point G is given by

$$z_G = m_{ua} y_G + p_{ua} = m_R y_G + p_R \Rightarrow y_G = \frac{p_R - p_{ua}}{m_{ua} - m_R} \tag{3.57}$$

with $m_R = tan(\theta_R)$ is the gradient of the force F_R and p_R is the offset. m_{ua} and p_{ua} are the same as for the vertical load. The offset p_R is computed using the center of the contact patch

$$z_{CPC} = m_R y_{CPC} + p_R \Rightarrow p_R = z_{CPC} - tan(\theta_R) y_{CPC}. \tag{3.58}$$

With all quantities known, the resultant force in the case the lower arm is present finally writes

$$F_R = \frac{F_{S,vert}}{\sin(\tan^{-1}(\frac{z_B - z_G}{y_B - y_G}) - \theta_1)\ \sin(\frac{\pi}{2} + \theta_1)} \frac{\sin(\tan^{-1}(\frac{z_B - z_G}{y_B - y_G}) - \theta_3)}{\sin(\tan^{-1}(\frac{F_Z}{F_Y}) - \theta_3)}, \tag{3.59}$$

and in the case the lower arm is suppressed writes

$$F_R = \frac{F_{B,vert}}{\sin(\tan^{-1}(\frac{z_B - z_G}{y_B - y_G}))} \frac{\sin(\tan^{-1}(\frac{z_B - z_G}{y_B - y_G}) - \theta_3)}{\sin(\tan^{-1}(\frac{F_Z}{F_Y}) - \theta_3)}. \tag{3.60}$$

Eq. (3.59) and Eq. (3.60) can be solved iteratively to find the suspension configuration corresponding to the given resultant force F_R.

3.3.1.4 Bump stops

In practice, suspension travel is limited by rubber elements called the bump stops. As contact is made with the upper arm of the suspension, the bump stop produces a rapidly increasing stiffness with deflection, which prevents contact between the suspension and the car body. There are two design approaches for the bump stop. The more conventional design is to have a relatively short and stiff bump stop. This design is targeted for infrequent contact with the upper arm, only in the case of extreme events (such as worst case accelerations for the suspension in Table 3.2). The other approach is to have a long and compliant bump stop, designed to come into contact with the upper arm often. The bump stop therefore acts as a secondary spring for large jounce. These kinds of bump stops can be found in all-terrain vehicles.

In this case, no information was found on whether the type or the position of the bump stop. It is therefore assumed that the bump stop position of the suspension corresponds to the maximum jounce position $\Delta z_{CPC} = 70$ and that the bump stop application point on the upper arm is the center of the upper arm. The suspension configuration at bump stop is represented in Fig. 3.19

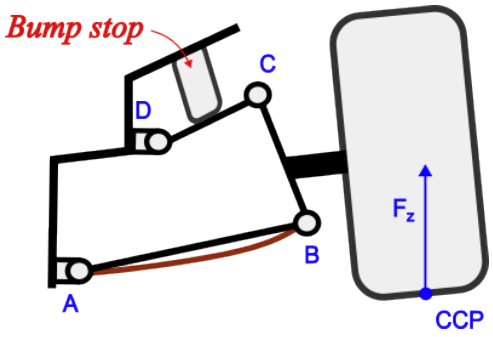

Figure 3.19: Suspension diagram in the case jounce is limited by a bump stop.

In the bump stop position, the wheel load F_z is greater than the vertical wheel load induced by the spring $F_{z'}$ As the upper arm is in contact with the bump stop, it is assumed that the bump stop and the suspension arms carry the excess of vertical wheel force $F_{ex} = F_z - F_{z'}$.

The computation of the suspension forces is separated in two steps. First, the suspension is drawn in the bump stop configuration (here equivalent to maximum jounce) considering the bump stop force is 0. Therefore, its associated wheel load $F_{z'}$ is computed with the same methodology as in Section 3.3.1.2. In a second step, the spring force is ignored and the bump stop force F_{bs} is considered while the wheel load F_{ex} is acting on the suspension. To compute the whole suspension forces, forces computed from the first

step are added to the one of the second step. The free body diagram of the suspension under the excess load F_{ex} is pictured in Fig. 3.20.

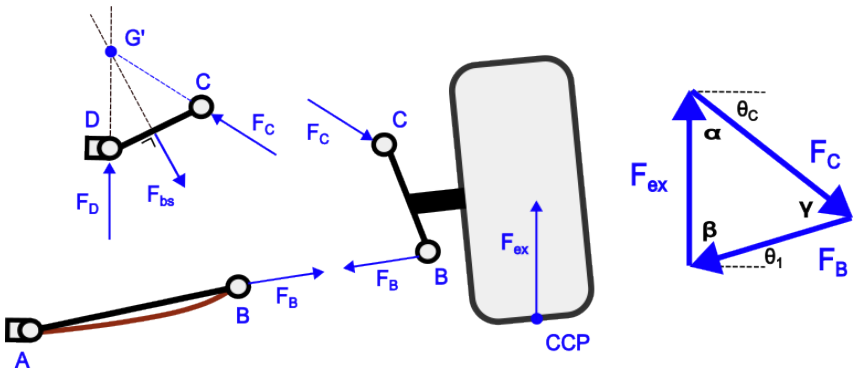

Figure 3.20: Free body diagram of the suspension in the bump stop case.

It is clear from the free body diagram that in the case a lower arm is present, the additional load F_{ex} does not add any load on the leaf. If the lower arm is deleted, the force F_B is acting directly on the leaf. As the arm is removed, the angle of application of F_B is now unknown. However, as the assumption was made that the leaf is rigid under axial tension/compression and that the knuckle is also rigid and rotates around the fixed joint C (due to the bump stop blocking the upper arm), the force F_B must therefore be purely axial. The new free body diagram associated to this case is pictured in Fig. 3.21.

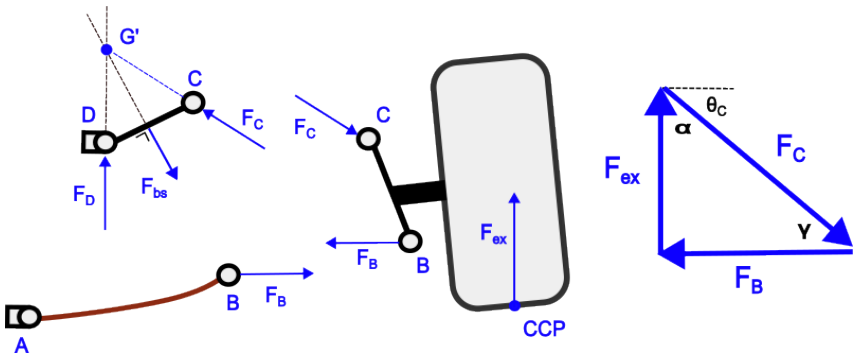

Figure 3.21: Free body diagram of the suspension without the lower arm in the bump stop case.

The force F_B yields

$$\frac{F_B}{\sin(\alpha)} = \frac{F_{ex}}{\sin(\gamma)} \Rightarrow F_B = F_{ex}\frac{\sin(\alpha)}{\sin(\gamma)} = F_{ex}\frac{\sin(\frac{\pi}{2} - \theta_C)}{\sin(\theta_C)} \tag{3.61}$$

where θ_C is computed using the intersection point G' between the forces F_D and F_{bs},

$$\theta_C = \tan^{-1}\frac{z_{G'} - z_C}{y_{G'} - y_C}. \tag{3.62}$$

3.3.1.5 Dynamic loading

Dynamic loads acting on suspension are mostly of a transient nature, which makes it complex to model. For a preliminary design, they are often modeled as static loads using dynamic load factors. Typical worst case load factors for suspension design are given in Table 3.2.

Load cases	Worst case acceleration		
	Longitudinal	Transverse	Vertical
Front/rear pothole bump	3 g at the wheel affected	0	4 g at the wheel affected, 1 g at other wheels
Bump during cornering	0	0	3.5 g at wheel affected, 1 g at other wheels
Lateral kerb strike	0	4 g at front and rear wheels on side affected	1 g at all wheels
Panic braking	2 g at front wheels, 0.4 g at rear wheels	0	2 g at front wheels, 0.8 g at rear wheels

Table 3.2: Typical worst case accelerations for dynamic suspension loads [4].

3.3.2 2D kinematic model

To compute suspension forces, 2D models in the front and side views of the suspension are required. The 3D suspension geometry is projected into the yz- and xz-planes (respectively front and side views of the suspension), leading to the 2D suspension diagrams in Fig. 3.22. For the sake of convenience, the suspension has been centered with respect to the x-axis.

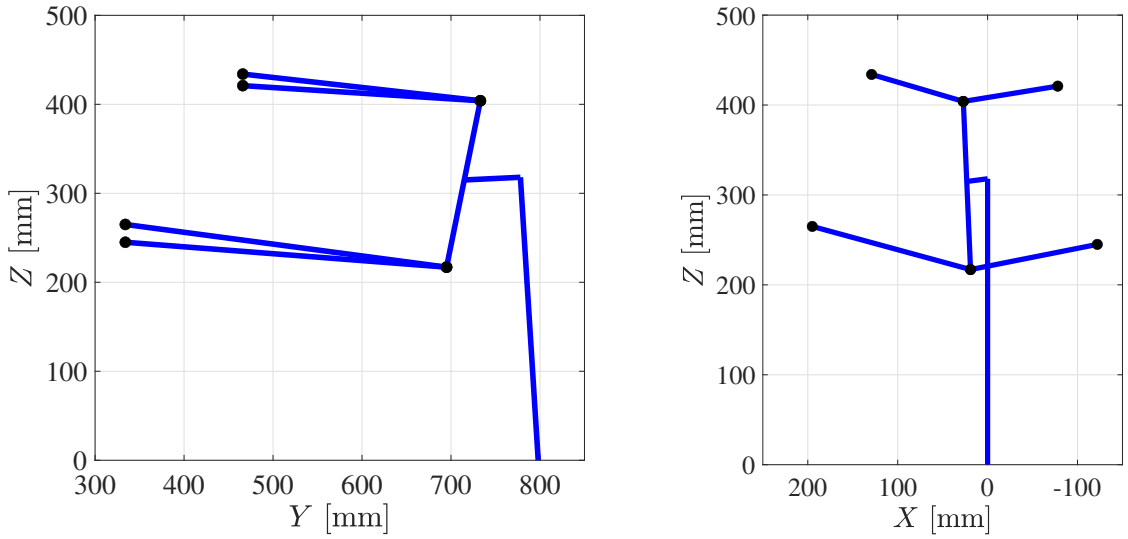

(a) Front view **(b)** Side view

Figure 3.22: Projected views of the 3D suspension geometry in the yz-plane (a) and xz-plane (b).

As it can be seen in Fig. 3.22a, the upper hinges and lower hinges are not aligned with each other, which should not be the case when analysing a double-wishbone suspension in 2D. In this case, the suspension is actually tiled by an angle $\zeta = -3.6°$ around the y-axis. The 2D side and front views are obtained by rotation of the 3D suspension geometry using Eq. (3.63).

$$\mathbf{A}' = \mathbf{A} * \mathbf{R}(\zeta) = \mathbf{A} \begin{pmatrix} \cos(\zeta) & 0 & \sin(\zeta) \\ 0 & 1 & 0 \\ -\sin(\zeta) & 0 & \cos(\zeta) \end{pmatrix}, \tag{3.63}$$

with **A** the matrix of coordinates of the 3D suspension and **A**' the new coordinates. Side and front views of the un-tilted suspension are pictured in Fig. 3.23

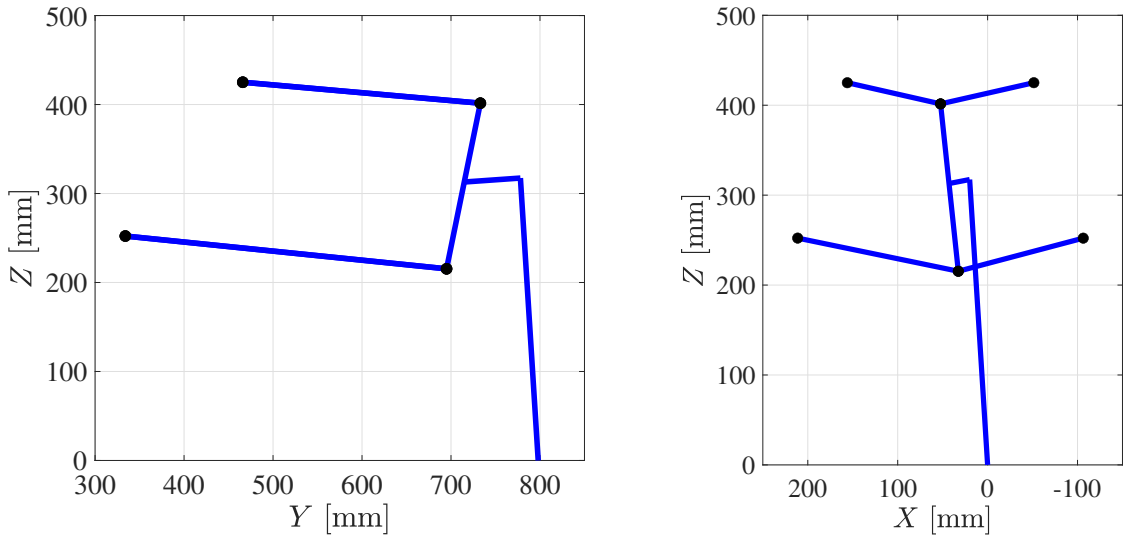

(a) Front view **(b)** Side view

Figure 3.23: Projected views of the un-tilted 3D suspension geometry in the yz-plane (a) and xz-plane (b).

A generic geometry of the front view Fig. 3.24a can be particularised to the current suspension based on the results obtained in Fig. 3.23a and the side view Fig. 3.24b is simplified to the requirements in the computation of the lateral force. Geometrical parameters of the schematics are gathered in Table 3.3.

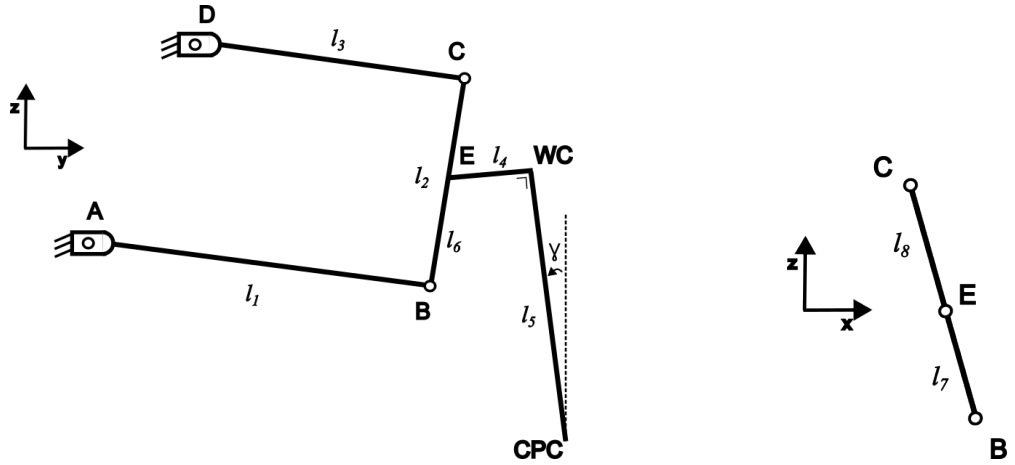

(a) Front view **(b)** Side view

Figure 3.24: Geometry of the 2D suspension model in the front (a) and side (b) view planes.

Parameter	Symbol	Value in standard position [mm]
Position of hinge A	(y_A, z_A)	(334, 252)
Position of revolute joint B	(x_B, y_B, z_B)	(32.6, 695, 216)
Position of revolute joint C	(x_C, y_C, z_C)	(52.3, 733, 401)
Position of hinge D	(y_D, z_D)	(466, 425)
Position of king-pin E	(x_E, y_E, z_E)	(42.7, 715, 313)
Position of wheel center WC	(y_{WC}, z_{WC})	(778, 317)
Position of center contact patch	(y_{CPC}, z_{CPC})	(797, 0)
Length long arm [AB]	l_1	363
Length knuckle arm [BC]	l_2	189
Length short arm [CD]	l_3	268
Length king-pin axle [EWC]	l_4	63
Radius of the wheel [WCCPC]	l_5	318
Length link [BE] (front plane)	l_6	99
Length link [BE] (side plane)	l_7	98
Length link [CE]	l_8	88

Table 3.3: Parameters for the 2D suspension schematics in the standard driving position.

Kinematics of this 2D suspension model are investigated to define the suspension configuration along the wheel vertical displacement. The planar mechanical system of the suspension is the one of the well-known four bar mechanism [40], as bars l_2, l_4 and l_5 can be assumed as a single body since it is a rigid assembly. The fourth bar virtually linking points A and D is a higher pair and is therefore not considered. The degrees of freedom

(DOFs) of the mechanisms are obtained using Grübler's formula, which in 2D yields

$$F = 3N - \sum_{i=1}^{n_j} p_i, \tag{3.64}$$

where F is the number of DOFs, N the number of bodies, n_j the number of joints and p_i the number of DOFs suppressed by joint number i. In this case, there are four bodies and four joints that are all revolute joints which each suppresses two DOFs. Eq. (3.64) becomes

$$F = 3 \cdot 3 - \sum_{i=1}^{4} 2 = 9 - 8 = 1, \tag{3.65}$$

which means that the mechanism can be described with only one coordinate, hence, the vertical displacement of the wheel.

To derive the equations of motion, the free body diagram (FBD) of the mechanism is created based on finite element coordinates.

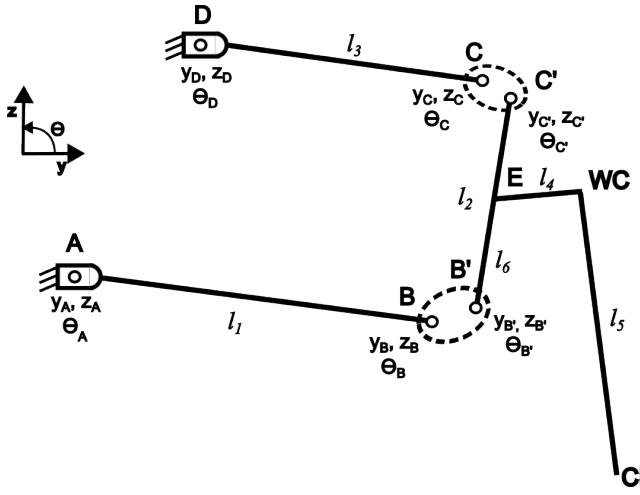

Figure 3.25: Free body diagram of the 2D suspension model in the front view.

Based on Fig. 3.25, there are 6 nodes leading to a total of 18 DOFs and therefore as many active coordinates. Rigidity constraints, assembly constraints and boundary conditions are expressed to reduce the size of the set of active coordinates.

1. Assembly constraints:

$$\begin{cases} y_B = y_{B'} \\ z_B = z_{B'} \end{cases} \quad (3.66) \qquad \begin{cases} y_C = y_{C'} \\ z_C = z_{C'} \end{cases} \quad (3.67)$$

2. Rigidity constraints:

$$\theta_A = \theta_B = \theta_1 \quad (3.68) \qquad \theta_{B'} = \theta_{C'} = \theta_2 \quad (3.69) \qquad \theta_C = \theta_D = \theta_3 \quad (3.70)$$

3. Boundary conditions:

$$\begin{cases} y_A = 334mm \\ z_A = 252mm \end{cases} \quad (3.71) \qquad \begin{cases} y_D = 466mm \\ z_D = 425mm \end{cases} \quad (3.72)$$

With the defined constraints, rigidity conditions for each links are expressed:

$$1^{\text{st}} \text{ link:} \quad \begin{cases} y_B = y_A + l_1\cos(\theta_1) \\ z_B = z_A + l_1\sin(\theta_1) \end{cases} \quad (3.73)$$

$$2^{\text{nd}} \text{ link:} \quad \begin{cases} y_C = y_B + l_2\cos(\theta_2) \\ z_C = z_B + l_2\sin(\theta_2) \end{cases} \quad (3.74)$$

$$3^{\text{rd}} \text{ link:} \quad \begin{cases} y_C = y_D + l_3\cos(\theta_3) \\ z_C = z_D + l_3\sin(\theta_3) \end{cases} \quad (3.75)$$

Injecting Eq. (3.73) into Eq. (3.74), it yields

$$\begin{cases} y_C = y_A + l_1\cos(\theta_1) + l_2\cos(\theta_2) \\ z_C = z_A + l_1\sin(\theta_1) + l_2\sin(\theta_2) \end{cases} \quad (3.76)$$

Injecting Eq. (3.76) into Eq. (3.75), the equations of motion are obtained:

$$\begin{cases} y_A + l_1\cos(\theta_1) + l_2\cos(\theta_2) = y_D + l_3\cos(\theta_3) \\ z_A + l_1\sin(\theta_1) + l_2\sin(\theta_2) = z_D + l_3\sin(\theta_3) \end{cases} \quad (3.77)$$

As expected from Grubler's formula, the kinematics of the suspension are described in a system of two equations for a total of three unknowns θ_1, θ_2 and θ_3 hence, one single DOF. However, it is not convenient to describe the motion of the suspension as a function of θ rather than the vertical displacement of the wheel. Therefore, the angle θ_2 is expressed as a function of the vertical displacement of the wheel z_{CPC} using the geometry of the king-pin axles and wheel assembly.

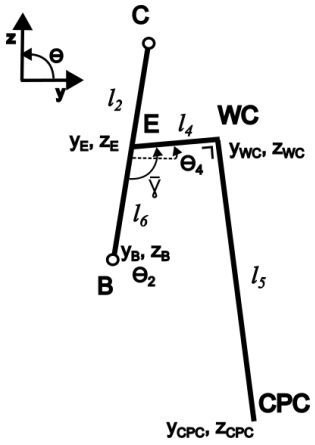

Figure 3.26: Geometry of the king-pin axle and wheel assembly.

Based on Fig. 3.26, constraints are derived for the king-pin axle and wheel assembly. First, the constraints on the links

$$4^{\text{th}} \text{ link:} \quad \begin{cases} y_{WC} = y_E + l_4 \cos(\theta_4) \\ z_{WC} = z_E + l_4 \sin(\theta_4) \end{cases} \tag{3.78}$$

$$5^{\text{th}} \text{ link:} \quad \begin{cases} y_{CPC} = y_{WC} + l_5 \cos(\theta_5) \\ z_{CPC} = z_{WC} + l_5 \sin(\theta_5) \end{cases} \tag{3.79}$$

$$6^{\text{th}} \text{ link:} \quad \begin{cases} y_E = y_B + l_6 \cos(\theta_2) \\ z_E = z_B + l_6 \sin(\theta_2) \end{cases} \tag{3.80}$$

Merging Eq. (3.78), Eq. (3.79), Eq. (3.80) and Eq. (3.73)

$$\begin{cases} y_{CPC} = y_A + l_1 \cos(\theta_1) + l_4 \cos(\theta_4) + l_5 \cos(\theta_5) + l_6 \cos(\theta_2) \\ z_{CPC} = z_A + l_1 \sin(\theta_1) + l_4 \sin(\theta_4) + l_5 \sin(\theta_5) + l_6 \sin(\theta_2) \end{cases} \tag{3.81}$$

Due to the rigidity of the king-pin axle and wheel assembly, angles γ and θ_5 can be expressed using θ_2

$$\begin{cases} \theta_4 = -\gamma = \bar{\gamma} - \pi + \theta_2 \\ \theta_5 = \theta_4 - \frac{\pi}{2} = \bar{\gamma} - \pi + \theta_2 - \frac{\pi}{2} = \bar{\gamma} + \theta_2 - \frac{3\pi}{2} \end{cases} \tag{3.82}$$

where $\bar{\gamma}$ is the constant angle formed by link 4 and link 6. Using the initial configuration of the suspension, $\bar{\gamma}$ is computed:

$$\bar{\gamma} = \gamma + \pi - \theta_2 = 0.06 + \pi - 1.37 = 1.83\text{rad} \tag{3.83}$$

Injecting Eq. (3.82) in Eq. (3.81)

$$\begin{cases} y_{CPC} = y_A + l_1\cos(\theta_1) + l_4\cos(\bar{\gamma} - \pi + \theta_2) + l_5\cos(\bar{\gamma} + \theta_2 - \dfrac{3\pi}{2}) + l_6\cos(\theta_2) & \text{(3.84a)} \\ z_{CPC} = z_A + l_1\sin(\theta_1) + l_4\sin(\bar{\gamma} - \pi + \theta_2) + l_5\sin(\bar{\gamma} + \theta_2 - \dfrac{3\pi}{2}) + l_6\sin(\theta_2) & \text{(3.84b)} \end{cases}$$

As z_{CPC} is the preferred active coordinate of the system, its expression Eq. (3.84b) is added to the set of motion equations Eq. (3.77).

$$\begin{cases} y_A + l_1\cos(\theta_1) + l_2\cos(\theta_2) = y_D + l_3\cos(\theta_3) & \text{(3.85a)} \\ z_A + l_1\sin(\theta_1) + l_2\sin(\theta_2) = z_D + l_3\sin(\theta_3) & \text{(3.85b)} \\ z_{CPC} = z_A + l_1\sin(\theta_1) + l_4\sin(\bar{\gamma} - \pi + \theta_2) + l_5\sin(\bar{\gamma} + \theta_2 - \dfrac{3\pi}{2}) + l_6\sin(\theta_2) & \text{(3.85c)} \end{cases}$$

Leading to a new system with three equations and four unknowns, where the DOF is defined as z_{CPC}. Imposing the vertical displacement at the wheel z_{CPC}, Eq. (3.85) could be rewritten as a single equation of motion depending only on the angle θ_2. However, this leads to a very non-linear equation. Instead, the system is solved on MATLAB using the *fsolve()* function [41] which, by default, utilises a trust-region dogleg algorithm based on Powell's dogleg method [42]. The configuration of the suspension along the vertical wheel displacement is therefore computed by solving the system of equations Eq. (3.85). For the maximum rebound and jounce position, the configurations are pictured in Fig. 3.27.

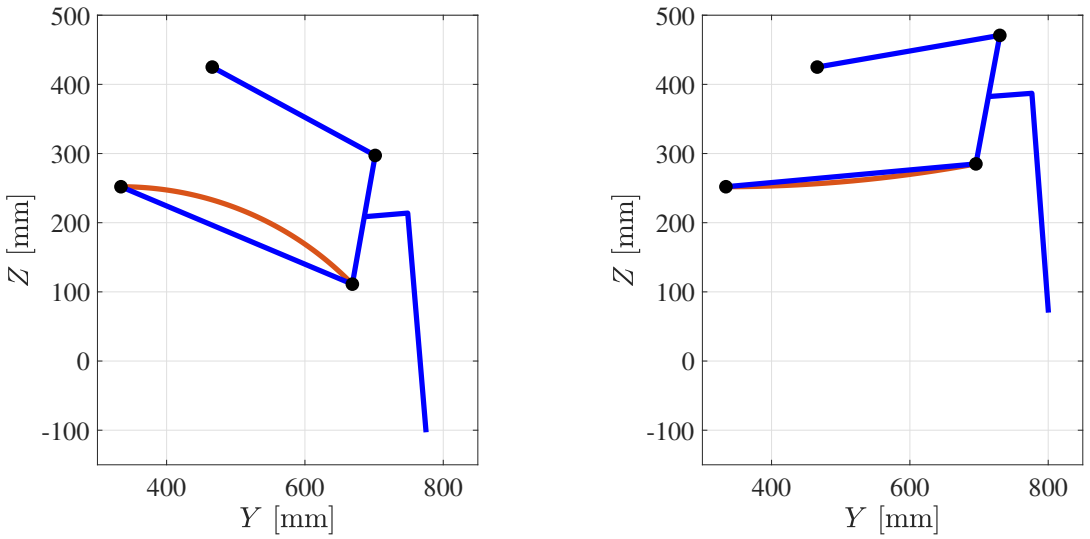

Figure 3.27: Computed configurations of the suspension in the minimum rebound (a) and maximum jounce (b) positions using MATLAB (integration degrees 1 and 2a, leaf in orange).

In the case the lower arm is suppressed, the rigid link AB is replaced by the leaf spring (beam in bending) in the kinematic model, as pictured in Fig. 3.28. The position of the lower joint B is now determined by the bending of the leaf only, which is now free since the arm is suppressed.

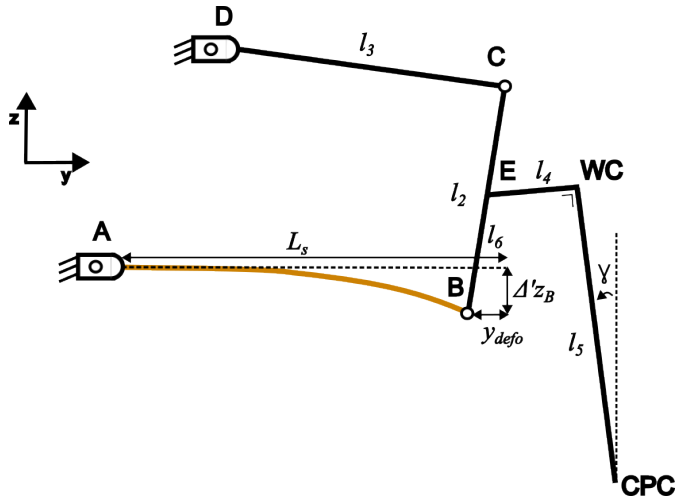

Figure 3.28: Free body diagram of the 2D suspension model in the front view in the case of a suppressed lower arm.

For the case where the leaf is represented using a cantilever beam (integration degree 2b), the position (y_B, z_B) can be expressed as the sole function of z_B rather than using θ_1 by using Eq. (3.29).

$$y_B = y_A + L\sqrt{\frac{sin(\frac{3\Delta z}{2L})}{\frac{3\Delta z}{2L}}} = L\sqrt{\frac{sin(\frac{3(z_B - z_A)}{2L})}{\frac{3(z_B - z_A)}{2L}}} \tag{3.86}$$

Eq. (3.86) can be now inserted in the equations of motion, replacing the unknown θ_1 by the unknown z_B.

$$\begin{cases} y_A + L\sqrt{\dfrac{sin(\frac{3(z_B - z_A)}{2L})}{\frac{3(z_B - z_A)}{2L}}} + l_2\cos(\theta_2) = y_D + l_3\cos(\theta_3) & \text{(3.87a)} \\ z_B + l_2\sin(\theta_2) = z_D + l_3\sin(\theta_3) & \text{(3.87b)} \\ z_{CPC} = z_B + l_4\sin(\bar{\gamma} - \pi + \theta_2) + l_5\sin(\bar{\gamma} + \theta_2 - \dfrac{3\pi}{2}) + l_6\sin(\theta_2) & \text{(3.87c)} \end{cases}$$

The system of motion equations Eq. (3.87) is solved analogously to Eq. (3.85) using the *fsolve()* function of MATLAB. Computed position of maximum jounce and minimum rebound position are pictured in Fig. 3.29 to illustrate these results.

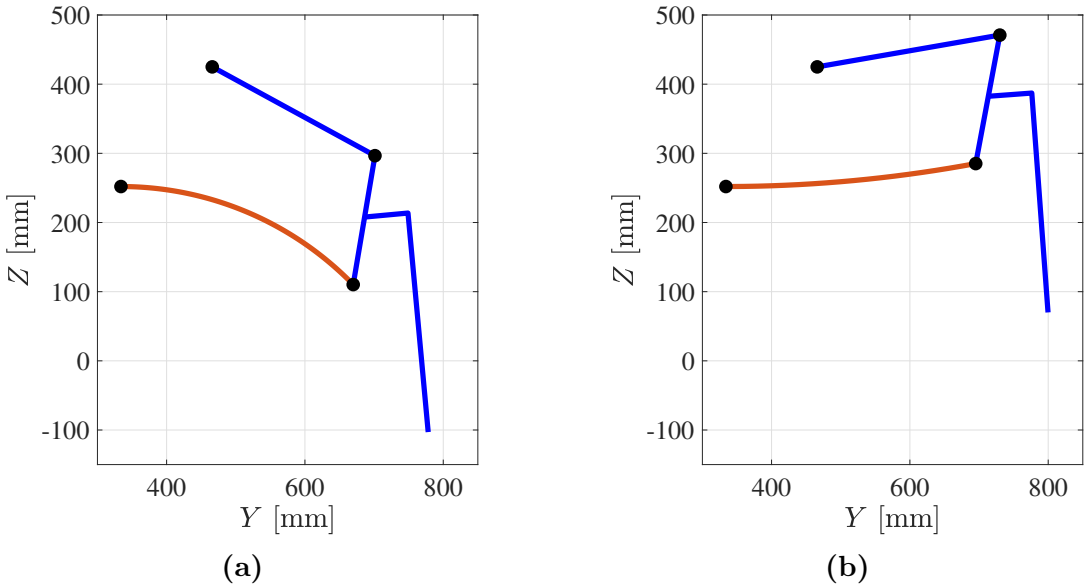

Figure 3.29: Computed configurations of the suspension in the minimum rebound (a) and maximum jounce (b) positions using MATLAB (integration degree 2b, leaf in orange).

As explained before, the case of the large deformation of the overhanging beam (integration degree 3) is not studied. The motion of joint B is therefore considered the same as if the arm was still imposing the motion.

Chapter 4

Preliminary leaf designs

With the established methodology in Chapter 3, a preliminary design is computed for each integration degree of the leaf spring proposed in Table 3.1 based on their diagrams illustrated in Fig. 3.2. The analysis is performed considering a simple leaf whose cross-section is fixed along the whole length. The width b of the leaf will be fixed to 100mm and the thickness will be constant. The laminate is also considered unidirectional in the direction of the vertical load. These parameters are discussed in a second step of the analysis (see Section 4.6). Therefore, equivalent structural properties are the same as the material properties: $E_x = E_{11}$, $E_y = E_{22}$ and $G_{xy} = G_{12}$. Preliminary designs are then compared and possible improvements are defined based on the obtained results.

4.1 Coil spring integration

The analytical methodology is first applied to the case where the leaf replaces the coil springs only, which is denoted integration degree 1 in Table 3.1.

4.1.1 Geometry of the leaf

For the computation of the vertical force in the contact patch, it is necessary to compute the leaf spring rate K. To least alter the characteristics of the car, the choice is made to keep the same standard ($1g$ load) and unloaded ($F_z = 0N$, not the minimum rebound position due to the mass of the wheel) positions of the suspension. Based on Fig. 1.7, the vertical displacement at the wheel contact patch corresponding to a 0N load yields $\Delta z_{CPC} = -99$mm. For this configuration, the position of the lower joint is computed solving the equations of motions Eq. (3.85) and writes $z_b = 115$mm. Finally the vertical displacement of the lower joint Δz_B is

$$\Delta z_B = z_B(F = 2859\text{N}) - z_B(F = 0\text{N}) = 216 - 115 = 101\text{mm}. \tag{4.1}$$

With this result and with the assumption that the leaf is deformed under pure bending, the spring rate of the leaf is computed based on Eq. (3.52). It yields

$$K = \frac{F_Z}{\Delta z_B} \frac{\sin(\tan^{-1}(\frac{z_B - z_G}{y_B - y_G}) - \theta_1)\, \sin(\frac{\pi}{2} + \theta_1)\, \sin(\frac{\pi}{2} + \theta_3)}{\sin(\tan^{-1}(\frac{z_B - z_G}{y_B - y_G}) - \theta_3)} \tag{4.2}$$

which is solved using the standard position of the suspension, leading to $K = 28.2\text{N/mm}$.

With the spring rate K, the cross section can be computed using the classical straight beam theory applied to the cantilever beam, as formulated in Eq. (3.16). Therefore, the spring rates writes

$$K = \frac{F}{\Delta z} = \frac{3E_x I}{L^3} \tag{4.3}$$

For a rectangular cross section, the second moment of inertia I writes

$$I = \frac{bt^3}{12}, \tag{4.4}$$

where $b = 100\text{mm}$ is the width and t is the thickness. Inserting Eq. (4.4) in Eq. (4.3), the thickness of the leaf spring yields

$$t = \sqrt[3]{\frac{12L^3K}{3E_x b}} = \sqrt[3]{\frac{12 \cdot 363^3 \cdot 28.2}{3 \cdot 39 \cdot 10^3 \cdot 100}} = 11\text{mm} \tag{4.5}$$

With the curvature already computed in Section 3.2.2.1, the complete geometry of the unloaded leaf is known and pictured in Fig. 4.1.

(a) 2D Geometry **(b)** Cross section

Figure 4.1: Initial 2D geometry of the leaf spring for integration degree 1 (a) and its cross section (b).

For this leaf design, the total mass of the leaf can be computed knowing that the curved parts of the leaf have an angular span $\theta = 46°$:

$$M = bt(2R\theta + l)\rho = 100 \cdot 11 \cdot (2 \cdot 468 \cdot \frac{41 \cdot \pi}{180} + 668) \cdot \frac{2000}{10^9} = 2.89\text{kg}, \tag{4.6}$$

with l the length between the curved parts (*i.e.* between the position of mount supports). This total mass is almost half the mass of the original coil springs (2.7kg each [43]).

To verify that the Euler-Bernoulli beam theory is valid (*i.e.* the shear deformation

can be neglected), the criterion expressed in Eq. (3.33) is verified.

$$\frac{3EI}{\kappa' L^2 AG} = \frac{3E_x bt^3}{12\kappa' L^2 btG_{xy}} = \frac{3 \cdot 39 \cdot 100 \cdot 11^3}{12 \cdot 5/6 \cdot 363^2 \cdot 100 \cdot 11 \cdot 3.7} = 0.003 << 1. \tag{4.7}$$

The criterion is therefore valid, meaning that the computation can be carried out with the standard beam theory.

4.1.1.1 Modal analysis

As the road presents irregularities, the suspension will experience vibrations that usually have a maximum frequency of 12Hz [29]. It is therefore necessary to check that the first natural frequency of the leaf is superior to this value in the case of standard driving conditions. For a cantilever beam, natural frequencies f_n can be approximated using the empirical relation in Eq. (4.8).

$$f_n = \frac{\alpha_n^2}{2\pi}\sqrt{\frac{EI}{\rho A L^4}} = \frac{\alpha_n t}{2\pi L^2}\sqrt{\frac{E_x}{12\rho}} \tag{4.8}$$

where A is the cross section of the beam and α_n is an empirical coefficient. First three frequencies and associated values of the coefficient α_n [29] are given in Table 4.1 while the mode shapes are illustrated in Fig. 4.2.

n	Coefficient α_n	Natural frequency f_n
1	1.875	31.8Hz
2	4.694	79.5Hz
3	7.885	133.5Hz

Table 4.1: First three natural frequencies of the leaf spring for integration degree 1.

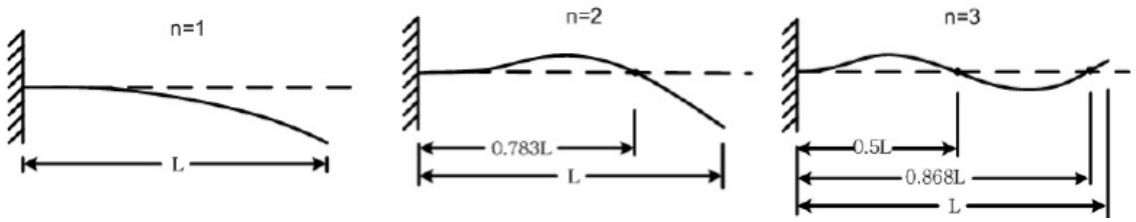

Figure 4.2: First three mode shapes for a cantilever beam [44].

Estimated natural frequencies are all greater than 12Hz, which should ensure that the leaf does not enter resonance due to the vibrations of the road.

4.1.2 Kinematic analysis

The transverse leaf spring suspension is studied over its jounce/rebound behavior, with no other loads applied. With the equations of motion Eq. (3.85), the different configuration of the suspension are computed over the whole vertical wheel travel. This allows to compute half-track and camber variation. These two results are compared with the results obtained from the original suspension in Fig. 4.3a and Fig. 4.3b.

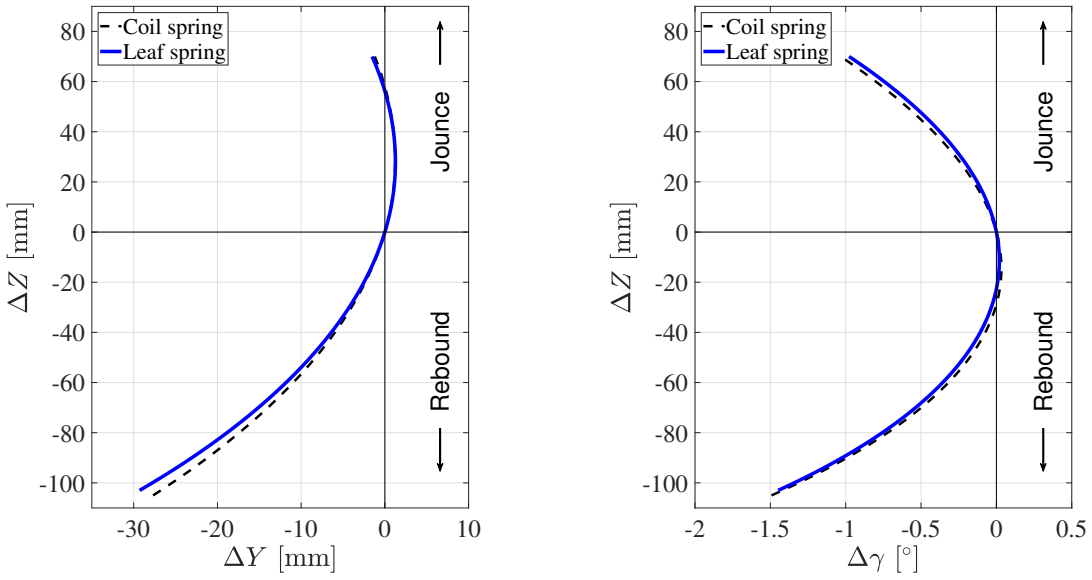

Figure 4.3: Half-track (a) and camber (b) variation during jounce and rebound for the leaf spring with integration degree 1, computed using the 2D MATLAB model and compared with the results from the original suspension.

As it can be seen in Fig. 4.3, variation of the half-track and camber angle from the 2D model are similar to the ones from the original suspension with coil springs. This was expected as, in this case, the leaf spring has no impact on the motion of the suspension which is modeled to be the same as the original. The small differences however can be imputed to the fact that the 3D suspension has been un-tilted by 3.6° to build the 2D model. This rotation did not change the value of the half-track distance but the initial camber angle is different. The negative camber angle in the 2D model is 3.3° while it was 2.5° for the initial suspension in 3D.

Using the suspension configurations with Eq. (3.52), the vertical wheel force is computed along the wheel travel. Results for the leaf spring are compared with the ones from the original suspension in Fig. 4.4.

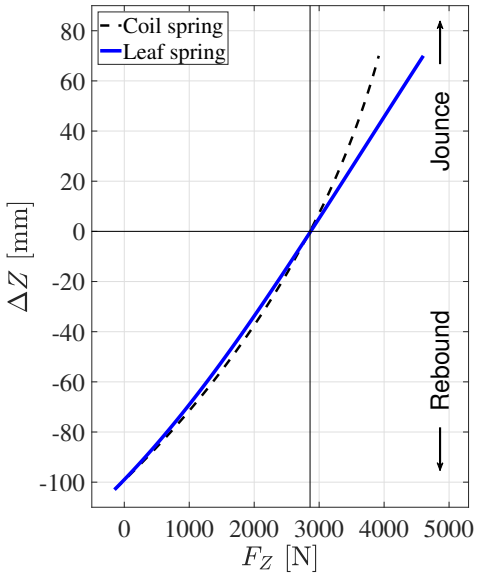

Figure 4.4: Vertical static loading in the contact patch center during jounce and rebound for the leaf spring integration degree 1, computed using the 2D MATLAB model and compared with the results from the original suspension.

The maximum force in the contact patch for this design is 4603N in jounce while the minimum force is -151N in rebound (due to the mass of the wheel). As it can be observed in Fig. 4.4, the vertical force in the contact patch F_Z is much more linear along the wheel stroke compared to the original design.

To compute stresses along the leaf, the bending force acting on the leaf is computed along the wheel stroke (Fig. 4.5a). As the laminate is considered unidirectional, the maximum bending stress σ_{max} can be computed using the classical beam theory. The bending stress occurring at the vertical position z from the neutral axis writes

$$\sigma(y) = \frac{z}{2}\frac{M(y)}{I} = \frac{z}{2}\frac{12F(L-y)}{bt^3}, \tag{4.9}$$

where $M(y)$ is the moment along the beam's axis. The maximum stress is found at the extreme fibers of the leaf at the clamped support. Eq. (4.9) is particularised to find the maximum bending stress and writes

$$\sigma_{max} = \frac{t}{2}\frac{12FL}{bt^3}. \tag{4.10}$$

The maximum bending stress along the wheel stroke is pictured in Fig. 4.5b.

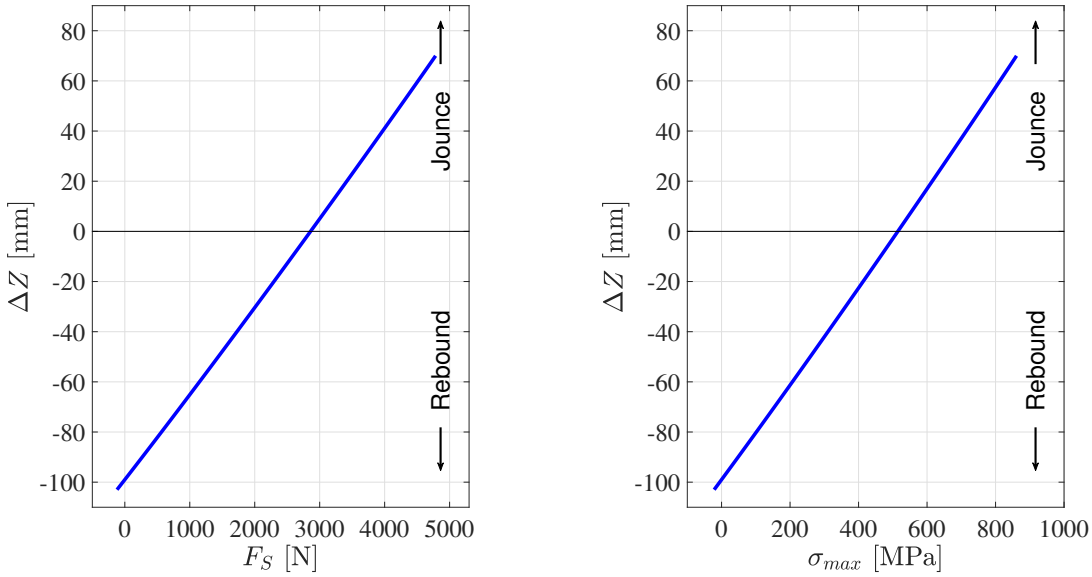

Figure 4.5: Vertical static loading acting on the leaf (a) and maximum bending stress (b) during jounce and rebound for the leaf spring with integration degree 1, computed using the 2D model MATLAB.

As it can be seen in Fig. 4.5b, the maximum bending stress occurs at full jounce and is 861MPa. To verify if failure occurs, Tsaï-Wu criterion Eq. (3.38) is computed for the maximum bending stress:

$$\begin{aligned} F_1\sigma_1 + F_{11}\sigma_1^2 &= \left(\frac{1}{\sigma_1^T} - \frac{1}{\sigma_1^C}\right)\sigma_x + \frac{\sigma_x^2}{\sigma_1^T\sigma_1^C} \\ &= \left(\frac{1}{1082} - \frac{1}{620}\right)861 + \frac{861^2}{1082 \cdot 620} = 0.51 < 1. \end{aligned} \tag{4.11}$$

The failure criterion is therefore satisfied, which means that the design is safe. The associated safety factor yields $R = 1.26$.

For the maximum jounce position of the suspension, the stresses along the beam are computed using Eq. (4.9). Results are pictured in Fig. 4.6

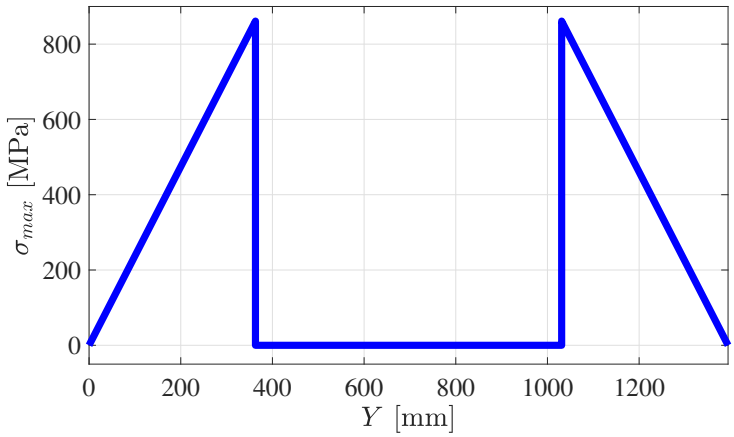

Figure 4.6: Maximum bending stress along the leaf spring in the case of maximum jounce of the suspension.

4.1.3 Dynamic loading

As mentioned in Section 3.3.1.5, worst case loads are assessed using a static load with dynamic load factors present in Table 3.2. For this suspension design, most typical worst case scenarios are trivial or have no impact on the leaf.

For the rear pothole bump, longitudinal loading is ignored since the arms are considered rigid. Also, due to the leaf being clamped, the rear axle is fully independent. This means that a different load acting on one of the wheels will have no impact on the other wheel. The 4g load acting on one of the wheels will simply correspond to the bump stop position, which gives a vertical force due to the leaf spring $F_{Z'} = 4603$. The excess force F_{ex} is computed and yields

$$F_{ex} = F_Z - F_{Z'} = 4 * 2859 - 4603 = 6833\text{N}. \tag{4.12}$$

This excess force is entirely taken by the lower arm and the bump stop, as demonstrated in Section 3.3.1.4. Finally, the configuration of the suspension is simply one of the wheel in the 1g position and the other one at full jounce, or in terms of vertical displacement of the wheel $z_{CPC} = 0$mm and $z_{CPC} = 70$mm respectively.

For the bump during cornering, the solution is the same as for the pothole bump. Position of the wheels are the same but the excess force is smaller

$$F_{ex} = F_Z - F_{Z'} = 3.5 * 2859 - 4603 = 5403\text{N}. \tag{4.13}$$

For panic braking, longitudinal loads are also ignored due to the rigid arms. The position of the wheels is directly found by looking at Fig. 4.4. A vertical force of 0.8g = 2287N corresponds to a vertical wheel displacement $z_{CPC} \approx -22.4$mm.

The only non-trivial worst case acceleration is the one of the lateral kerb strike, which is pictured in Fig. 4.7.

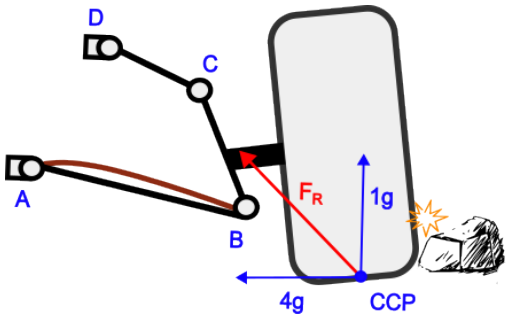

Figure 4.7: Loading case for the lateral kerb strike.

In this case, the position of the wheel is found by solving Eq. (3.59). To do so, the spring force $F_{S,vert}$ due to the kerb impact resulting force $F_R = \sqrt{2859^2 + (4 \cdot 2859)^2}$N is computed. Then, the position of the suspension corresponds to the one where $F_{S,vert} = K\Delta z_B$. In this case, the load applied on the spring is $F_{S,vert} = 1276$N, corresponding to a wheel displacement of -59.8mm. This means that, due to the lateral kerb strike, the wheel impacted experiences a rebound of approximately 60mm.

4.2 Coil spring and anti-roll bar integration

The analytical methodology is applied to the case where the leaf integrates the coil springs and anti-roll bar, which is denoted integration degree 2a in Table 3.1.

4.2.1 Leaf spring model

The leaf spring rate K is the same as for the coil spring integration, as the motion of the suspension is defined by the arms and not the leaf. With the value of the spring rate, cross section is computed using the classical straight beam theory applied to the overhanging beam, as formulated in Eq. (3.21).

$$K = \frac{F}{\Delta z} = \frac{6EI}{2c^3 + 3c^2 l} = \frac{E_x b t^3}{2(2c^3 + 3c^2 l)} \tag{4.14}$$

From there, thickness writes

$$t = \sqrt[3]{\frac{2K(2c^3 + 3c^2 l)}{E_x b}} = \sqrt[3]{\frac{2 \cdot 28.2 \cdot (2 \cdot 363^3 + 3 \cdot 363^2 \cdot 668)}{39 \cdot 10^3 \cdot 100}} = 17.3\text{mm}. \tag{4.15}$$

With the curvature already computed in Section 3.2.2.1, the complete geometry of the unloaded leaf is known and pictured in Fig. 4.8.

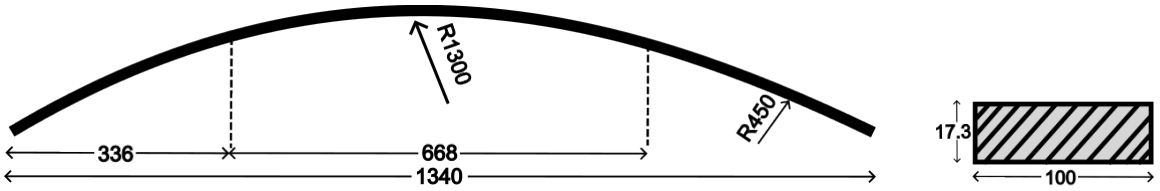

(a) 2D Geometry **(b)** Cross section

Figure 4.8: Initial 2D geometry of the leaf spring for integration degree 1 (a) and its cross section (b).

For this leaf design, the total mass of the leaf can be computed knowing that the curved parts of the leaf have an angular span of $2\theta = 2 * 31$:

$$M = R(2\theta)A\rho = 1300 \cdot 2 \cdot \frac{31 \cdot \pi}{180} \cdot 17.3 \cdot 100 \cdot \frac{2000}{10^9} = 4.87\text{kg}. \tag{4.16}$$

For the original suspension, the mass of the two springs is 5.6kg and the anti-roll bar can be estimated to have a mass of 1kg [45]. The integration of the leaf therefore represents a 27% mass saving on the rear axle (considering that an anti-roll bar is necessary).

To verify that the Euler-Bernoulli beam theory is valid (*i.e.* the shear deformation can be neglected), the criterion expressed in Eq. (3.33) is verified.

$$\frac{3EI}{\kappa' L^2 AG} = \frac{3E_x bt^3}{12\kappa' L^2 btG_{xy}} = \frac{3 \cdot 39 \cdot 100 \cdot 17.3^3}{12 \cdot 5/6 \cdot 363^2 \cdot 100 \cdot 17.3 \cdot 3.7} = 0.007 << 1. \tag{4.17}$$

The criterion is verified, meaning that the computation can be carried out with the standard beam theory.

4.2.2 Modal analysis

For the overhanging beam model subjected to loads on its free ends, no model estimating the first natural frequencies of the beam has been found. Therefore, modal analysis cannot be done analytically and will be performed based on the finite element model of the beam in Section 5.3.

4.2.3 Kinematic analysis

In this case, the suspension is modeled as for the previous case. Therefore, half-track variation (Fig. 4.3a), camber variation (Fig. 4.3b) and vertical force (Fig. 4.4) give the same results as for the integration of the coil spring.

Nonetheless, since the beam model is different, stresses along the leaf will be different. Using the bending force on the leaf in Fig. 4.5a, the bending stress $\sigma(y)$ of the unidirec-

tional laminate leaf spring is computed using classic straight beam theory. For a fiber located at a vertical distance z from the neutral axis, it yields

$$\sigma(y) = \frac{z}{2}\frac{M(y)}{I} = \begin{cases} \frac{z}{2}\frac{12F(\frac{L}{2}-|y|)}{bt^3}, & \text{for } y \in \left[-\frac{L}{2};-\frac{l}{2}\right] \text{ and } \left[\frac{l}{2};\frac{L}{2}\right] \\ \frac{z}{2}\frac{12Fc}{bt^3}, & \text{for } y \in \left[-\frac{l}{2};\frac{l}{2}\right] \end{cases} \tag{4.18}$$

The maximum stress is found at the extreme fibers of the leaf at and in-between the supports. Eq. (4.18) is particularised to find the maximum bending stress and writes

$$\sigma_{max} = \frac{t}{2}\frac{12Fc}{bt^3}. \tag{4.19}$$

The maximum bending stress along the wheel stroke is pictured in Fig. 4.9.

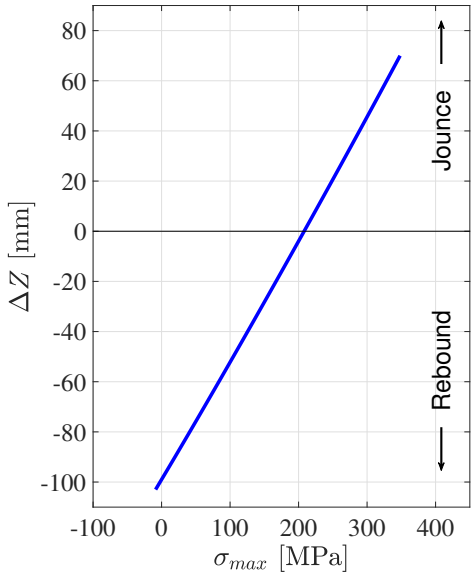

Figure 4.9: Maximum bending stress during jounce and rebound for the leaf spring with integration degree 2a, computed using the 2D model in MATLAB.

As it can be seen in Fig. 4.9, the maximum bending stress occurs at full jounce and is 348MPa. Failure is assessed using Tsaï-Wu criterion Eq. (3.38) for the maximum bending stress:

$$\begin{aligned} F_1\sigma_1 + F_{11}\sigma_1^2 &= \left(\frac{1}{\sigma_1^T} - \frac{1}{\sigma_1^C}\right)\sigma_x + \frac{\sigma_x^2}{\sigma_1^T\sigma_1^C} \\ &= \left(\frac{1}{1082} - \frac{1}{620}\right)348 + \frac{348^2}{1082 \cdot 620} = 0.059 < 1. \end{aligned} \tag{4.20}$$

The failure criterion is therefore satisfied, which means that the design is safe. The associated safety factor yields $R = 3.11$.

For the maximum jounce position of the suspension, the stresses along the beam are computed using Eq. (4.18). Results are pictured in Fig. 4.10

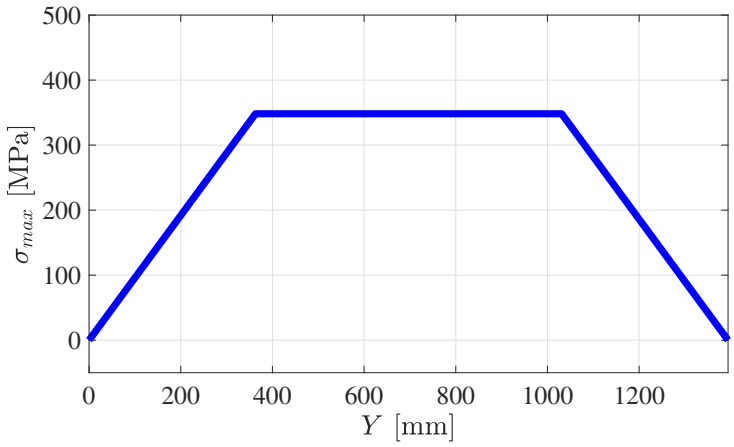

Figure 4.10: Maximum bending stress along the leaf spring in the case of maximum jounce of the suspension, integration case 2a.

4.2.4 Roll stiffness

In the case the leaf integrates the anti-roll bar, an equivalent roll stiffness K_ϕ of the axle can be computed due to the mounts of the leaf allowing a transfer of moment. This value can easily be computed using an equivalent suspension model of a rigid axle with two springs of equal stiffness K_S as shown in Fig. 4.11. Please note that the length L is chosen as the distance between the leaf eyes in the standard position.

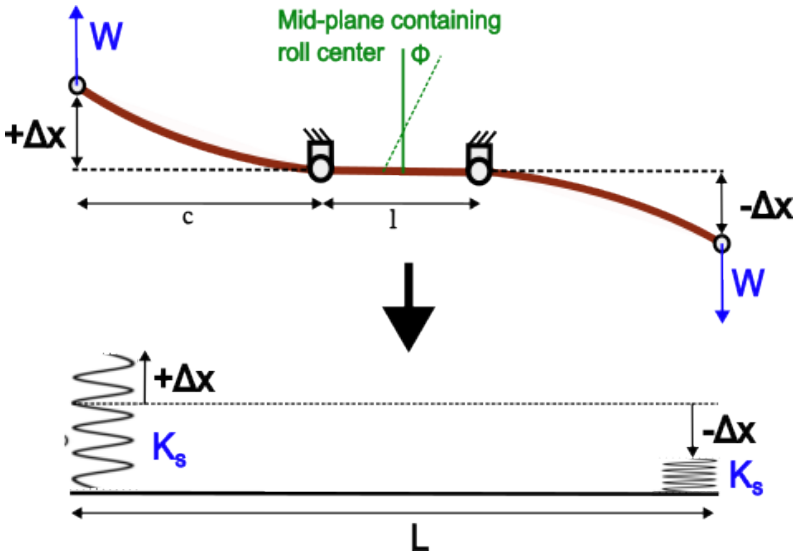

Figure 4.11: Equivalent suspension model .

Using the formula for the deflection of the leaf spring Eq. (3.17), the total deflection of the spring is obtained by summing the contribution of both loads W on one of the ends.

For the left end of the leaf, this yields

$$\Delta x = \underbrace{\frac{Wc^2}{3EI}(c+l)}_{\text{from } +W} \underbrace{-\frac{Wc^2}{6EI}(l)}_{\text{from } -W} = \frac{W}{6EI}(2c^3 + c^2 l). \tag{4.21}$$

Therefore, the stiffness of the equivalent springs writes

$$K_S = \frac{W}{\Delta x} = \frac{6EI}{2c^3 + lc^2} \tag{4.22}$$

and the roll stiffness can be computed using the geometry of the equivalent axle

$$K_\phi = \frac{1}{2} K_S L^2 = \frac{1}{2} \frac{6EI}{2c^3 + lc^2} L^2. \tag{4.23}$$

With the current geometry of the leaf spring, this leads to a roll stiffness $K_\phi = 936\text{Nm/deg}$ for the rear axle. Compared to standard roll stiffness of rear axles in production cars, this value has a good order of magnitude but is quite superior as the expected value, as most rear axles have a roll stiffness that lies in between 400Nm/deg and 600Nm/deg [11].

As it can be seen in Eq. (4.23), the roll stiffness explicitly depends on the distance between the mounts l. Using the relation $c = (L - l)/2$, Eq. (4.23) can be written as a function of l only

$$K_\phi = \frac{1}{2} \frac{6EI}{2(\frac{L-l}{2})^3 + l(\frac{L-l}{2})^2} L^2 = \frac{12EI}{(L-l)^3 + l(L-l)^2} L^2. \tag{4.24}$$

From Eq. (4.24), it is clear that increasing the distance between the mounts allows an increase in the roll stiffness. However, changing the distance between the leaf mounts will have an impact on the leaf spring rate K, as it also depends on l. To keep the same spring rate K, EI is also expressed as a function of l

$$K = \frac{6EI}{2(\frac{L-l}{2})^3 + 3(\frac{L-l}{2})^2 l} \Rightarrow EI = \frac{K \cdot (2(\frac{L-l}{2})^3 + 3(\frac{L-l}{2})^2 l)}{6}. \tag{4.25}$$

Eq. (4.25) shows that for an increasing distance between mounts l, EI decreases. Hence, since the width is fixed, the thickness of the leaf t decreases with increasing l.

With Eq. (4.25), Eq. (4.24) becomes,

$$K_\phi = \frac{2K(2(\frac{L-l}{2})^3 + 3(\frac{L-l}{2})^2 l)}{(L-l)^3 + l(L-l)^2} L^2. \tag{4.26}$$

The change of roll stiffness with the length between the leaf mounts and the associated change in leaf thickness are graphically represented in Fig. 4.13 and Fig. 4.12 respectively.

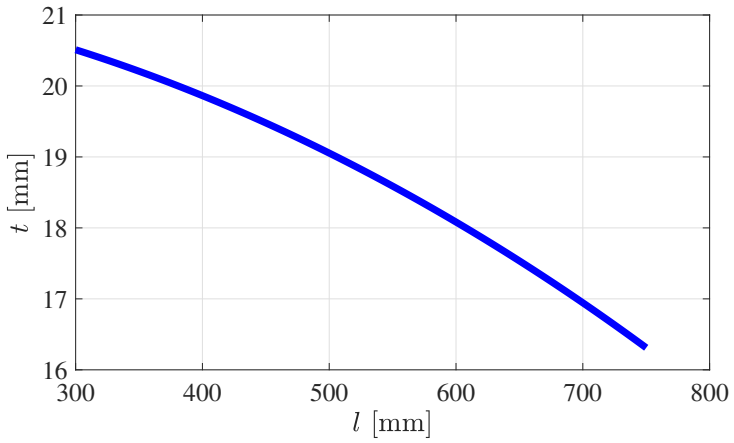

Figure 4.12: Variation of the leaf thickness as a function of the length between the leaf mounts.

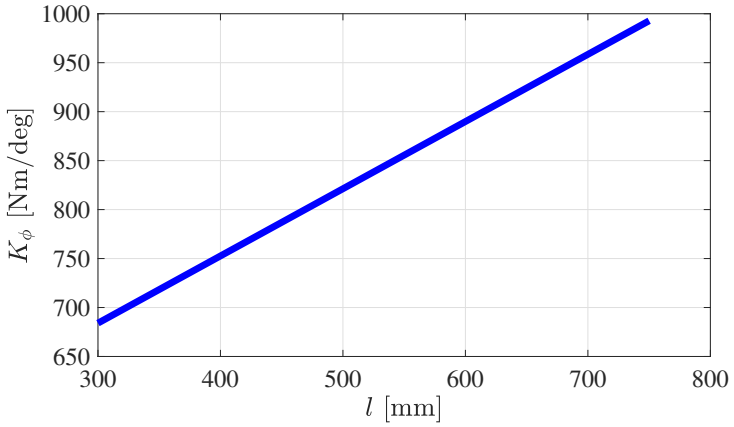

Figure 4.13: Variation of the equivalent roll stiffness as a function of the length between the leaf mounts.

As expected, Fig. 4.13 shows that the equivalent roll stiffness of the axle grows by increasing the distance between the supports. In fact, changing the length between the supports of the leaf is one of the most common procedures to tune the anti-roll effect [13]. Another way to tune the anti-roll effect is to change the width and thickness of the center part (between mounts) of the leaf. This second method cannot be evaluated analytically as the assumption is done that the leaf has a constant cross section.

4.2.5 Dynamic loading

In this case, most worst case scenarios in Table 3.2 can be evaluated. As for the integration of the spring, longitudinal loads are ignored since they are taken up by the rigid suspension arms. Therefore, the configuration for the suspension for panic braking is trivially found, as it corresponds to a vertical load of 0.8g. For this load, Fig. 4.4 gives a vertical wheel stroke of -22.4mm from the standard position.

With the longitudinal load not having effects on the leaf, rear pothole bump and bump during cornering can be solved with the same methodology. They will also lead to the same results, as the affected wheel will be in bump stop (or maximum jounce) position with the excess force being entirely carried over by the lower arm and the bump stop spring element. Both cases are pictured in Fig. 4.14.

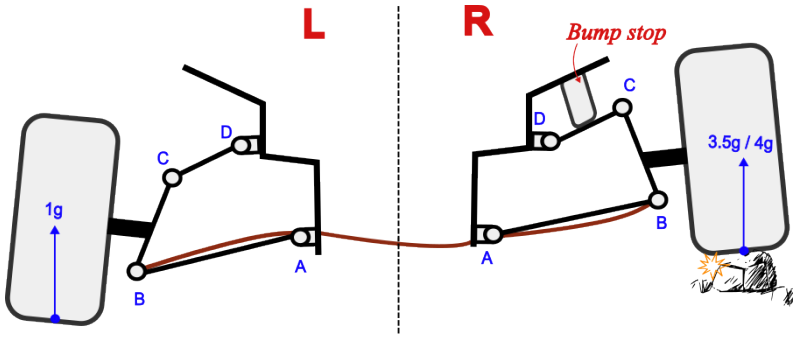

Figure 4.14: Loading case for the pothole/cornering bump (integration of the ARB).

To solve this statics problem, the principle of superposition is used. The loading of the beam model is therefore separated in two parts: a first part corresponding to the standard driving conditions (Fig. 4.15a) and a second part corresponding to the additional vertical force on the spring due to the bump (Fig. 4.15b). Note that for the computations and the schematics, right wheel will correspond to the wheel affected by the bump and will be denoted R whilst left wheel will be denoted L.

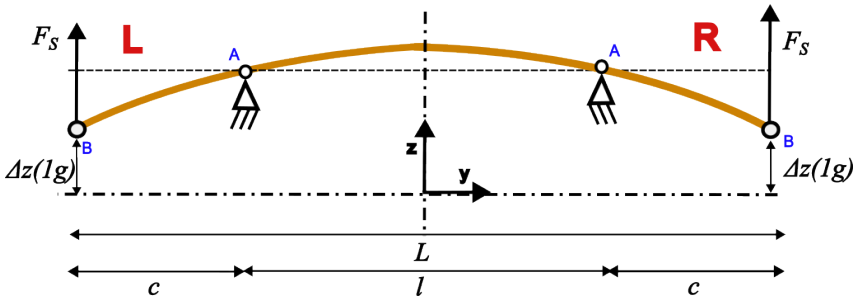

(a) Standard position

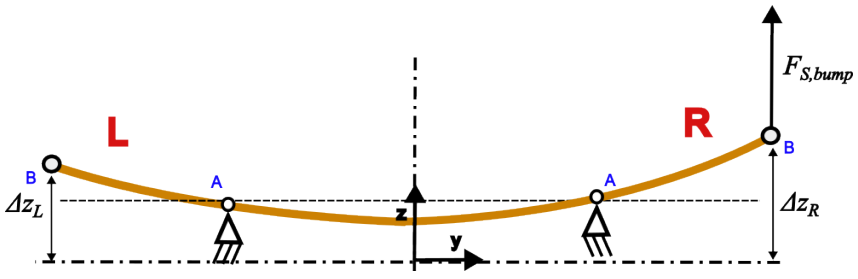

(b) Deformation due to bump

Figure 4.15: Separation of the loading cases for the pothole/cornering bum (ARB integration). (a) standard position and loads from for the leaf. (b) deformation due to the supplementary vertical force due to the bump.

First, the position of z_B due to the 1g load in Fig. 4.15a is determined using the initial configuration of the suspension. It yields, for both wheels under 1g vertical loading in the contact patch, $z_B = 217$mm. Using the configuration of the suspension at bump stop, the additional vertical displacement made by the right end of the leaf Δz_R is assessed:

$$\Delta z_R = z_B(bump) - z_B(1g) = 285 - 217 = 68\text{mm}. \tag{4.27}$$

With the vertical right displacement known, the additional force acting on right side of the leaf is determined using Eq. (3.18).

$$F_{S,bump} = \frac{3\Delta z_R EI}{c^2(c+l)} = \frac{3 \cdot 68 \cdot 39 \cdot 10^3 \cdot 100 \cdot 17.3^3}{12 \cdot 363^2 \cdot (363+668)} = 2527\text{N}. \tag{4.28}$$

Using Eq. (3.17), the induced displacement of the left side Δz_L of the leaf due to the load on the right side $F_{S,bump}$ writes

$$\Delta z_L = \frac{F_{S,bump} c^2 l}{6EI} = \frac{2527 \cdot 363^2 \cdot 668 \cdot 12}{6 \cdot 39 \cdot 10^3 \cdot 100 \cdot 17.3^3} = 22\text{mm}. \tag{4.29}$$

This 22mm displacement of the leaf end corresponds to a 23mm vertical displacement of the wheel. Finally, for both pothole and cornering bumps, the configuration of the rear axle is a vertical displacement of 70mm for the wheel affected by the bump and a 23mm vertical displacement for the other wheel.

For the lateral kerb strike case, a similar approach can be used to compute the suspension configuration.

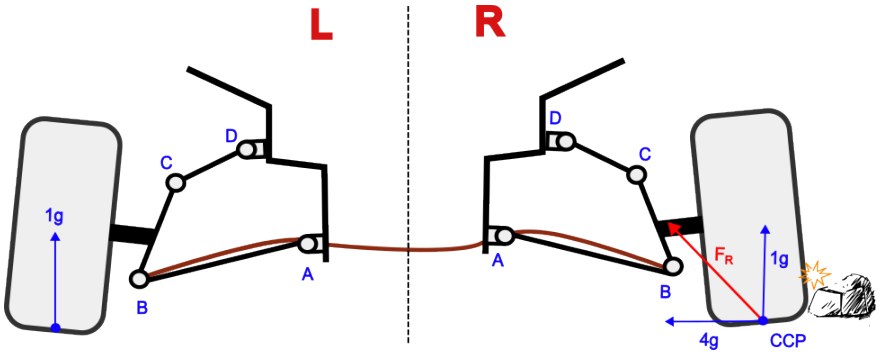

Figure 4.16: Loading case for the lateral kerb impact bump (ARB integration).

The position of the wheel is found by solving Eq. (3.59) combined with the beam model which yields at the impacted wheel

$$F_{S,vert} = \Delta z_R \frac{3EI}{c^2(c+l)}. \tag{4.30}$$

Solving Eq. (3.59) iteratively, the displacement corresponding to the lateral kerb is z_{CPC} = −53.4mm. The displacement on the other wheel writes

$$\Delta z_L = \frac{F_{S,vert} c^2 l}{6EI} = -12\text{mm}. \tag{4.31}$$

4.3 Coil spring and lower arm integration

The analytical methodology is applied to the case where the leaf integrates the coil springs and lower suspension arm, which is denoted integration degree 2b in Table 3.1.

4.3.1 Geometry of the leaf

With the integration of the arm by the leaf, a new spring rate K has to be computed based on the new motion of the suspension. As for previous designs, the choice is made to keep the same standard and unloaded positions from the original coil spring suspension. Based on the configurations computed using Eq. (3.87), the vertical displacement between unloaded and standard positions writes

$$\Delta z_B = z_B(F = 2859\text{N}) - z_B(F = 0\text{N}) = 216 - 102 = 114\text{mm}. \tag{4.32}$$

Combined with Eq. (3.54) and the pure bending assumption, the spring rate of the leaf writes

$$K = \frac{F_Z}{\Delta z_B} \frac{\sin(\tan^{-1}(\frac{z_B - z_G}{y_B - y_G}))\, \sin(\frac{\pi}{2} + \theta_3)}{\sin(\tan^{-1}(\frac{z_B - z_G}{y_B - y_G}) - \theta_3)}. \tag{4.33}$$

Solving Eq. (4.33) with F_Z = 2859N, this gives K = 26.68N/mm.

With the value of the spring rate, cross section of the leaf is computed by using straight beam theory, similarly to Section 4.1.1. The thickness of the leaf yields

$$t = \sqrt[3]{\frac{12L^3K}{3E_x b}} = \sqrt[3]{\frac{12 \cdot 363^3 \cdot 26.68}{3 \cdot 39 \cdot 10^3 \cdot 100}} = 11\text{mm}. \tag{4.34}$$

Computing the constant curvature with Eq. (3.11), the complete geometry of the unloaded leaf is known and pictured in Fig. 4.17.

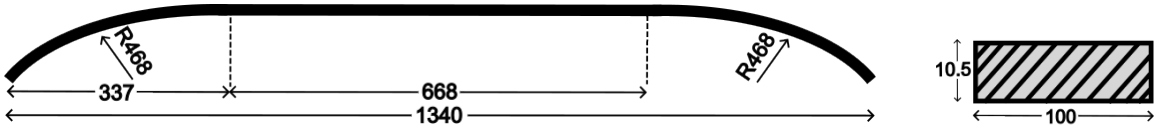

(a) 2D Geometry **(b)** Cross section

Figure 4.17: Initial 2D geometry of the leaf spring for integration degree 2b (a) and its cross section (b).

The total mass of the leaf is computed using the geometry.

$$M = bt(2L + l)\rho = 100 \cdot 11 \cdot (2 \cdot 363 + 668) \cdot \frac{2000}{10^9} = 3.07\text{kg} \tag{4.35}$$

For the original suspension, the mass of the two springs is 5.6kg and the lower arms (left and right wheels) can be estimated to have a mass of 4kg each. The integration of the leaf therefore represents a 78% mass saving on the rear axle.

Analogously to the other designs, the criterion validating the use of the Euler-Bernoulli straight beam theory in Eq. (3.33) writes

$$\frac{3EI}{\kappa' L^2 AG} = \frac{3E_x bt^3}{12\kappa' L^2 btG_{xy}} = \frac{3 \cdot 39 \cdot 100 \cdot 10.5^3}{12 \cdot 5/6 \cdot 363^2 \cdot 100 \cdot 11 \cdot 3.7} = 0.003 << 1, \tag{4.36}$$

ensuring that shear deformation can be neglected.

4.3.2 Modal analysis

The computation of the first natural frequencies is performed analogously as for the integration of the coil spring in Section 4.1. Using Eq. (4.8), the first three natural frequencies of the leaf are computed and gathered in Table 4.2.

n	Coefficient α_n	Natural frequency f_n
1	1.875	31.8Hz
2	4.694	79.5Hz
3	7.885	133.5Hz

Table 4.2: First three natural frequencies of the leaf spring for integration degree 2b.

The leaf should not enter in resonance while driving, as the first natural frequencies are all greater than the 12Hz produced by the road irregularities.

4.3.3 Kinematic analysis

The transverse leaf spring suspension is first studied over its wheel stroke using Eq. (3.87). With the computed configurations of the suspension, half-track and camber variation are computed and are drawn in Fig. 4.18.

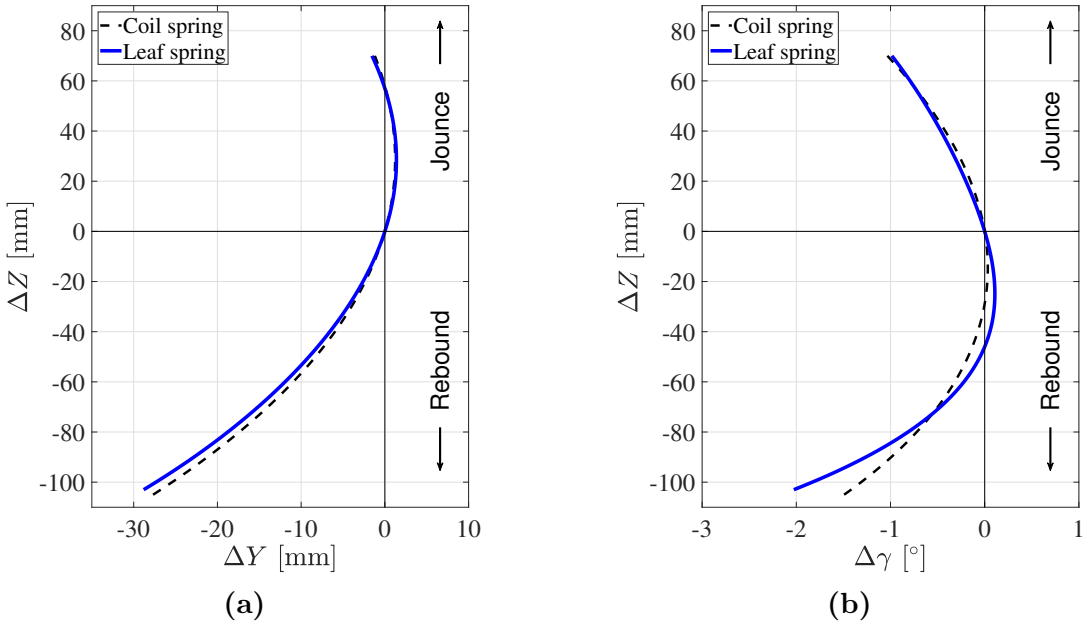

Figure 4.18: Half-track (a) and camber (b) variation during jounce and rebound for the leaf spring with integration degree 2b, computed using the 2D MATLAB model and compared with the results from the original suspension.

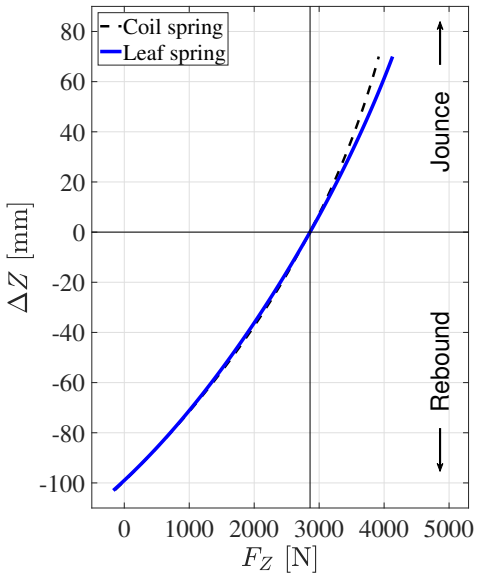

Figure 4.19: Vertical static loading in the contact patch center during jounce and rebound for the leaf spring integration degree 2b, computed using the 2D MATLAB model and compared with the results from the original suspension.

As shown in Fig. 4.18a, half-track variation for the leaf spring integrating the coil spring and the lower arm is similar to the one of the original suspension, with a small overshoot of maximum 1mm in the minimum rebound position. The camber variation in Fig. 4.18b however is a bit different. In rebound, the new suspension design is gaining more positive camber before rapidly gaining more negative camber compared to the initial design. In jounce, the gain of negative camber is close to the one of the original design.

The initial camber value is the same as for the initial suspension in 2D, which was expected since the initial configuration of the new design is based on the configuration of the initial design.

For the vertical wheel force in the contact patch, results from the new suspension are similar to the original suspension design, as shown in Fig. 4.19. The maximum force in the contact patch is 3953N, which is 35N more than the original design.

As the lower arm is suppressed, the lateral force is not withheld by the arm anymore. To verify the assumption that was made to neglect the deformation caused by this lateral force, the lateral force acting on the leaf is computed along the wheel stroke and plotted in Fig. 4.20a.

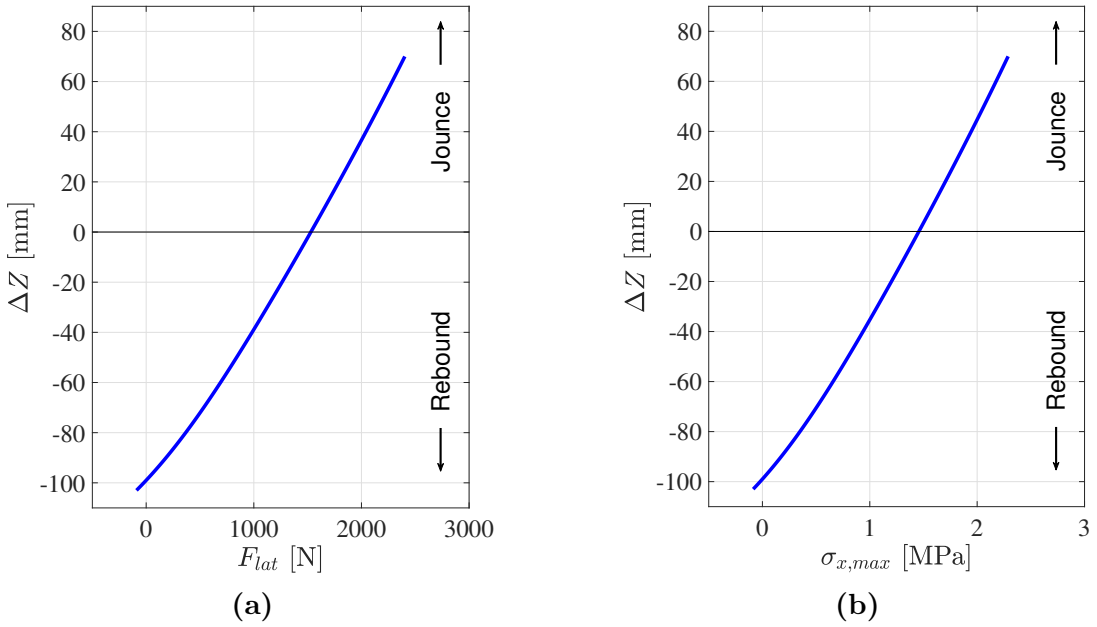

Figure 4.20: Lateral static loading acting on the leaf (a) and maximum axial stress (b) during jounce and rebound for the leaf spring with integration degree 2b, computed using the 2D MATLAB model.

The maximum lateral force acting on the leaf yields $F_{lat,max}$ = 2300N at the maximum jounce position. Using straight beam theory, the maximum axial deformation δ_{max} can be evaluated using Eq. (4.37).

$$\delta_{max} = \frac{F_{lat,max} L}{E_x A} = \frac{2300 \cdot 363}{39 \cdot 10^3 \cdot 100 \cdot 11} = 0.02\text{mm} \tag{4.37}$$

The maximum axial deformation is negligible and the previously made assumption that the leaf is subjected to pure bending can be considered valid. Using Fig. 4.20a, the maximum axial stress $\sigma_{x,max}$ (in the material axes) is computed along the wheel stroke

using Eq. (4.38).

$$\sigma_{x,max} = \frac{F_{lat}}{A} = \frac{F_{lat}}{bt} \tag{4.38}$$

The maximum axial stress along the wheel stroke is pictured in Fig. 4.20b and its maximal value at the maximum jounce is $\sigma_{x,max} = 2.3\text{MPa}$. Overall, the axial stress is very small and can be neglected when computing the failure criterion.

Maximum bending stress along jounce and rebound in Fig. 4.21b is computed using Eq. (4.10) with the vertical force acting on the leaf in Fig. 4.21a.

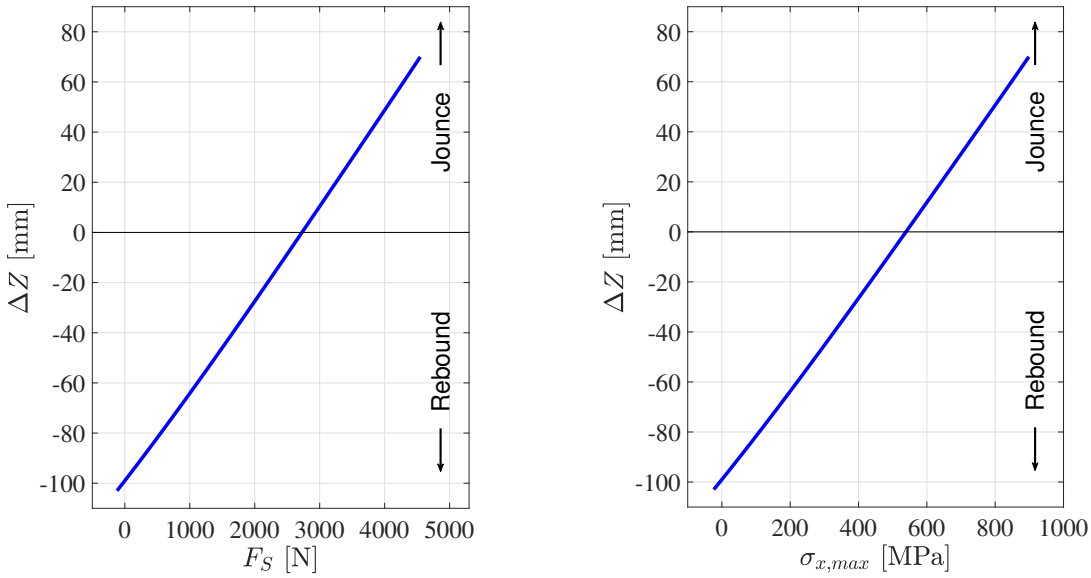

Figure 4.21: Vertical static loading acting on the leaf (a) and maximum bending stress (b) during jounce and rebound for the leaf spring with integration degree 2b, computed using the 2D MATLAB model.

Fig. 4.21b shows that the maximum bending stress acting on the leaf is 899MPa in the full jounce position. Failure is assessed using the Tsaï-Wu criterion, which writes with the axial stress neglected

$$\begin{aligned} F_1\sigma_1 + F_{11}\sigma_1^2 &= \left(\frac{1}{\sigma_1^T} - \frac{1}{\sigma_1^C}\right)\sigma_x + \frac{\sigma_x^2}{\sigma_1^T\sigma_1^C} \\ &= \left(\frac{1}{1082} - \frac{1}{620}\right)899 + \frac{899^2}{1082 \cdot 620} = 0.59 < 1. \end{aligned} \tag{4.39}$$

The failure criterion is therefore satisfied, which means that the design is safe. The associated safety factor yields $R = 1.20$.

For the maximum jounce position of the suspension, the stresses along the beam are computed using Eq. (4.9). Results are pictured in Fig. 4.22.

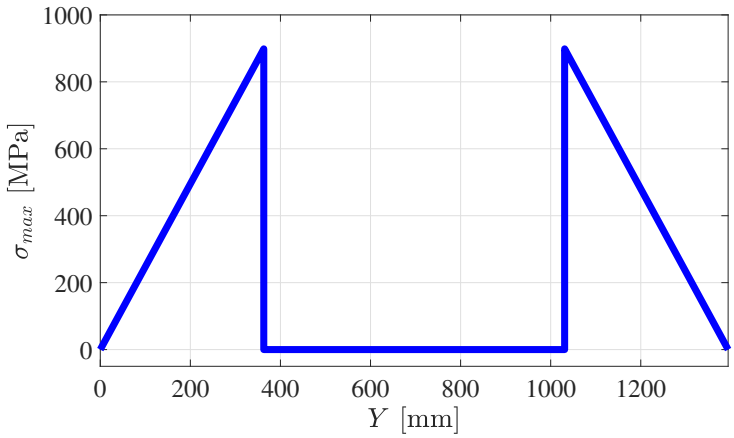

Figure 4.22: Maximum bending stress along the leaf spring in the case of maximum jounce of the suspension (integration degree 2b).

4.3.4 Dynamic loading

Rear pothole bump induces a longitudinal force that, now that the lower arm is removed, will impose a transverse deformation on the leaf spring. This deformation is studied independently from the lateral and vertical loads in the side view plane as shown in Fig. 4.23.

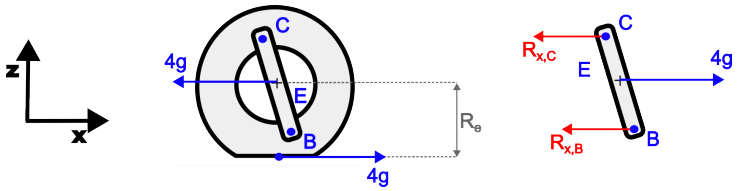

Figure 4.23: Longitudinal load from rear pothole bump on the wheel affected (integration degree 2b).

The force acting on the center of the wheel due to the 4g longitudinal load acting in the wheel contact patch is reacted on both points C and B trough reaction forces $R_{x,B}$ and $R_{x,C}$. The latter reaction force is not of interest, as the rigid upper arm withstand the reaction force, whilst the first is the one acting on the leaf spring. Using the geometry of the knuckle, the reaction force on the leaf $R_{x,B}$ yields

$$R_{x,B} = F_x \frac{CE}{CB} = 4 \cdot 2859 \frac{88}{187} = 5382\text{N}. \tag{4.40}$$

Using CLPT, the longitudinal deflection δ_x of the beam is evaluated. First, the stiffness matrix $\mathbf{Q}(0°)$ is computed.

$$\mathbf{Q}(0°) = \begin{bmatrix} m\ E_{xx} & m\ \nu_{yx}\ E_{xx} & 0 \\ m\ \nu_{xy}\ E_{yy} & m\ E_{yy} & 0 \\ 0 & 0 & G_{xy} \end{bmatrix} = \begin{bmatrix} 39637 & 2277 & 0 \\ 2277 & 8131 & 0 \\ 0 & 0 & 3700 \end{bmatrix} [MPa] \tag{4.41}$$

The membrane strains in the structural axes writes

$$\boldsymbol{\epsilon}^0 = \begin{bmatrix} \varepsilon_x \\ \varepsilon_y \\ \varepsilon_{xy} \end{bmatrix} = \boldsymbol{A}^{-1} \begin{bmatrix} N_x \\ N_y \\ N_{xy} \end{bmatrix} = [t\boldsymbol{Q}(0°)]^{-1} \begin{bmatrix} 0 \\ 0 \\ \frac{R_{x,B}}{b} \end{bmatrix} = \begin{bmatrix} 0 \\ 0 \\ 0.0014 \end{bmatrix} \tag{4.42}$$

Finally, the longitudinal deflection yields $\delta_x = b\varepsilon_{xy} = 0.14$mm. The stress associated to the longitudinal force is expressed with the strains in the material axes.

$$\begin{bmatrix} \sigma_x \\ \sigma_y \\ \sigma_{xy} \end{bmatrix} = \varepsilon_{12}\boldsymbol{Q}(0°) = \begin{bmatrix} 1 & 0 & 0 \\ 0 & 1 & 0 \\ 0 & 0 & 1 \end{bmatrix} \varepsilon_{12}\boldsymbol{Q}(0°) = \begin{bmatrix} 0 \\ 0 \\ 5.12 \end{bmatrix} \text{MPa}. \tag{4.43}$$

For the vertical loading due to the bump, the wheel affected is at the bump position ($\Delta z_{CPC} = +70$mm). With the suppression of the lower arm, the excess vertical force F_{ex} is no longer withheld by the arm but rather by the leaf. As shown in Fig. 3.21 from Section 3.3.1.4, the excess force will induce a lateral force on the arm F_B which writes

$$F_B = F_{ex} \frac{\sin(\frac{\pi}{2} - \theta_C)}{\sin(\theta_C)}, \tag{4.44}$$

with $\theta_C = \tan^{-1} \frac{z_{G'} - z_C}{y_{G'} - y_C}$. Using Fig. 4.19, the excess force is computed.

$$F_{ex} = F_z - F_{z'} = 4 \cdot 2859 - 3953 = 7483\text{N}. \tag{4.45}$$

Using the geometry of the suspension in bump, the lateral excess force is $F_B = 2531$N. This lateral force can be added to the lateral force computed in Fig. 4.20a in the maximum jounce position, $F_{lat,max} = 2402$N. The axial deformation in bump δ_y therefore yields

$$\delta_y = \frac{F_{lat} L}{EA} = \frac{(F_B + F_{lat,max})L}{E_x bt} = 0.04\text{mm}. \tag{4.46}$$

The maximum axial stress writes

$$\sigma_{x,lat} = \frac{F_{lat}}{A} = \frac{(F_B + F_{lat,max})}{bt} = 4.48\text{MPa} \tag{4.47}$$

With the axial stress computed from the bending of the leaf in the full jounce position $\sigma_{x,max} = 899$MPa, failure criterion can be verified for the pothole bump loading case.

$$\begin{aligned} F_1\sigma_1 + F_6\sigma_6 + F_{11}\sigma_1^2 + F_{66}\sigma_6^2 &= \left(\frac{1}{\sigma_1^T} - \frac{1}{\sigma_1^C}\right)\sigma_x + \frac{\sigma_x^2}{\sigma_1^T \sigma_1^C} + \frac{\sigma_6^2}{\tau_{12}^2} \\ &= \left(\frac{1}{1082} - \frac{1}{620}\right)(899 + 4.48) + \frac{(899 + 4.48)^2}{1082 \cdot 620} + \frac{5.12^2}{89^2} = 0.60 < 1. \end{aligned} \tag{4.48}$$

The criterion is therefore verified, ensuring the leaf does not break under the load.

For the bump during cornering, the position of the suspension is simply found at the bump stop position. As for previous case, a lateral force rises due to the excess vertical load in the contact patch. This excess force writes

$$F_{ex} = F_z - F_{z'} = 3.5 \cdot 2859 - 4130 = 5876\text{N}. \tag{4.49}$$

Using Eq. (4.44), the lateral force acting on the leaf is $F_B = 2457$N. As this force is lower than for the pothole bump case, we can ensure that the axial deformation of the leaf is negligible and that the failure criterion indicates that the design is safe.

For the lateral kerb strike, the position of the wheel is found by solving Eq. (3.60). To do so, the spring force $F_{S,vert}$ due to the kerb impact resulting force F_R is computed with $F_R = \sqrt{2859^2 + (4 \cdot 2859)^2} = 11788$N. Then, the position of the suspension corresponds to the one where $F_{S,vert} = K\Delta z_B$. In this case, the load applied on the spring is $F_{S,vert} = 955$N, which corresponds to a wheel displacement of -65.8mm and a stress of 189MPa. The lateral force acting on the leaf writes $F_{S,lat} = 11770$N, which yields

$$\delta_y = \frac{F_{S,lat} L}{EA} = 0.10\text{mm}. \tag{4.50}$$

The maximum axial stress therefore writes

$$\sigma_{x,lat} = \frac{F_{S,lat}}{A} = 10.7\text{MPa} \tag{4.51}$$

The lateral deformation and the stress caused by the lateral kerb strike are negligible, so that one can assume the failure criterion is satisfied.

For panic braking, the vertical position of the wheels is trivially given by Fig. 4.19 for a vertical force $F_Z = 0.8 \cdot 2859 = 2287$N: $\Delta Z_{CPC} = -16.5$mm. The deformation due to the longitudinal load must be computed differently from the rear pothole bump as, in this case, the longitudinal load comes from a braking force (outboard brakes). The lateral load is studied in the side view plane shown in Fig. 3.13.

$$F_{B,x} = F_X \frac{CE}{BE} \frac{R_e}{L_k} = 0.4 \cdot 2859 \frac{88}{99} \frac{318}{187} = 1729\text{N}. \tag{4.52}$$

Using CLPT as in Eq. (4.42) and Eq. (4.43), the longitudinal deflection is $\delta_x = 0.04$mm and the maximum shear stress in the laminate plies is $\sigma_{xy} = 1.57$MPa.

4.4 Complete integration

As explained in Section 3.2.2.2, the large deformation of the overhanging beam is not formulated analytically. It was therefore decided to consider that, for a preliminary design phase, it was acceptable to consider that the motion of the joint B is the same as if the arm was still present. Following this assumption, the leaf has therefore the same geometry as the one found for the integration degree 2a in Section 4.2.1.

4.4.1 Kinematic analysis

Kinematic analysis is also the same due to the assumption, even though for the 'real' leaf it should be different. However in this case, the lateral force acting on the leaf can be evaluated analogously to Section 4.3.3.

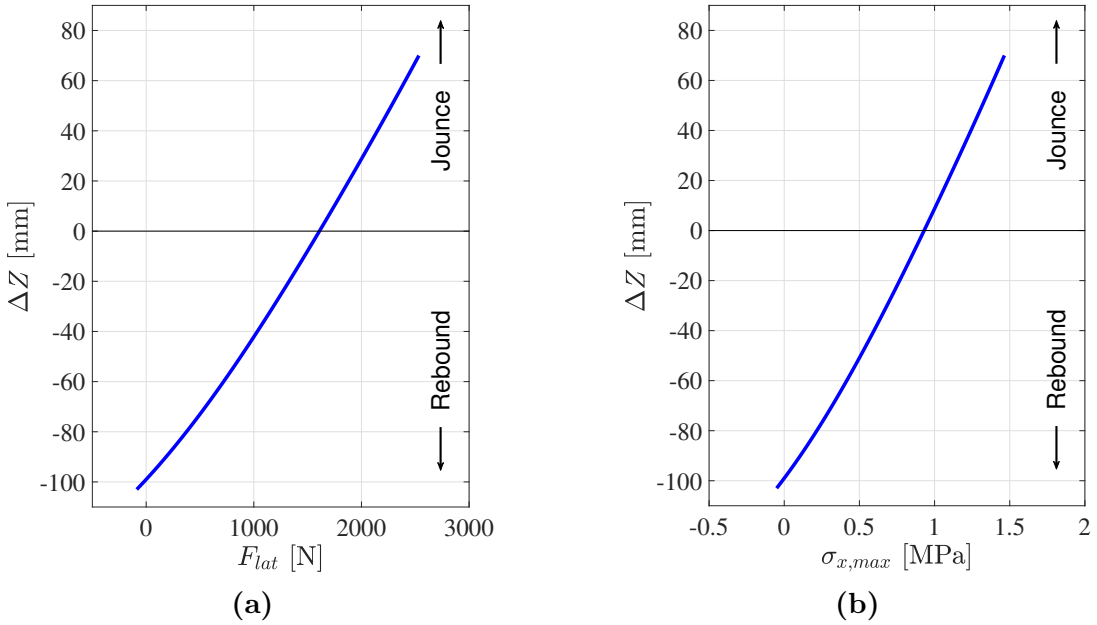

Figure 4.24: Lateral static loading acting on the leaf (a) and maximum axial stress (b) during jounce and rebound for the leaf spring with integration degree 3, computed using the 2D MATLAB model.

Fig. 4.24a shows that the maximum lateral force on the free end of the leaf is F_{lat} = 2533N when the suspension is in the maximum jounce position. Using beam theory, the maximum axial deformation yields

$$\delta_{max} = \frac{F_{lat,max} L}{E_x A} = \frac{2533 \cdot 363}{39 \cdot 10^3 \cdot 100 \cdot 17.3} = 0.014\text{mm} \tag{4.53}$$

The maximum axial deformation is negligible and the previously made assumption that the leaf is subjected to pure bending can be considered valid. Using Fig. 4.24a, the maximum axial stress $\sigma_{x,max}$ (in the material axes) is computed along the wheel stroke

using Eq. (4.38) and is pictured in Fig. 4.24b. Its maximal value at the maximum jounce is $\sigma_{x,max}$ = 1.46MPa. Overall, the axial stress is very small and can be neglected when computing the failure criterion.

4.4.2 Dynamic loading

As the lower arm is suppressed, one can assess the deformation due to the lateral and longitudinal load acting on the leaf. However, as it was observed for integration degree 2b in Section 4.3, those loads are very small and lead to negligible change in longitudinal/lateral motion and in the stresses. Results from the different worst case loading scenarios in Table 3.2 can therefore be assumed the same as for integration degree 2a of the leaf in Section 4.2.5.

4.5 Comparison of the designs

Preliminary designs are compared based on their computed kinematic curves, which are the camber variation curves in Fig. 4.25, half-track variation curves in Fig. 4.26 and static vertical force in the contact patch in Fig. 4.27. Results from the integration degree 3 are ignored since the 'real' behavior of the suspension could not be assessed in this case. A last comparison is made based on the mass that is saved by the design in Table 4.3.

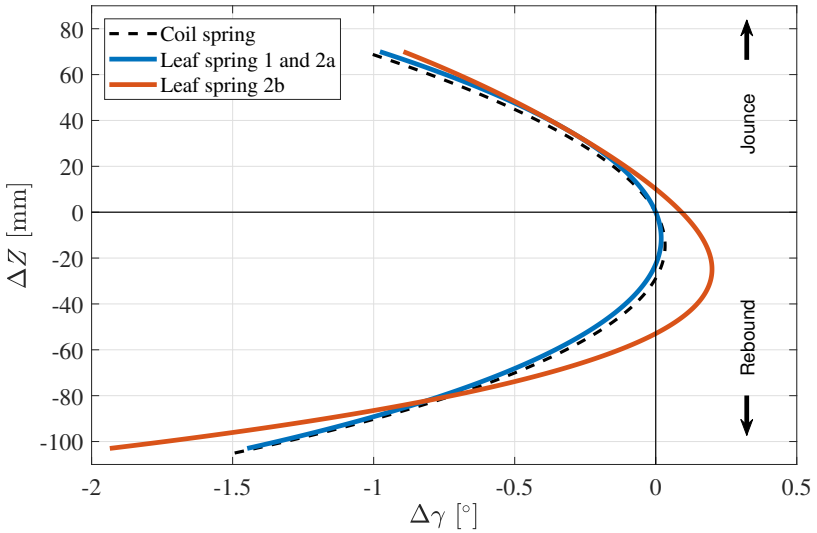

Figure 4.25: Comparison of the camber variation curves for the preliminary designs based on their integration degree with reference solution from the original suspension design.

Fig. 4.25 highlights the fact that the suppression of the lower arm has an impact on the camber variation. In jounce, the suppression of the arm has few impact on the camber gain. A more important positive camber gain is observed at the start of the rebound phase that becomes a huge negative camber gain in the latter phase of the rebound. This

may be explained by the fact that the leaf in large deformation first experiences small lateral deflection that is increased as the vertical deflection grows, as it can be deduced from Eq. (3.28).

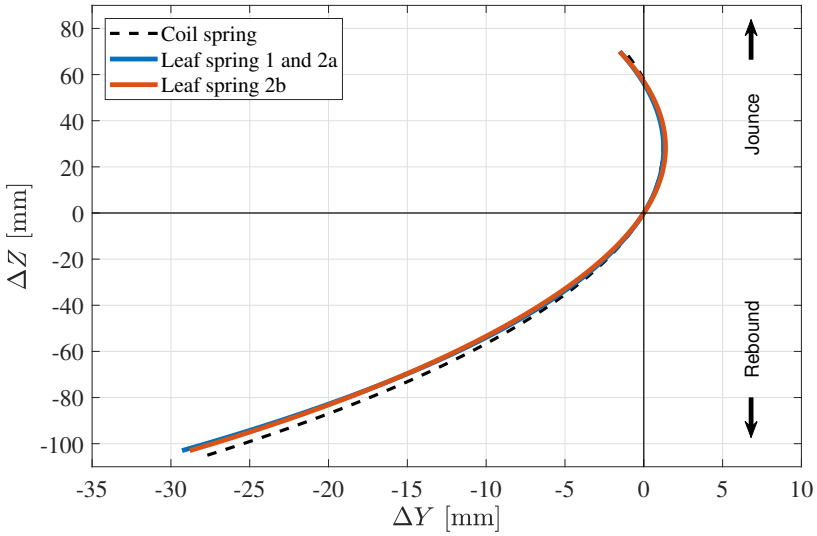

Figure 4.26: Comparison of the half-track variation curves for the preliminary designs based on their integration degree with reference solution from the original suspension design.

Fig. 4.26 shows that half-track variation is not affected by the suppression of the lower arm. The small difference compared with the reference coil spring suspension is explained by the rotation that was applied on the 3D model to derive the 2D model on which results for the leaf springs are based.

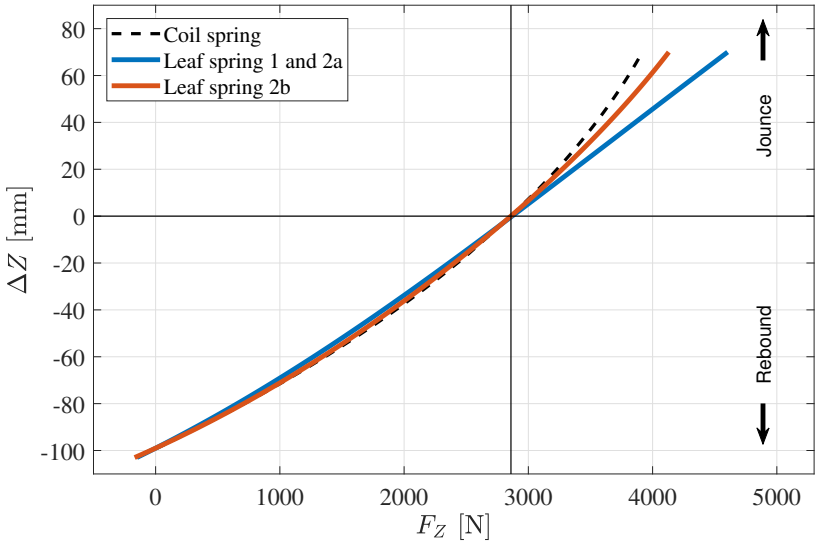

Figure 4.27: Comparison of vertical contact patch force curves for the preliminary designs based on their integration degree with reference solution from the original suspension design.

Fig. 4.27 shows that in rebound, suspension forces are similar whether a coil or a

transverse leaf spring is used. In jounce, the transverse leaf spring gives a more linear evolution of the vertical contact patch force. This means that the transverse leaf spring suspension gives a better road holding in jounce, hence reducing the comfort [11]. On the other hand, the more linear vertical loading has also a positive impact on the vibratory comfort. The most convenient value for the first natural frequency of the sprung mass should be close to 1Hz, which is optimal for a human body in the driving seat [11]. Therefore, the suspension should ideally become stiffer as the payload is increased. This is not the case for the original suspension as the vertical force decreases when the payload is increased. This effect is reduced for the transverse leaf spring suspension, as the payload is quasi-proportional with the suspension travel, and should therefore have a smaller natural frequency. When the lower arm is suppressed (integration degree 2b), the 'linearity' of the evolution of the vertical force is reduced. This behavior can be explained by the fact that, in jounce, the lower arm has a low angle θ_1 which means that the force transmitted by the leaf spring is purely vertical. In the case the lower arm is suppressed, a lateral force is added due to the geometry of the suspension.

Component	Mass [kg]	Quantity [-]
Coil spring	2.8	2
Anti-roll bar	1	1
Lower arm	4	2
	Total mass	**14.6kg**

(a) SLA Coil springs (reference)

Component	Mass [kg]	Quantity [-]
Leaf spring	2.9	1
Anti-roll bar	1	1
Lower arm	4	2
	Total mass	**11.9kg**
	Saved mass	**-18.5%**

(b) SLA Leaf spring 1

Component	Mass [kg]	Quantity [-]
Leaf spring	4.9	1
Anti-roll bar	1	0
Lower arm	4	2
	Total mass	**12.9kg**
	Saved mass	**-12%**

(c) SLA Leaf spring 2a

Component	Mass [kg]	Quantity [-]
Leaf spring	3.1	1
Anti-roll bar	1	1
Lower arm	4	0
	Total mass	**4.1kg**
	Saved mass	**-72%**

(d) SLA Leaf spring 2b

Component	Mass [kg]	Quantity [-]
Leaf spring	4.9	1
Anti-roll bar	1	0
Lower arm	4	0
	Total mass	**4.9kg**
	Saved mass	**-67%**

(e) SLA Leaf spring 3

Table 4.3: Comparison of the mass accounting for suspension members in the case of the reference suspension and the different preliminary leaf designs.

As highlighted in Table 4.3, the integration of the leaf spring reduces the mass on the axle. However, it is observed that the integration of the anti-roll bar in the leaf spring leads to a diminution of the saved mass. This is discussed in the next section.

4.6 Improvements on the preliminary leaf design

In this section, possible ameliorations of the preliminary leaf designs are motivated and discussed based on the results obtained from the preliminary designs.

4.6.1 Shape optimisation

The width of the leaf has been defined and remains constant during the preliminary design of the leafs. However, changing the width (resp. thickness) has significant impact on the properties of the leaf. To illustrate these changes in properties, impact of the value of the width is assessed in the case of the leaf with integration degree 1. Computations are gathered in Fig. 4.28.

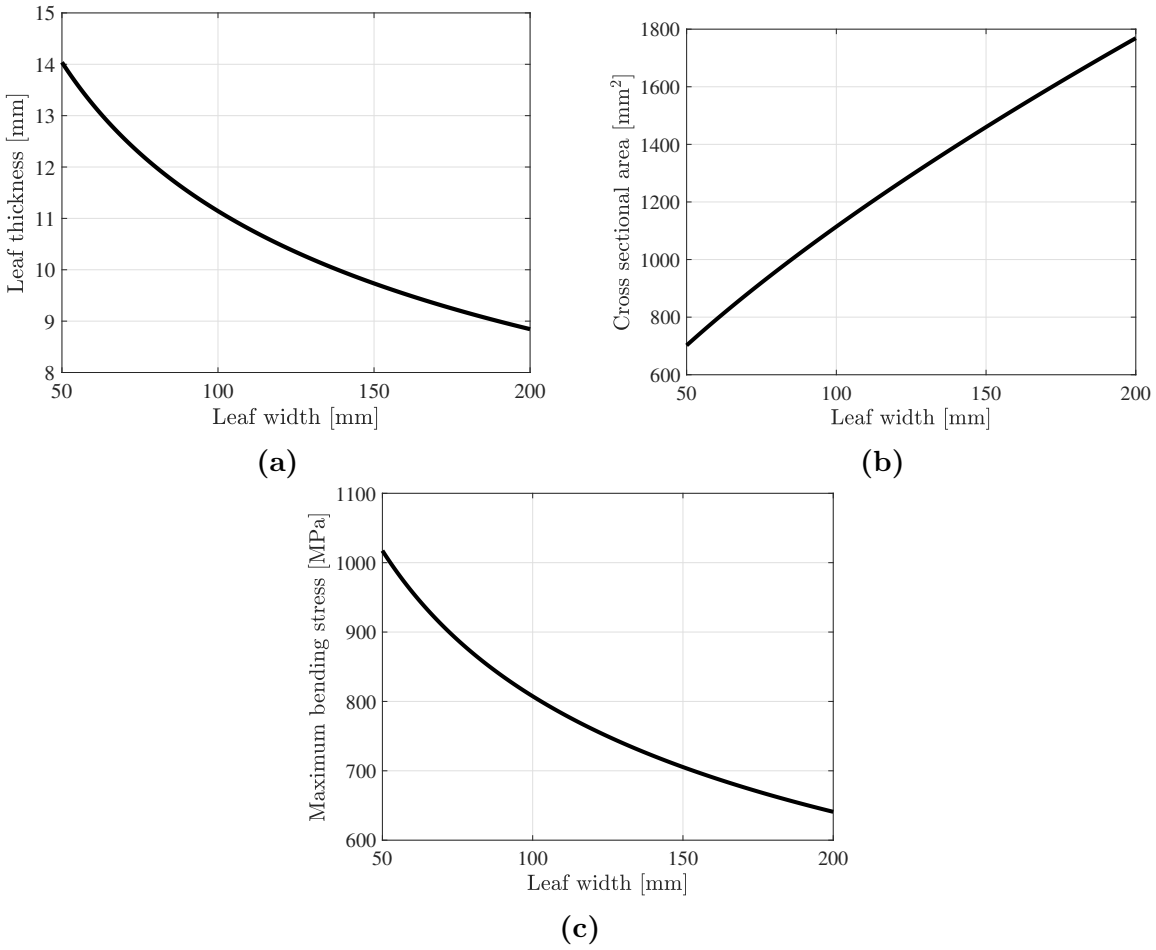

Figure 4.28: Effects of the variation of the leaf width on the thickness (a), cross sectional area (b) and maximum bending stress (c) for the leaf with integration degree 1.

As observed in Fig. 4.28a, the thickness of the leaf decreases when the width of the leaf increases. This is due to the stiffness ratio of the leaf, which is constant and therefore leads to $I = \frac{bt^3}{12} = cst$. Due to this relation, the cross section of the leaf increases when the width is increased, as pictured in Fig. 4.28b. Fig. 4.28c shows that a wider leaf leads to a decrease in the bending stress of the leaf.

Based on these results, a preliminary optimisation of the leaf shape can be deduced. As observed in Fig. 4.6, the maximum bending stress acting on the leaf occurs at the mounts where the leaf is attached to the car body. Close to the eyes of the leaf, the stress is null. Therefore, the idea would be to have a wider and thinner leaf close to the mounts and thicker and narrower close to the eyes while keeping the same area moment of inertia. This geometry would help homogenize and reduce stresses along the leaf and also reduce the mass of the leaf with the reduction of the cross sectional area toward the eyes. This shape is easy to manufacture using HP-RTM as previously discussed. Please note that these observations are also valid for other integration degrees of the leaf springs.

4.6.2 Anti-Roll property

As previously discussed in Section 4.2.4, the equivalent roll stiffness of the transverse leaf spring axle is too big compared to standard values for passenger cars (940Nm/deg *v.s.* 400Nm/deg). As discussed in Section 4.2.4, changing the position of the mounts can help tune the value of the equivalent roll stiffness. However, as shown by Fig. 4.13, the value remains too big (680Nm/deg) for the leaf spring even though the distance between the mounts is decreased to 300mm.

To further reduce the value of the equivalent roll stiffness, it is therefore necessary to modify the thickness of the leaf in-between the mounts, as advised by Michael Lamm [13]. However, as the assumptions made for the analytical design method require a constant cross section of the leaf, this behavior cannot be verified analytically. It is therefore necessary to use numerical computations to find an optimal shape of the leaf part between the mounts that will lead to the desired equivalent roll stiffness of the axle.

Chapter 5

Numerical study

The main objective of this chapter is to validate the analytical models and associated assumptions made in Chapter 3. To do so, static analysis is performed on numerical beam models based on the preliminary designs found in Chapter 4. They are then compared with static results from the analytical models.

5.1 Finite element modeling of the leaf

In order to perform finite element analysis of the leaf springs, it is necessary to build a finite element model. To model laminate structures, three types of finite elements can be used:

- Membrane finite elements (2D);
- (Mindlin) Shell elements (2D + thickness);
- Monolayer or multilayer solid elements (3D).

The most commonly used elements are the shells, which are less computationally expensive than solid elements while still providing accurate solutions. However, the use of such elements is limited by the Mindlin assumption, which assumes that the section remains straight under deformation, as shown in Fig. 5.1b. Under deformation, the real behavior of the composite leads to warping of its section, as shown in Fig. 5.1c.

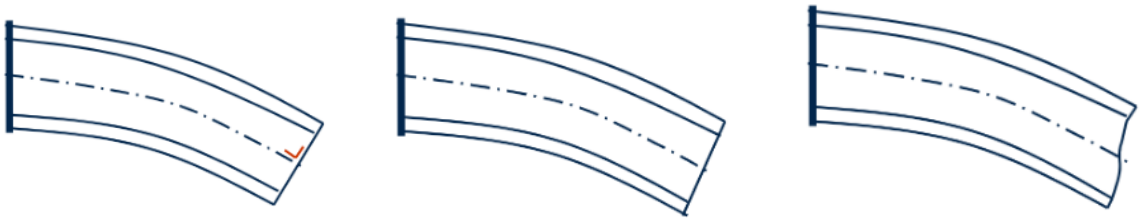

(a) Kirchoff **(b)** Mindlin **(c)** Real behavior

Figure 5.1: Kirchoff assumption (a), Mindlin assumption (b) and real behavior (c) of the section of [36].

To use the Mindlin shells, criteria Eq. (5.1) must be verified beforehand [36].

$$\frac{E}{G}\left(\frac{h}{L}\right)^2 < 1, \tag{5.1}$$

where h is the thickness and L is the total length of the plate. If Eq. (5.1) is verified, it is assumed that the cross section remains straight under the deformation. If Eq. (5.1) is not verified, one must resolve to the use of 3D solid elements.

In the case of the three leaf designs computed, Eq. (5.1) yields:

$$\text{Integration degree 1:} \quad \frac{39}{3.7}\left(\frac{11}{1340}\right)^2 = 7 * 10^{-4} < 1 \tag{5.2}$$

$$\text{Integration degree 2a:} \quad \frac{39}{3.7}\left(\frac{17.3}{1340}\right)^2 = 1.7 * 10^{-3} < 1 \tag{5.3}$$

$$\text{Integration degree 2b:} \quad \frac{39}{3.7}\left(\frac{11}{1342}\right)^2 = 7 * 10^{-4} < 1 \tag{5.4}$$

The criteria is valid for all designs, therefore leafs are modeled using Mindlin shell elements in the xy-plane.

Based on the geometries of the leaf in Fig. 4.1, Fig. 4.8 and Fig. 4.17, the curved leaf springs are modeled in Nx. Due to the very close geometries of leaf with integration degrees 1 and 2b, only one leaf model is analysed for both cases. Additionally, an equivalent straight beam model of the leaf is also created for future comparison. The leaf mounts are modeled using fixed constraints for integration degree 1 and 2b and using a user defined constraint allowing only rotation along the y-axis of the leaf. The mesh is made of 5mm elements, which allow a good convergence of the results for a relatively short computation time. Leaf models are pictured in Fig. 5.2 and Fig. 5.3.

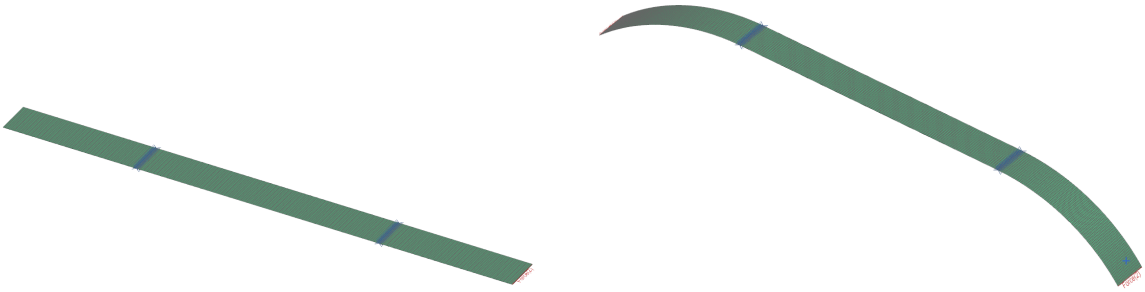

(a) Straight **(b)** Curved

Figure 5.2: Finite element models of the straight leaf (a) and of the curved leaf (b) for integration degrees 1 and 2b.

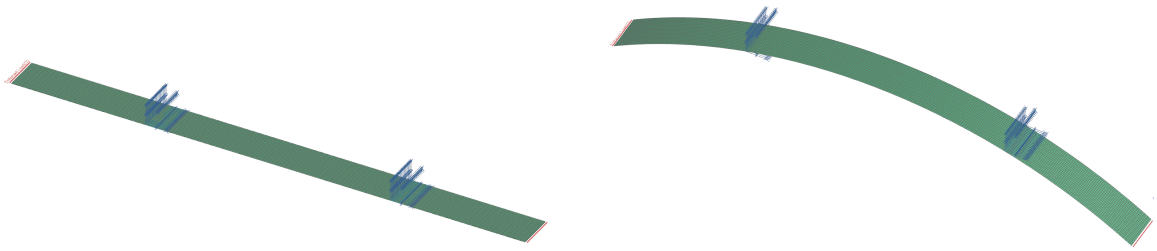

(a) Straight **(b)** Curved

Figure 5.3: Finite element models of the straight leaf (a) and of the curved leaf (b) for integration degree 2a.

5.2 Large displacements

In the analytical methodology, the 'free' (non-driven) large deformation of the cantilever beam (integration degree 2b) is modeled using the empirical relations from Ji Wang *et al.* [38] Eq. (3.28) and Eq. (3.29). To assess if this empirical relation is valid, the large displacement of the curved beam is computed using finite element method. To do so, curved leaf model in Fig. 5.2b is subjected to an imposed motion ΔZ = 142mm on both ends. To further compare with straight beam theory, the straight beam model is also subjected to an equivalent large deformation ΔZ = 142mm and a straight steel beam model of the same size is also modeled using tetrahedral (3D) elements and subjected to the same loads. The computations are performed using the NASTRAN SOL402 multi-step non-linear kinematics solver with a non-linear statics subcase and with the assumption of large displacements enforced. Results from the three computations are gathered and compared with the empirical solution and rotation of an equivalent rigid arm in Fig. 5.4.

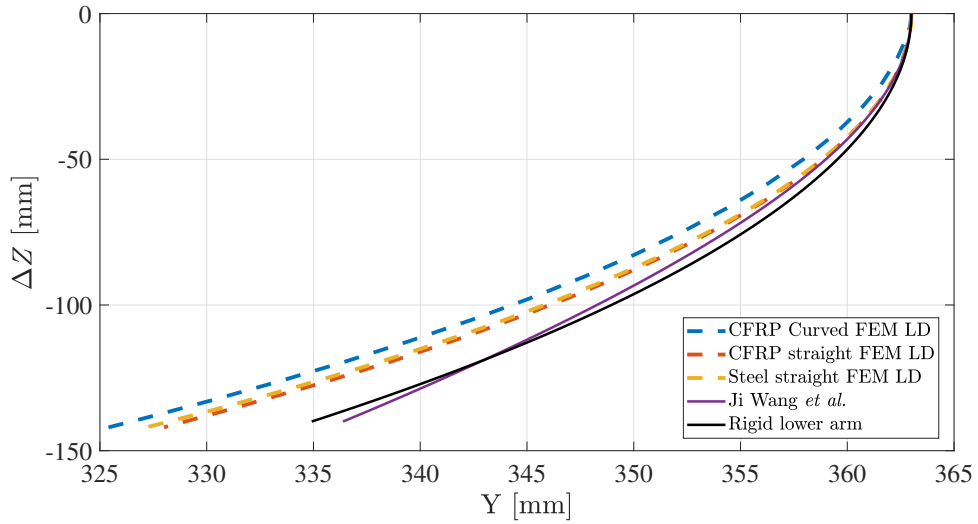

Figure 5.4: Comparison of the lateral deflection Y of the curved leaf spring (integration degree 2b) in large deformation (LD) versus lateral deflection of the equivalent straight leaf spring, straight steel leaf of the same length, empirical relation from Ji Wang *et al.* [38] and lateral deflection imposed by a rigid arm.

As it can be seen in Fig. 5.4, the analytical expression from Ji Wang *et al.* gives an accurate estimation of the lateral deflection of the straight beam for relatively moderate vertical displacement (<75mm). When the deformation is larger, the approximation leads to an increasing error, up to 10mm in this case which is significant for the camber variation for instance. Therefore, for the analytical computations of the deformation of the beam in large deformation, another analytical expression or a combination of several analytical expressions should be used. In fact, such expressions can be found Ji Wang *et al.*, where the authors combine the first approximation with a 30^{th} order polynomial expression when the vertical deflection becomes too big. On the other hand, large deformation of the straight composite is similar to the one of the steel straight beam. This was expected as the laminate is unidirectional and subjected to pure bending load. Finally, Fig. 5.4 highlights the expected difference between the initially curved beam and the straight beam, leading to a 3mm difference for the maximum deflection.

The same analysis is performed for the 'free' (non-driven) large deformation of the overhanging beam (integration degree 3). In this case, however, the results are only compared to the rotation of the equivalent rigid arm as no empirical expression was found. Associated results are gathered in Fig. 5.5.

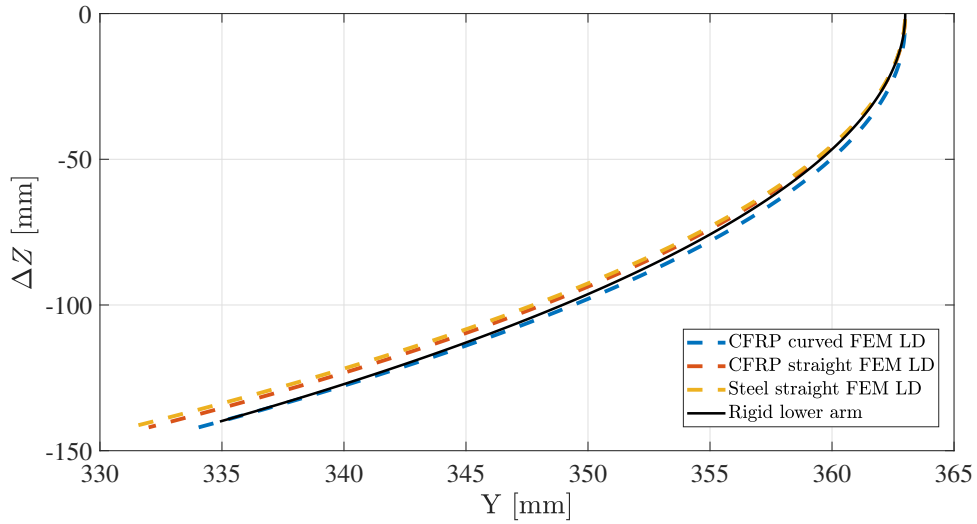

Figure 5.5: Comparison of the lateral deflection Y of the curved leaf spring (integration degree 3) in large deformation (LD) versus lateral deflection of the equivalent straight leaf spring, straight steel leaf of the same length and lateral deflection imposed by a rigid arm..

As it can be seen in Fig. 5.4, the large deformation of the overhanging beam is pretty similar in all cases. It is also worth to note that the rotating rigid arm gives a really accurate estimation of the large deformation of the curved beam. Therefore, a preliminary design for the leaf with complete integration of the suspension members (integration degree 3) could be computed using the kinematic model of the suspension with the lower arm.

5.3 Modal analysis of the leaf designs

Using NASTRAN SOL103, modal analysis is performed on the curved leafs (Fig. 5.2b and Fig. 5.3b). The first three mode shapes and associated natural frequencies are picture in Fig. 5.6 and in Fig. 5.7.

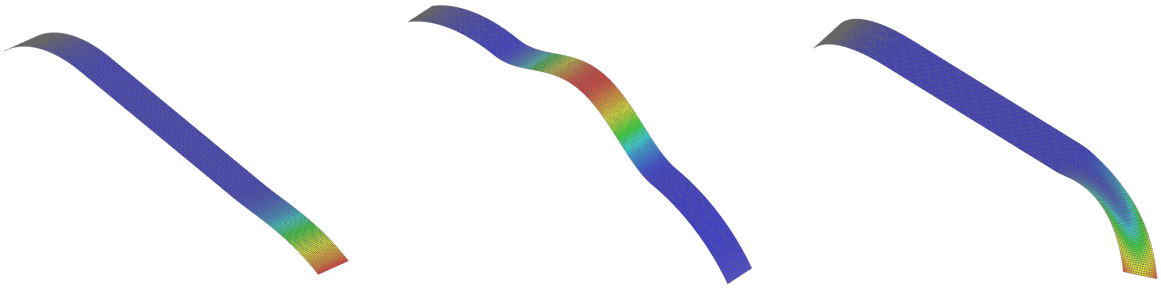

(a) Mode 1 - 56.85Hz **(b)** Mode 2 - 111.86Hz **(c)** Mode 3 - 150.75Hz

Figure 5.6: First three vibration mode shapes for integration degrees 1 and 2b.

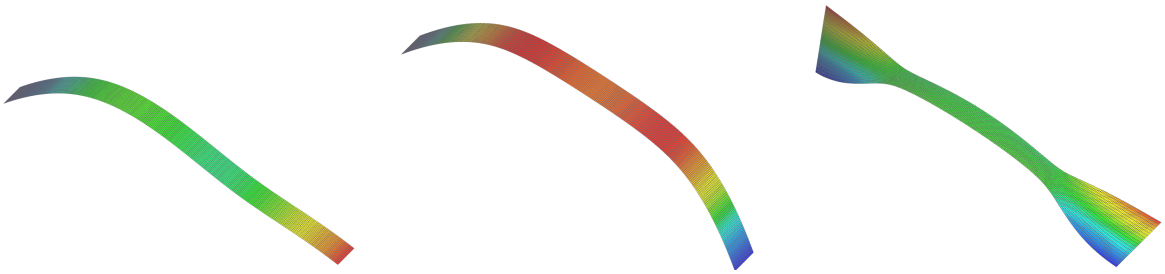

(a) Mode 1 - 62.15Hz **(b)** Mode 2 - 72.31Hz **(c)** Mode 3 - 311.06Hz

Figure 5.7: First three vibration mode shapes for integration degree 2a.

In a general observation, Fig. 5.6 and Fig. 5.7 show that both curved leafs experience two bending modes followed by a torsion mode. Compared to the analytically estimated natural frequencies of the leaf 1 in Table 4.1, natural frequencies of the curved beam are greater. Actually, mode shapes 2 and 3 were not predicted by the analytical relation in Eq. (4.8), as this relation only accounts for bending modes. Nonetheless, both curved leaf springs have natural frequencies that are greater than the estimated 12Hz produced by the road irregularities. This means that no failure coming from vibratory response should be expected for the leaf springs due to the road surfaces irregularities.

Conclusion

In this thesis, a general analytical approach in the design of transverse composite leaf springs has been established. Properties and impact of the integration of the transverse leaf spring onto the axles have been assessed using first the analytical approach and then correlating these results with the one obtained from the multi-body finite element analysis of the suspension. The development of the analytical method is summarised hereafter.

In the first chapter, the independent suspension model has been chosen to be the double wishbone suspension, as this type of suspension is the most general form of independent suspension. After selection of the suspension type, the 2004 Audi A6 has been defined as a case study. This car is equipped with a short long arm suspension on the rear axle, which is a particular case of the double wishbone suspension. The multi-body finite element model of the suspension was re-built and kinematic performance curves of the car have been computed to serve as benchmark in the design of the leaf springs. Analysis of the motion of the suspension highlighted the negative camber gain characteristic of short long arms suspensions, with the suspension having an initial camber angle of $-2.5°$. Analysis of the half-track variation of the suspension also brought out the fact that the suspension was initially tilted by an angle of approximately $-3.6°$ in the xz-plane of the car.

In the second chapter, the choice of the composite material was made. Amongst common material candidates in the manufacturing of leaf springs, E-Glass/Epoxy glass fiber reinforced laminate has been chosen based on a compromise between affordability, in the aim of mass produced elements, and better mechanical properties. Mechanical properties of the material have then been defined and manufacturing processes have been discussed. It came out that the high-pressure resin transfer molding (HP-RTM) was the most commonly used manufacturing method for composite leaf springs. However, short moulding compounds could also be of interest, as it is one of the cheapest method in the manufacturing of composite elements.

In the third chapter, the analytical leaf design methodology has been established. Transverse leaf spring designs are first separated according to suspension members they functionally integrate, named integration degrees. Joining classical laminated plate the-

ory with classical straight beam theory, leaf springs have been modeled according to their integration degree. Leaf springs integrating the anti-roll bar are modeled as overhanging beams whilst other leaf springs are modeled using a cantilever beam. Deformation of curved beams has been analysed and led to the conclusion that the leaf springs should rather be modeled using straight beams. Large deformation of the beams has also been discussed and an empirical model of the large deformation for cantilever beams has been defined. To assess the effects of transverse shear deformation for composite beams, Timoshenko's beam theory has been used to define a criterion under which shear deformation is considered negligible. The leaf model led to the assumption that the laminate had to be balanced and symmetric and that the cross section of the leaf had to be constant and rectangular. The suspension has also been modeled. First, methodologies for the computation of the suspension forces have been particularised to the case of the short long arm independent suspension. Longitudinal loads are computed in the side view plane of the wheel whilst lateral and vertical loads are studied in the front view plane of the axle. The specific case of bump stops has also been discussed in the front view plane. Dynamic loading cases have been defined as static load factors. Finally, a two-dimensional kinematic model of the suspension has been created. This kinematic model is declined into two separate cases. The first one corresponds to the suspension with a rigid lower arm while the second corresponds to the motion of the suspension where the lower arm is replaced by a cantilever beam in large deformation. The kinematic model of the suspension with the lower arm replaced by the overhanging beam could not be modeled, as there was a lack of an analytical solution for the large deformation of these types of beams.

In the fourth chapter, preliminary designs of the transverse leaf springs have been computed and analysed. Initial assumptions have been made that the width of the leaves was fixed to 100mm and that the laminate was unidirectional in the direction of the load, hence the y-axis of the car. Starting with the leaf integrating the coil springs only (integration degree 1), its spring rate has been computed and yields K = 28.2N/mm. The associated geometry that leads to this spring rate gives a leaf thickness of 11mm and a total mass of 2.89kg. Preliminary modal analysis revealed that the leaf would not enter in resonance due to the irregularities of the road surface. Kinematics of the transverse leaf suspension revealed similar behavior with the original suspension except that the vertical force in the contact patch exhibits a more 'linear' behavior in jounce. For the leaf integrating the coil springs and anti-roll bar (integration degree 2a), spring rate and kinematic curves are the same as for the previous design. However, due to the pivot mounts, the thickness of the leaf increases to 17.3mm, leading to a mass of 4.87kg for the leaf. In this case, the leaf adds an equivalent roll stiffness of 936Nm/deg on the axle. Variation of the equivalent roll stiffness of the axle as a function of the length between

mounts has been studied and showed that increasing the distance between mounts adds more roll stiffness to the axle. For the leaf integrating the coil springs and lower arms (integration degree 2b), the spring rate has been computed and yields K = 26.68N/mm. The thickness and geometry of the leaf is very close to the one of the integration degree 1, as its total mass is 3.07kg. Analysis of the kinematic curves revealed a change in the camber gain variation along the stroke, as the transverse leaf induces more positive camber gain in the start of the rebound phase and a more growing negative camber gain later in the rebound phase. The vertical static load in the contact patch was however closer to the one of the original suspension. A more thorough dynamic loading analysis has been conducted, showing that lateral and longitudinal loads acting on the leaf could be neglected. Finally, the leaf with complete integration of the suspension members (integration degree 3) was assumed as having the same geometry as for the integration degree 2a. Different leaf designs are then compared based on their kinematic curves and mass savings. This allowed to highlight a maximum mass saving of 72% for the integration degree while the minimum mass saving is 12% for the integration degree 2a. After that, shape optimisation has been discussed, leaving a possible geometry where the leaf is large and thin towards the support on the car body and thick and narrow close to its free ends. This geometry allows a diminution of the maximum bending stress while having a more homogeneous stress distribution along the length of the leaf. The value of the equivalent roll stiffness was also discussed as its value was too big compared to standard values of the roll stiffness of axles in passenger cars ($\approx$ 400Nm/deg). Discussion led to the conclusion that it would be necessary to reduce the thickness of the part of the leaf that lies in-between the mounts.

In the last chapter, finite element models of the curved leafs and additional equivalent straight beams have been created. These models are made of 5mm Mindlin shell elements. Large displacements of the leafs springs are analysed thanks to the NASTRAN SOL402 multi-step non-linear kinematics solver used in non-linear statics. This revealed that for the integration degree 2b of the leaf, the analytical expression accounting for the large deformation of the leaf was only accurate for vertical deflection under 75mm and led to an error of 10mm for the minimum rebound position of the leaf. This led to the conclusion that a more precise model needs to be used in this case. For the large deformation of the leaf with integration degree 3, computation showed that the large deformation of the leaf was actually well modeled using the rotating lower rigid arm of the original suspension. Finally, modal analysis was performed using NASTRAN SOL103. Results highlighted the differences between the expected natural frequencies for the straight leaf in the case the leaf was modeled by a cantilever beam. Overall, natural frequencies of all leaves were higher than the 12Hz induces by the road surface irregularities.

Future perspectives

A non-exhaustive list of possible improvements and recommendations to account for future developments in the design methods for transverse composite leaf springs:

- Development of the Timoshenko beam theory to derive the analytical expression of the lateral deflection of the beam as a function of the vertical deflection in the case of the overhanging beam. This, to derive the design for the full integration of the leaf (coil springs + anti-roll bar + lower arms) which could not be done in this thesis.

- Integration of the transverse leaf spring into the multi-body finite element model. This will allow to determine the stresses in the leaf due to the imposed movement of the lower arm for integration degrees 1 and 2a.

- Modeling of the mounts and joints linking the transverse leaf spring to the suspension members and car body. These elements are key in the modeling of the transverse suspension leaf spring and can have great impact on the behavior of the suspension [13].

- Introduction of topology optimisation in the design phase. This requires to adapt the analytical method to variable cross sections of the leaf.

- Validation of the leaf designs using a more developed multi-body model. In this thesis, dynamic loads are computed using equivalent static loads. These loads could however be modeled to take into account their transient nature in the multi-body FE model.

- Modeling of bump stop as a spring and integration into both multi-body FE and analytical models.

- Final validation of the designs, by the means of a prototype suspension integrated into an existing chassis. Experiments can then be carried out to compare with expected results obtained from the analytical method and multi-body FE model.

Bibliography

[1] D. Richard. Automotive suspension systems benefit from composites. *Reinforced Plastics*, 47:18–21, 12 2003. doi: 10.1016/S0034-3617(03)00072-9.

[2] Ludwig Seethaler. Design of an innovative car wheel suspension concept with a fiber-reinforced plastic spring/control arm. In Peter E. Pfeffer, editor, *11th International Munich Chassis Symposium 2020*, pages 267–278, Berlin, Heidelberg, 2021. Springer Berlin Heidelberg. ISBN 978-3-662-63193-5.

[3] P. Beardmore and C.F. Johnson. The potential for composites in structural automotive applications. *Composites Science and Technology*, 26(4):251–281, 1986. ISSN 0266-3538. doi: https://doi.org/10.1016/0266-3538(86)90002-3. URL `https://www.sciencedirect.com/science/article/pii/0266353886900023`.

[4] David C Barton and John D Fieldhouse. *Automotive Chassis Engineering*. Springer International Publishing AG, Cham, 2018. ISBN 3319724363.

[5] E. Favary. Springs and spring suspensions. *SAE Transactions*, 15:143–176, 1920. ISSN 0096736X, 25771531. URL `http://www.jstor.org/stable/44717874`.

[6] Emmanuel Tromme and Pierre Duysinx. Lecture notes in vehicle architecture and components, 2021 - 2022.

[7] Mahmood M Shokrieh and Davood Rezaei. Analysis and optimization of a composite leaf spring. *Composite structures*, 60(3):317–325, 2003. ISSN 0263-8223.

[8] M. Carello, A. G. Airale, A. Ferraris, A. Messana, and L. Sisca. Static design and finite element analysis of innovative cfrp transverse leaf spring. *Applied composite materials*, 24(6):1493–1508, 2017. ISSN 0929-189X.

[9] Mercedes-Benz Luxembourg. Ressort d'essieu arrière en plastique renforcé de fibres de verre, Accessed 2023-05-10. URL `https://www.mercedes-benz.lu/vans/fr/sprinter/panel-van/equipment/list-reference/suspension/rear-axle-springs-glass-fibre`.

[10] L. Brooke, B. Ford, and P. Mooradian. *Ford Model T: The Car That Put the World on Wheels*. Motorbooks, 2008. ISBN 9781610584609. URL `https://books.google.be/books?id=4RYSEAAAQBAJ`.

[11] Giancarlo Genta. *The automotive chassis*. Mechanical engineering series. Springer, Dordrecht, 2009. ISBN 9781402086748.

[12] Rick Oleson. Ford Model T front suspension, Accessed 2023-05-10. URL https://www.flickr.com/photos/rick_oleson/19809816865.

[13] Michael Lamm. *The newest corvette: From A through Z-51*. Lamm-Morada Pub. Co., 1983,issn=ISBN 978-0932128041.

[14] Corvette Kingdom. Suspension Overhaul, Accessed 2023-05-10. URL https://www.corvettekingdom.co.uk/suspension-overhaul-packages.

[15] Dave McLellan. Corvette from the inside: the 50 year development history. *Scitech Book News*, 26(3), 2002. ISSN 0196-6006.

[16] Amanda Jacob. Volvo XC90 features polyurethane composite leaf spring, Accessed 2023-05-10. URL https://www.reinforcedplastics.com/content/news/volvo-xc90-features-polyurethane-composite-leaf-spring/.

[17] Dong Geun Lee. Transverse leaf spring for suspension of vehicle, KR Patent 20130005910A, Jan. 2013.

[18] Volvo Cars Global Media Newsroom. The all-new Volvo XC90 - rear suspension, Accessed 2023-05-10. URL https://www.media.volvocars.com/global/en-gb/media/photos/149308/the-all-new-volvo-xc90-rear-suspension.

[19] Dobbertin Performance Innovations. What makes corvette suspension so cool?, Accessed 2023-05-10. URL https://rick486.wixsite.com/dobbertinperformance/blank-c3ga.

[20] Peter E Pfeffer. *11th International Munich Chassis Symposium 2020: Chassis.tech Plus*. Proceedings. Springer, 2021. ISBN 9783662631928.

[21] Mubea. Innovative - drive e-mobility with mubea, Accessed 2023-05-10. URL https://www.mubea.com/en/innovations.

[22] Olivier Bruls. Integrated simulation and reduced-order modeling of controlled flexible multibody systems, 2005.

[23] Pierre Duysinx, Olivier Bruls, Jean-François Collard, Paul Fisette, Christophe Lauwerys, and Jan Swevers. Optimization of mechatronic systems: application to a modern car equipped with a semi-active suspension, 2005.

[24] cars.com. 2004 audi a6, Accessed 2023-06-10. URL https://www.cars.com/research/audi-a6-2004/.

[25] ISO 8855:2011(en). Road vehicles — Vehicle dynamics and road-holding ability — Vocabulary. Standard, International Organization for Standardization, Geneva, CH, December 2011.

[26] Michel Geradin and Daniel J. Rixen. *Mechanical vibrations: theory and application to structural dynamics*. Wiley, New York, 3rd ed edition, 2015. ISBN 9781118900208.

[27] Mohd Khairul Nizam Bin Suhaimin. Kinematic analysis performance between short long arm and parallel suspension for racing car. 2018. URL https://api.semanticscholar.org/CorpusID:195256919.

[28] Joo-teck Jeffrey Kueh and Tarlochan Faris. Finite element analysis on the static and fatigue characteristics of composite multi-leaf spring. *Journal of Zhejiang University. A. Science*, 13(3):159–164, 2012. ISSN 1673-565X.

[29] W.J. Yu and H.C. Kim. Double tapered frp beam for automotive suspension leaf spring. *Composite Structures*, 9(4):279–300, 1988. ISSN 0263-8223. doi: https://doi.org/10.1016/0263-8223(88)90049-9. URL https://www.sciencedirect.com/science/article/pii/0263822388900499.

[30] M.K. Hagnell and M. Åkermo. The economic and mechanical potential of closed loop material usage and recycling of fibre-reinforced composite materials. *Journal of Cleaner Production*, 223:957–968, 2019. ISSN 0959-6526. doi: https://doi.org/10.1016/j.jclepro.2019.03.156. URL https://www.sciencedirect.com/science/article/pii/S0959652619308479.

[31] Warren Clarence Young. *Roark's formulas for stress and strain*. McGraw-Hill, New York, NY, 6th ed edition, 1989. ISBN 0070725411.

[32] Ginger Gardiner. Hp-rtm on the rise, Accessed 2023-05-26. URL https://www.compositesworld.com/articles/hp-rtm-on-the-rise.

[33] Alessio Vita, Vincenzo Castorani, Michele Germani, and Marco Marconi. Comparative life cycle assessment of low-pressure rtm, compression rtm and high-pressure rtm manufacturing processes to produce cfrp car hoods. *Procedia CIRP*, 80:352–357, 01 2019. doi: 10.1016/j.procir.2019.01.109.

[34] Dominick V. Rosato, Donald V. Rosato, and Matthew V. Rosato. 15 - reinforced plastic. In Dominick V. Rosato, Donald V. Rosato, and Matthew V. Rosato, editors, *Plastic Product Material and Process Selection Handbook*, pages 455–496. Elsevier, Oxford, 2004. ISBN 978-1-85617-431-2. doi: https://doi.org/10.1016/B978-185617431-2/50018-9. URL https://www.sciencedirect.com/science/article/pii/B9781856174312500189.

[35] IDI Composites International. Sheet molding compounds (smc), Accessed 2023-05-26. URL https://www.idicomposites.com/smc-bmc-overview.php.

[36] Michaël Bruyneel. Lecture notes in mechanics of composites, 2022 - 2023.

[37] Kashinath Saha and Sushanta Ghuku. A theoretical and experimental study on geometric nonlinearity of initially curved cantilever beams. *Engineering Science and Technology, an International Journal*, 08 2015. doi: 10.1016/j.jestch.2015.07.006.

[38] Ji Wang, Jian-Kang Chen, and Shijun Liao. An explicit solution of the large deformation of a cantilever beam under point load at the free tip. *Journal of Computational and Applied Mathematics*, 212(2):320–330, 2008. ISSN 0377-0427. doi: https://doi.org/10.1016/j.cam.2006.12.009. URL https://www.sciencedirect.com/science/article/pii/S0377042706007333.

[39] S. Ali Faghidian and Isaac Elishakoff. The tale of shear coefficients in

timoshenko–ehrenfest beam theory: 130 years of progress. *Meccanica (Milan)*, 58 (1):97–108, 2023. ISSN 0025-6455.

[40] Olivier Bruls. Lecture notes in kinematics and dynamics of mechanisms, 2021 - 2022.

[41] Mathworks. Matlab - fsolve(). URL `https://nl.mathworks.com/help/optim/ug/fsolve.html`. Accessed: 2022-07-15.

[42] M. J.D. Powell. A fortran subroutine for solving systems of nonlinear algebraic equations. 11 1968. URL `https://www.osti.gov/biblio/4772677`.

[43] Auto Journal. Des ressorts de suspension plus lÉgers chez audi, Accessed 2023-08-13. URL `https://www.autojournal.fr/audi/a6`.

[44] Behzad Zai, Furqan Ahmad, Chang Lee, Tae-Ok Kim, and Myung kyun Park. Structural optimization of cantilever beam in conjunction with dynamic analysis. *Journal of the Korean Institute of Gas*, 15:31–36, 10 2011. doi: 10.7842/kigas.2011.15.5.031.

[45] 111 Racers. Grosse barre anti-roulis 1" réglable, Accessed 2023-08-16. URL `https://www.111racers.com/2013/12/02/grosse-barre-anti-roulis-1%E2%80%B3-reglable-elise-parts`.